UNIVERSITÀ DEGLI STUDI DI BARI "ALDO MORO"

Dipartimento Interateneo di Fisica "M. Merlin"

DOTTORATO DI RICERCA IN FISICA

CICLO XXXI

Settore Scientifico Disciplinare Fis/04

^{7}Be(n,p)^{7}Li cross section measurement for the Cosmological Lithium Problem at the n_TOF facility at CERN

Supervisori:
Dott. Nicola Colonna
Dott. Giuseppe Tagliente

Coordinatore:
Ch.mo Prof. Giuseppe Iaselli

Dottoranda:
Lucia Anna Damone

ESAME FINALE 2018

There is a theory which states that if ever anyone discovers exactly what the Universe is for and why it is here, it will instantly disappear and be replaced by something even more bizarre and inexplicable.
There is another theory which states that this has already happened.

Ad un padre che é il mio supereroe,
ad una madre forte come una roccia,
ad una sorella saggia come la storia
ed al mio amore Aronne.

Contents

Introduction

The Cosmological Lithium Problem (CLiP) is currently one of the most intriguing open questions in Cosmology. It refers to a discrepancy between the primordial ^{7}Li abundance inferred from astronomical observations and calculations based on the standard Big Bang Nucleosynthesis (BBN) theory [1, 2], that otherwise is very successful in predicting the production of the lightest nuclei during the first minutes of the Universe life. This issue has survived more than 50 years of efforts to find a solution. Over the time, various possibilities have been investigated, from the presence of systematic errors in the ^{7}Li abundance inferred from very old stars (the so-called Spite plateau stars), to possible hints of new physics beyond the Standard Model.

Among the various possibilities, a nuclear solution to the problem has also been considered. The 95% of primordial ^{7}Li is produced by electron capture decay of ^{7}Be, so the key to solve the CLiP could reside in the production and destruction rate of this isotope. Since the BBN relies on a network of nuclear reactions involving nucleons and light nuclei, it has been considered the possibility that an incomplete or an incorrect knowledge of the cross sections of some key reactions could be the reason for the large overestimation in the calculations of the primordial Lithium abundance. To clarify this issue, charged-particle induced reactions have been carefully studied, in search of resonances that could enhance the destruction of ^{7}Be, the progenitor of primordial Lithium, or alternatively reduce its predicted abundance. Up to now, all efforts in this respect have failed.

Neutron-induced reactions could also play a role in the ^{7}Be destruction in the early stage of the Universe. However, up to a few years ago, the cross sections of these reactions were still somewhat uncertain. This is the case, in particular, of the (n,α) reaction for which only one result existed in literature, dating back to the early 60s. The measurement had been performed at a nuclear reactor so that it provided only a point at thermal neutron energy, too far from the energy region of interest for BBN and therefore practically useless. In the case of the more important (n,p) reaction, two measurements had been performed in the 80s, but neither of them covered the neutron energy region of interest for Big Bang Nucleosynthesis and, most importantly, the results were largely inconsistent between each other.

Measurements of neutron-induced reactions on ^{7}Be are very challenging. The main problems are related to the difficulty in finding a sample material of adequate purity, in sufficient amount and, especially, to the very large specific activity of ^{7}Be that is a radioactive isotope of half-life of only 53 days, which makes background and radioprotection issues extremely hard to handle. This is the reason for the lack of data up to recently. These problems, however, become manageable if an intense neutron beam is available, since in this case a small amount of ^{7}Be can be used in the measurements. Such neutron beam became available few years ago at the n_TOF facility at CERN, with the construction of a new vertical beam line and a relative experimental area. Thanks to the extremely high neutron flux in that area, that I had the opportunity to deepen during my master thesis, the measurements of neutron-induced reactions on ^{7}Be finally became feasible. The first measurement performed at n_TOF was the (n,α) reaction. The results finally demonstrated that this reaction does not play a significant role in the Cosmological Lithium Problem.

This thesis regards the measurement of the second and most important neutron-induced reaction on ^{7}Be: the $^7Be(n,p)^7Li$ reaction. The measurement involved three different laboratories: the neutron facility n_TOF and the radioactive beam facility ISOLDE at CERN, as well as

the Analytical Chemistry Laboratory of the Paul Sherrer Institutes in Zurich, Switzerland. For the first time, a sample made by implantation of a radioactive beam was used in a neutron measurement and, for the first time, accurate cross sections for this reaction were determined in a wide energy range including the one of interest for BBN.

While the production and characterization of the sample, as well as the construction, mounting and test of the experimental set-up, involved a large number of people from the n_TOF and ISOLDE Collaborations, including myself, the data taking, data analysis and related Monte Carlo simulations were under my full and exclusive responsibility, as the calculations of the astrophysical reaction rates based on the new data, and the new estimate of the production of primordial ^{7}Li.

In brief, this is the story of a difficult but successful measurement, that has added new information on the puzzle of the Cosmological Lithium Problem. I hope anyone will enjoy reading about it as much as I did working on it.

Chapter 1

The Cosmological Lithium Problem

1.1. The first stages of the Universe up to the Nucleosynthesis

Since the Big Bang, 13.7 billion years ago, the Universe has passed through many different phases or epochs. The closest in time that current physics can get from the absolute beginning is the "Planck Epoch" (or Planck Era), from zero to approximately 10^{-43} seconds [3]. At this point, the Universe covered a region of only 10^{-35} meters and had a temperature of over $10^{32}{}^{\circ}C$. It is believed that in this epoch, the four fundamental forces (electromagnetism, weak nuclear force, strong nuclear force and gravity) all had the same strength and were possibly even unified into one fundamental force, held together by a perfect symmetry [4].
Between 10^{-43} to 10^{-36} second after the Big Bang, the force of gravity separated from the other fundamental forces and the earliest elementary particles (and antiparticles) begun to be created in a quark-gluon plasma. After this separation the Universe begun to expand exponentially, starting the so called cosmic inflation. The linear dimensions of the early Universe increased during this period, in a fraction of a second, to around 10 centimeters.

From 10^{-36} to 10^{-12} seconds, as the strong nuclear force separated from the other two, particle interactions created large numbers of exotic particles, including W and Z bosons and Higgs bosons.
After that phase, quarks, electrons and neutrinos formed in large numbers as the Universe cooled off to below 10^{15} degrees and the four fundamental forces assumed their present forms. Quarks and antiquarks annihilated each other, but, in a process known as baryogenesis, a surplus of quarks (about one for every billion pairs) survived, which ultimately combined to form matter.
From 10^{-6} seconds to 3 minutes after the Big Bang, the temperature of the Universe cooled enough, to about 10^{12} degrees, to allow quarks to combine to form hadrons. Electrons colliding with protons, fused to form neutrons and neutrinos, these last ones continuing to travel freely through space today at or near the speed of light [5]. Following, hadrons and antihadrons annihilated each other to form leptons (such as electrons) and antileptons (such as positrons). Electrons and positrons collided and annihilated each other, freeing energy in the form of photons.
Three minutes after the Big Bang, the production of light elements started, continuing up to 20 minutes, a process known as Big Bang Nucleosynthesis. At this point, the temperature of the Universe had fallen to the point (about 10^9 degrees) where atomic nuclei can begin to form, as protons and neutrons combine through nuclear fusion. In this way nuclei of the simple elements of ^{2}H, ^{3}He, ^{4}He and ^{7}Li were formed. After about 20 minutes, the temperature and density of the Universe fell to the point where nuclear fusion cannot continue.

1.2. The Big Bang Nucleosynthesis Theory

The theory of Big Bang Nucleosynthesis (BBN) gives a detailed mathematical description of the production of the light elements, ^{2}H, ^{3}He, ^{4}He and ^{7}Li, just three minutes after the Big Bang.
The BBN theory is based on the following assumptions:

- a gravity governed by general relativity;
- a homogeneus and isotropic Universe;
- the Standard Model of particle physics;
- dark matter and dark energy supplement the particle content of the Standard Model.

The theory of Big Bang Nucleosynthesis contains few parameters that allow to study the light element formation such as the neutron decay time τ_n and the number of neutrino families N_ν (see, for instance, Ref. [6]). The LEP experiments deduced the number of neutrino families [7] to the value N_ν=2.9840±0.0082, and neutron lifetime measurements have inferred that $\tau_n \approx 880.2 \pm 1.0$ s [8].
Another important parameter of BBN models is the neutron-proton ratio. Once stable hadrons can form from the quark-gluon plasma in the very early Universe, n and p are kept in thermal equilibrium by the weak interactions:

$$n + \nu_e \longleftrightarrow p + e^- \tag{1.1}$$

and

$$p + \overline{\nu_e} \longleftrightarrow n + e^+ \tag{1.2}$$

that lead the number of neutrons and protons to an equilibrium ratio:

$$\frac{n}{p} = e^{-(m_n - m_p)/T} \tag{1.3}$$

At $kT = kT_f \approx 1$ MeV (where T_f is the freeze out temperature), which is reached ≈ 2 minutes after the Big Bang, the $n - p$ interconversion (Equations 1.1 and 1.2) stops as the weak interaction "freezes out". As a consequence, the neutron-to-proton ratio is fixed at the value: $n/p \approx e^{-(m_n - m_p)/T_f} \sim 1/6$. At this stage deuterium production through the $p\,(n, \gamma)\,d$, takes place, partially counterbalanced by photodissociation. During this time, free neutron decay reduces the neutron to proton ratio

to $\approx 1/7$.
At $T \approx 0.07MeV$, blackbody photons become ineffective in photodissociating deuterium. As a consequence, the deuteron abundance rapidly rises, triggering a series of reactions in which all light elements are built via strong (i.e. nuclear) interactions.

The last parameter of the BBN theory, which affects the formation and the abundance of the light elements, is the relative amounts of baryons (nucleons) and radiation, which are parameterized by the baryon-to-photon ratio:

$$\eta \equiv \frac{\eta_b}{\eta_\gamma} = 2.74 \times 10^{-8} \Omega_b h^2 \tag{1.4}$$

Here Ω_b is the barion density of the Universe. This parameter controls the rate at which nucleons collide and react, and affects the model prediction of element abundances after nucleosynthesis ends.

The Wilkinson Microwave Anisotropy Probe (WMAP) [9], a spacecraft operating from 2001 to 2010, played an important role in the determination of the baryon to photon ratio. The WMAP objective was to measure the temperature differences in the Cosmic Microwave Background (CMB) radiation. The anisotropies then were used to measure the Universe geometry, content and evolution, allowing to test the Big Bang model and the cosmic inflation theory. For that, the mission created a full sky map of the CMB (Figure 1.1). Furthermore the WMAP mission helped to determine the age of the Universe to better than 1% precision. The content of the Universe presently consists of $4.628\% \pm 0.093\%$ ordinary baryonic matter, $24.02\%^{+0.88\%}_{-0.87\%}$ cold dark matter (CDM) that neither emits nor absorbs light, and $71.35\%^{+0.95\%}_{-0.96\%}$ of dark energy [10].

Among all these important results from the WMAP, one of the most precise and robust results is the measurement of the cosmic baryon density and thus of η. The anisotropies of the cosmic microwave radiation (CMB) allowed to determine the value of η [11, 12] when the Universe was about 0.3 Myr old. The most recent WMAP data release gives

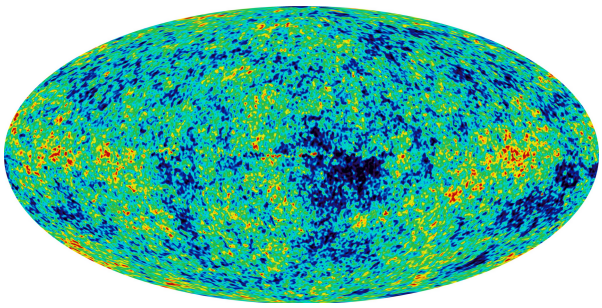

Figure 1.1: WMAP image of background cosmic radiation with a 13 arcminute resolution via multi frequency observation [9]. The map contains 3,145,728 pixels.

$$\eta = (6.19 \pm 0.15) \times 10^{-10} \tag{1.5}$$

This high precision value is now fixed in models of Big Bang Nucleosynthesis.

1.2.1 The reactions mostly responsable for the production of light nuclides

The simplified reaction network shown in Figure 1.2 highlights the reactions mostly responsable for the production of light nuclides. In contrast to stellar nucleosynthesis, for BBN the number of key reactions is small and well defined.

A few minutes ($\approx$ 3 min) after the Big Bang, deuterons were formed by neutron capture on protons by means of the reaction $p(n,\gamma)d$. The formation of deuterons is strongly dependent on the value of η. Once they are formed, deuterons are promptly destroyed leading to the formation of ^{3}He and ^{3}H that are then converted into ^{4}He; the reactions responsible of this production are fast and immediately convert the newly formed deuterium; in detail, these reactions are:

$$d + p \Rightarrow^3 He + \gamma \tag{1.6}$$

$$d + d \Rightarrow^3 He + n \tag{1.7}$$

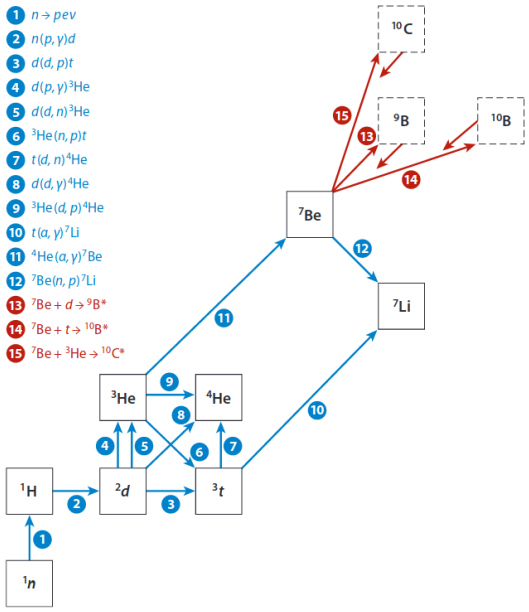

Figure 1.2: Simplified Big Bang Nucleosynthesis nuclear reaction network. Shown are 12 standard important reactions (blue) and 3 proposed new reactions (red) [13].

$$d + d \Rightarrow t + p \tag{1.8}$$

$$^3He + n \Rightarrow t + p \tag{1.9}$$

followed by:

$$^3He + d \Rightarrow^4 He + p \tag{1.10}$$

$$t + d \Rightarrow^4 He + n \tag{1.11}$$

Fusion reactions with neutrons at this stage are irrelevant because free neutrons are immediately captured once deuterium fusion begins. Since there are no stable elements with atomic weight A=5 and fusion involving deuterium does not play a role because its abundance is very low, nucleosynthesis can proceed only by the fusion of ^{4}He with tritium and ^{3}He to build up elements with A=7:

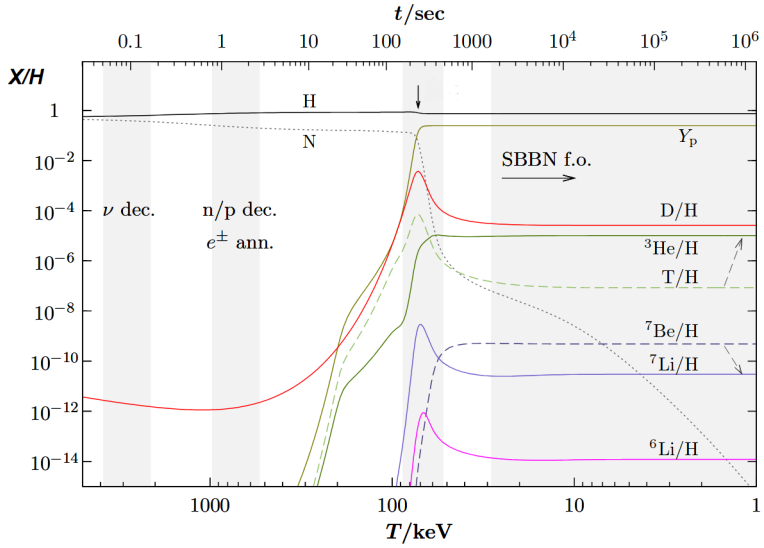

Figure 1.3: Time and temperature evolution of the abundance of light elements during and after the Big Bang Nucleosynthesis (BBN) [14]. The vertical arrow indicates the moment at which most of the helium nuclei are synthesized. The gray vertical bands indicate main BBN stages. From left to right: neutrino decoupling, electron-positron annihilation and n/p freeze-out, D bottleneck, and freeze-out of all nuclear reactions. Y_p denotes the ^{4}He mass fraction.

$$t + {}^4He \Rightarrow {}^7Li + \gamma \tag{1.12}$$

$${}^3He + {}^4He \Rightarrow {}^7Be + \gamma \tag{1.13}$$

$${}^7Be + e^- \Rightarrow {}^7Li + \nu_e \tag{1.14}$$

Figure 1.3 shows the nucleosynthesis of the primordial elements as a function of time (or temperature) [14]. ^{2}H and ^{3}H are intermediate states, through which the reactions proceed towards ^{4}He (see Eq. 1.10 and 1.11). Therefore their abundance first rises, it is highest at the time when ^{4}He production is fastest, and then falls as ^{4}He reaches its maximum. ^{3}He is also an intermediate state, but the main channel from ^{3}He to ^{4}He is via ${}^3He + n \Rightarrow {}^3H + p$ reaction, which terminates soon since free neutrons are captured in other reactions. Therefore the abundance of ^{3}He does not fall

the same way as ^{2}H and ^{3}H. The abundance of ^{7}Li also rises at first and then falls as lithium is destroyed via the $^7Li + p \Rightarrow^4 He +^4 He$ reaction. Since ^{4}He has a higher binding energy per nucleon than ^{7}Li and ^{7}Be, the reactions leading to ^{4}He production are energetically favoured. However, in the case of ^{7}Be, the reaction $^7Be + n \Rightarrow^4 He +^4 He$ is hindered by the lack of free neutrons whose number decreases with time.

1.3. Comparison between theoretical predictions and observations of the primordial abundances of ^{2}H, ^{3}He, ^{4}He and ^{7}Li

The BBN model predicts that the Universe is composed of about 75% of hydrogen and 25% of helium, about 0.01% of ^{2}H and ^{3}He, a small abundance of lithium (being the Li/H ratio on the order of 10^{-10}) and a negligible amount of heavier elements [15].

Figure 1.4 shows the standard BBN light element abundances (relative to hydrogen) as a function of the single free parameter η (Equation 1.4). The ^{4}He abundance depends only weakly on η. In contrast, deuterium drops strongly with η and ^{3}He decreases substantially.
The envelopes around the curves in Figure 1.4 correspond to the uncertainties in the abundance predictions, while the horizontal lines indicate the inferred primordial abundances from observations. The uncertainty for ^{4}He is very small ($< 1\%$), for deuterium and ^{3}He are small ($\sim 7\%$), whereas for ^{7}Li uncertainty is larger ($\sim$ 12% in the high-η region of interest). The vertical band represents the WMAP determination of η.

The main problem in comparing the light element abundances predicted by primordial nucleosynthesis models with values inferred from astronomical observations is that further fusion processes have happened since primordial fusion ceased. In order to determine an abundance as close as possible to the primordial value, observations have either to

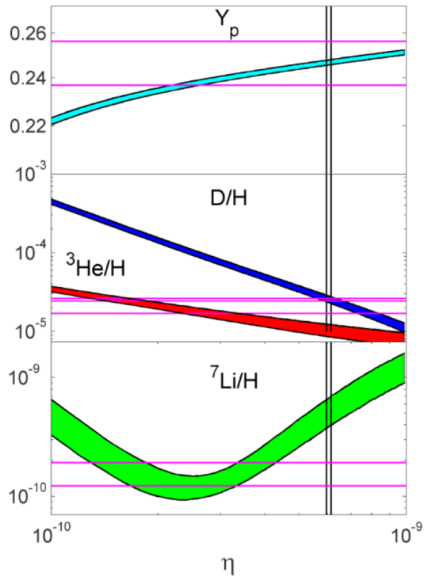

Figure 1.4: Prediction of Big Bang Nucleosynthesis models for light element abundances versus the baryon to photon ratio η [16]. The curve widths indicate the theoretical uncertainties while the horizontal lines indicat the inferred primordial abundances from observations. The vertical band represents the WMAP determination of η. Y_p denotes the ^{4}He mass fraction.

consider stellar objects in which little or no contamination by later nucleosynthesis is expected, or those in which observed element abundances can be corrected for changes during cosmic history.

Deuterium abundance can be measured directly at high redshift (i.e. old and distant objects). It is present in distant neutral hydrogen gas clouds, which are observed in absorption along sight lines to distant quasars. At present, there are seven systems with robust deuterium measurements [17, 18, 19, 20, 21]. These lie around redshift z$\sim$3 and have a metallicity that is two orders of magnitude less than that of solar system material. We recall here that the term metallicity for a stellar object describes the abundance of elements heavier than helium and is related to the age of a star. Therefore, in low metallicity systems, deuterium should be essentially primordial. The deuterium abundance inferred in

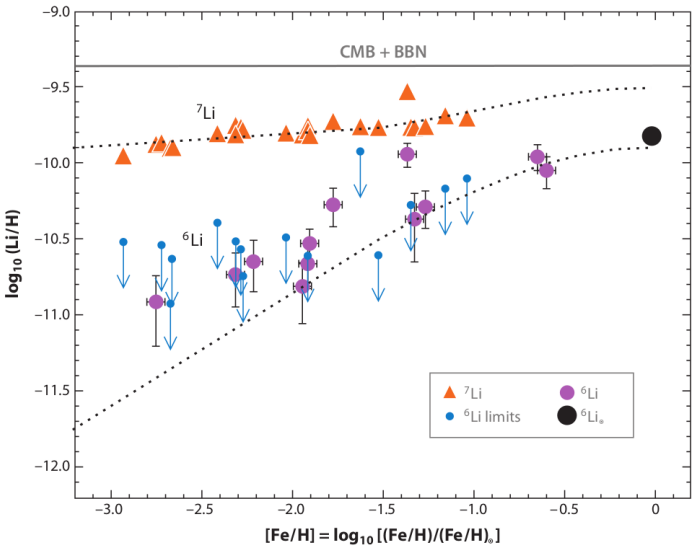

Figure 1.5: Lithium abundances in selected metal poor Galactic halo stars. For each star, both lithium isotopes are plotted versus the stars metallicity: $[Fe/H] = log_{10}[(Fe/H)_{obs}/(Fe/H_o)]$. Upper points show ^{7}Li. The flatness of ^{7}Li versus iron is known as the Spite plateau; it indicates that the bulk of the lithium is unrelated to Galactic nucleosynthesis processes and thus is primordial. The horizontal band represents the $CMB + WMAP$ prediction; the gap between this prediction and the plateau illustrates the ^{7}Li problem. Points below the Spite plateau show ^{6}Li abundances; the apparent flatness of these points constitutes the ^{6}Li problem. Curves show predictions of a Galactic cosmic ray nucleosynthesis model.

these observations is:

$$\frac{D}{H} = (2.82 \pm 0.21) \times 10^{-5} \tag{1.15}$$

in very close agreement with the predictions of BBN theory. ^{4}He can be measured in emission from nearby metal-poor galaxies [22, 23, 24, 25, 26]. ^{3}He is at present accessible only in the interstellar medium of our Galaxy [27]. This unfortunately means it cannot be measured at low metallicity, and so its primordial abundance cannot be determined reliably [28]; for this reason, ^{3}He is not used to constrain BBN theory.

Finally ^{7}Li is measured in the atmospheres of metal poor stars in the stellar halo (Population II) of our Galaxy. Due to convective motions, lithium from the surface can be transported towards the hot interior of

the star, where it can be burned via $^7Li(p,^4He)^4He$ reaction. This effect is evidenced by low lithium abundances in cool halo stars. Fortunately, the hottest (most massive) halo stars have thin convection zones and show no correlation between lithium and temperature. Therefore, the primordial lithium abundance is inferred only from these stars.
Figure 1.5 shows lithium and iron abundances for a sample of halo stars. The ratio of lithium to hydrogen (Li/H) content, is nearly independent of the ratio of iron to hydrogen (Fe/H) that indicates the metallicity of the stars and consequently the age; this flat trend is known as the Spite plateau in honor of its discoverer [29]. Since the abundance of heavy elements such as iron (metals) increases with time as Galactic nucleosynthesis proceeds and matter cycles in and out of stars, the Spite plateau indicates that in most halo stars lithium is uncorrelated with Galactic nulceosynthesis. This is considered an evidence that the ^{7}Li observed in Spite plateau stars is primordial.

1.3.1 The Cosmological Lithium Problem

By propagating the errors on the model calculations as well as those on the observed values, the likelihood distribution of the abundance of the light elements can be computed.

Figure 1.6 shows such distributions: the blue curves and areas represent the likelihoods predicted by the standard BBN theory using the cosmic baryon density determined by WMAP.

The yellow curves represent the observational likelihoods of the primordial abundances, while the dotted curves show the effect of different analyses of abundance data; the difference between these and the yellow curves gives an idea of the systematic errors. A spectacular agreement of the deuterium to hydrogen ratio can be noted. In contrast, a strong mismatch between predicted and measured ^{7}Li abundance is observed, with the predictions substantially higher than the observations. The mass fraction for ^{4}He, historically denoted by Y_p, is taken from Ref. [30]. The deuterium abundance is inferred from the measurements of the cosmic

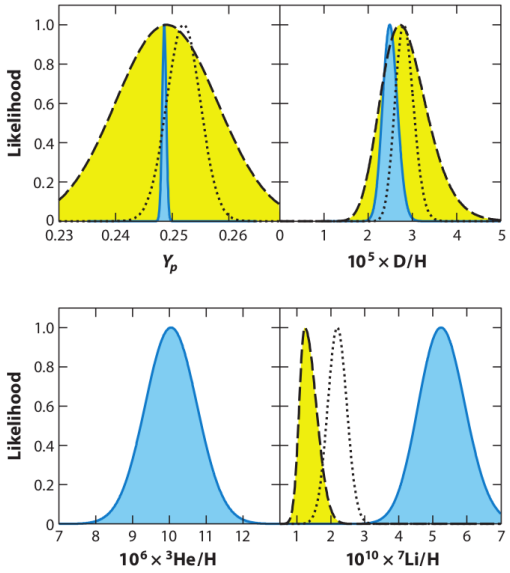

Figure 1.6: Comparison between the predicted and observed likelihood for the light elements [13]. Note the very good agreement of the ratio of deuterium to hydrogen and, in contrast, the strong mismatch between ^{7}Li theory and data, which constitutes the Cosmological Lithium Problem.

microwave background [12]. The ^{3}He abundance is taken from Ref. [31], and finally the lithium abundance is taken from Ref. [32].

The BBN model predictions for the ^{7}Li abundance shown in Figure 1.6 are in evident disagreement (roughly by a factor 3) with the observations. This large mismatch constitutes the so called Cosmological Lithium Problem (CLiP), a long standing issue that at present, after several decades of efforts, is still unsolved.

1.4. Solutions to The Cosmological Lithium Problem

Possible solutions to the Cosmological Lithium Problem can be categorized into three groups:

- Astrophysical solutions: a potential systematic error affects the measured primordial lithium abundance;

- Nuclear physics solutions: the reaction flow into and out mass-7 nuclei is miscalculated due to errors in the reaction cross sections;
- Solutions beyond the Standard Model: it invokes new particle physics or nonstandard cosmological physics.

These solutions are briefly described here below.

1.4.1 Astrophysical Solutions

First we consider the possibility that BBN predictions are correct, i.e. that standard cosmology and particle physics are valid, and the nuclear physics at the basis of the production of mass-7 nuclei (i.e. ^{7}Be and ^{7}Li) is properly calculated. If so, the measured value of the primordial lithium abundance must be affected by a large error, with the true value of the primordial Li abundance higher than currently inferred by a factor of three to four.
As mentioned in Section 1.3, the Spite plateau level is assumed to indicate the primordial abundance of ^{7}Li. A problem in this assumption could potentially explain the CLiP. For example, systematic errors could affect the Li/H ratio determined from the observations of the absorption lines in the photospheres of primitive stars. The only accessible lithium line has a wavelength of 670.8 nm and is the one relative to the neutral lithium, Li^0. The problem is that lithium is easily ionized (its ionization potential is 5.39 eV), so Li^0 line can be seen only in relatively cold stars with effective temperatures $T_{eff} < 8500$ K [33], while in hotter stars all lithium in the atmosphere is fully ionized, so that Li^0 line cannot be observed. In the stars of interest, lithium is mostly ionized and, since the measurements aim at determine the total lithium content of the stellar photosphere, summed over all ionization states, one must introduce a large ionization correction that is exponentially sensitive to the stellar temperature. Thus, a systematic shift in the temperature scale for halo stars would increase all stellar lithium abundances and raise the Spite plateau toward the

BBN+WMAP prediction. In practice, accurate determination of stellar temperatures remains nontrivial.

Another entirely separate question is whether the present lithium content in a star reflects or not its initial abundance. If the halo stars have destroyed some of their lithium, the present Li/H ratio represents a lower limit to the primordial lithium abundance. Indeed, given the low nuclear binding of ^{7}Li, even relatively low stellar temperatures (T$\geq 2.5\times10^6$K) could lead to a substantial destruction of the primordial lithium. The major effect is convection, which circulates photospheric material deep into the interior of the star (though still far from the stellar core), where nuclear burning can occur. Models for the evolution of low metallicity stars, appropriate for the Spite plateau, now include numerous mixing effects that can change the photospheric lithium: convective motions, turbulence, rotational circulation, diffusion and gravitational settling, and internal gravity waves [34, 35, 36, 37]. Among various studies, recently, several groups have found that at very low metallicity, [Fe/H]≤ -3, lithium abundances on average fall below the Spite Plateau (i.e., below the levels seen at metallicities $-3 \leq$[Fe/H]≤ -1.5) [32, 38, 39, 40]. This appears to confirm the presence of significant lithium depletion in at least some halo stars. An accurate determination of the primordial lithium abundance continues to be necessary and efforts in this sense are currently ongoing.

1.4.2 Nuclear Physics Solutions

Another possible explanation considers the possibility that the measured primordial lithium abundance is correct and that the Standard Model of particle physics and the standard cosmology are valid. In this case, the lithium problem could be related to errors in the BBN predictions, due to a wrong estimate of the reaction rates leading to the production and destruction of ^{7}Li. To examine a possible nuclear physics solution, one has to consider the processes by which ^{7}Li is produced. As described in Section 1.2 and shown in Figure 1.2, only a relatively small number of

reactions are important for producing the light elements. At BBN energies, there are two main pathways for ^{7}Li production: direct production in the $^3H\,(\alpha,\gamma)^7\,Li$ reaction, or through the electron capture decay of ^{7}Be.
While during the first minutes of the Universe life ^{7}Li is produced and destroyed by nuclear reactions, almost all primordial ^{7}Li is produced at later times by the electron capture decay of ^{7}Be. Therefore reducing the amount of ^{7}Be produced during BBN will reduce the abundance of the primordial ^{7}Li. The first reaction to consider is naturally the reaction forming ^{7}Be, namely $^3He\,(\alpha,\gamma)^7\,Be$. However this reaction is also crucial in the production of solar neutrinos. To fix the Cosmic Lithium Problem, the $^3He\,(\alpha,\gamma)^7\,Be$ normalization would need to be lower by a factor 3-4; if this were the case, the ^{7}Be and ^{8}Be solar neutrinos fluxes would be lower by a similar factor. The Sun can be seen as a reactor that investigates the $^3He\,(\alpha,\gamma)^7\,Be$ rate, and the precise agreement between solar neutrino predictions and observations confirms that this reaction is correctly estimated and therefore removes it as a possible solution to the Lithium Problem [41].

Destruction of ^{7}Be by charged particle induced reactions

If the ^{7}Li problem cannot be attributed to an overproduction of ^{7}Be, another explanation could be related to an underestimation of its destruction through various reactions.
One of the most important group of reactions are those involving charged nuclei. To produce sizable effects on the ^{7}Li abundance, their efficiency has to be increased by a very large factor. This seems possible only if new unknown resonances are found. This possibility has been investigated in the past, by using a method that allows to calculate the change in the ^{7}Li abundance produced by an arbitrary modification of the rate of various nuclear reactions. In particular, this method has been used to assess whether it is possible to increase the total ^{7}Be destruction rate to the level required to solve (or alleviate) the cosmic ^{7}Li puzzle.
It was found that the only destruction channels (induced by charged

particles) that could have a non negligible impact on the ^{7}Li abundance are the $^7Be + d$ and $^7Be + \alpha$ reactions.

a) $^7Be + d$

Postulating a resonance in the $^7Be + d$ reaction at an energy $E_r \sim$ 150 keV, with a total width $\Gamma_{tot}(E_r,R) \sim$ 45 keV, and partial widths $\Gamma_{out} \sim$ 35 keV and $\Gamma_{in}(E_r,R) \sim$ 10 keV, leads to a $\sim 40\%$ reduction in the ^{7}Li abundance. A non negligible suppression would, therefore, require the existence of a new excited state of ^{9}B around $E_r \sim$ 150 keV [42].

In 2005 at the CYCLONE radioactive-beam facility at Louvain-la-Neuve this reaction has been studied for the first time at energies appropriate to the Big Bang environment. The cross section was found to be a factor of 10 smaller than the one derived from earlier measurements. It is concluded therefore that this reaction cannot explain the discrepancy between observed and predicted primordial ^{7}Li abundances [43].

In [44], the possibility to have a resonance in the $^7Be + d$ reaction at an energy $E_r \sim 150$ keV was also studied by using the $^2H(^7Be, d)^7Be$ reaction. The data show no evidence for new resonances and allow to set an upper limit on the total resonance width at the level of $\sim$ 1 keV.

b) $^7Be + \alpha$

With this channel one obtains at most a $\sim 25\%$ reduction of the ^{7}Li abundance assuming a resonance in the $^7Be + \alpha$ channel with energy $E_r \sim$ 270 keV, with a total width $\Gamma_{tot}(E_r,R) \sim$ 160 eV and partial widths $\Gamma_{out} \sim$ 100 eV and $\Gamma_{in}(E_r,R) \sim$ 60 eV [42].

The possibility of a missing resonance in the $^7Be + \alpha$ channel has been considered studying the states of the compound nucleus ^{11}C. However, the levels have, at most, a few eV widths which are considerably lower than required to reduce the ^{7}Li abundance [45].

c) $^7Be + t$

With this channel, the maximum effect one can obtain is a $\sim$ 0.2% reduction of primordial ^{7}Li abundance [42]. To solve the Cosmological Lithium Problem the reaction rate of the ^7Be+t must be at least similar to that of ^7Be+n channel; but this is impossible for two reasons: first of all ^7Be+t collisions are suppressed by Coulomb repulsion and second, neutrons are more abundant than tritons at the temperature of interest for the synthesis of beryllium $T_{Be} \sim 50$ keV.

d) $^7Be +^3 He$
For this channel as well, a resonance cannot solve the problem because a strong Coulomb repulsion suppresses the reaction cross section at BBN temperatures [42]).

In view of the above results, the possibility of a nuclear physics solution of the cosmic ^{7}Li problem, based on reactions on ^{7}Be induced by charged particles can be excluded.

Neutron-induced reactions

In addition to the reactions involving charged nuclei, the reactions with neutrons also contribute to the destruction of ^{7}Be. The $^7Be(n,p)^7Li$ reaction is believed to be the most important one, accounting for 97% of ^{7}Be destruction through neutron reactions. The study of this reaction will be the main topic of this thesis. The next significant neutron reaction is believed to be the $^7Be(n,\alpha)^4He$ reaction, providing 2.5% of the destruction rate.
Despite the important role that these two reactions can play in the solution of the Cosmological Lithium Problem, data have been so far scarce or completely missing. The lack of experimental data is due to the intrinsic difficulty of the measurement, mostly related to the short half life of ^{7}Be, 53 days, and the consequently high specific activity of 13 GBq/μg.
Regarding the $^7Be(n,\alpha)^4He$, before n_TOF, only one measurement was performed in 1963 at the ISPRA reactor by Bassi [46], providing just

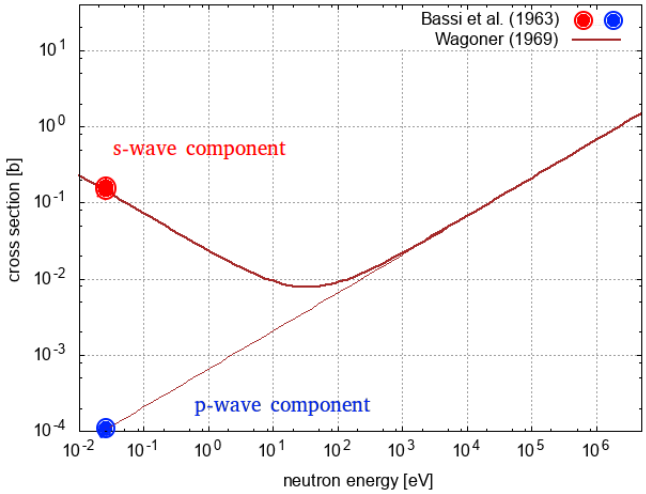

Figure 1.7: The red and blue point represent respectively the thermal point of the s-wave and p-wave component of the $^7Be(n,\alpha)^4He$ cross section measured by Bassi in 1963. The brown curve is the rate evaluation of the (n,α) reaction performed by Wagoner in 1969.

one point at thermal energy for the s-wave component of the partial $^7Be(n,\gamma\alpha)^4He$ cross-section and an upper limit for the p-wave component. In 1969 Wagoner, using just these two points and considering the typical $1/v$ trend for the s-wave channel and the $\sqrt{E}$ trend for the p-wave channel, evaluated a reaction rate for the (n,α) cross section [47]. The brown curve in Figure 1.7 shows the evaluated cross section used in BBN calculations up to very recently.

The construction of a second experimental area (EAR2) at n_TOF (Neutron Time of Flight) characterized by an extremely high instantaneous neutron flux (10^8 n/cm^2/pulse), a good energy resolution and a low repetition rate [48], offered the unique opportunity to perform time-of-flight measurements of $^7Be(n,p)^7Li$ and $^7Be(n,\alpha)^4He$ cross sections over a wide energy range (from thermal up to 1 MeV), covering the one of interest for the Big Bang Nucleosynthesis.

In 2016 at n_TOF the first time-of-flight measurement of the partial $^7Be(n,\gamma\alpha)^4He$ reaction was performed between 10 meV and 10 keV [49]. The results are reported in Figure 1.8. The purple squares represent the n_TOF results, that were found to be in agreement with the only point

measured by Bassi at thermal neutron energy. The thicker black curve represent the total cross section obtained by considering the branching ratios between different transitions. In order to derive a rate on the $^7Be(n,\alpha)^4He$ reaction in the energetic range of interest for Big-Bang Nucleosynthesis, the hatched area in Figure 1.8, the cross section has been complemented by the ENDF evaluation that is based on indirect measurements. The final result is represented by the green curve.
The n_TOF measurement allows to draw some conclusions on the role of the $^7Be(n,\alpha)^4He$ reaction in the Cosmological Lithium Problem. The first consideration regards the behaviour of the cross section as a function of neutron energy, with the experimental data clearly incompatible with the evaluation performed by Wagoner, previously discussed (brown curve in Figure 1.8). The most important result of the measurement is that even though below 100 eV neutron energy the cross section is over a factor of 20 higher than the one used in BBN calculations so far, in the energy range of interest for the Big Bang Nucleosynthesis the rate extracted from n_TOF data is a factor of 10 lower than the one estimated by Wagoner. This result ruled out a solution of the Cosmological Lithium Problem based on the $^7Be(n,\alpha)^4He$ reaction.

For the other most important neutron-induced reaction on ^{7}Be, the $^7Be(n,p)^7Li$ reaction, only few data existed dating back to the late 1980s. They are reported in Figure 1.9. None of them covers the full energy range of interest for the problem (20-200 keV) and they are in disagreement with each other [50, 51].

Moreover, above approximately 10 keV, the cross-section must match the one extracted from measurements of the time-reversal reaction $^7Li(p,n)^7Be$, such as the one performed by Sekharan et al. in 1976 [52], which provides accurate information in the upper part of the energy spectrum. This check can not be performed with the old data, since they stopped at neutron energies well below those of the time-reversal reaction. It is therefore evident that new data on the $^7Be(n,p)^7Li$ are needed to understand if this reaction could play an important role in solving the Cosmological Lithium Problem. A new measurement of $^7Be(n,p)^7Li$ cross section was

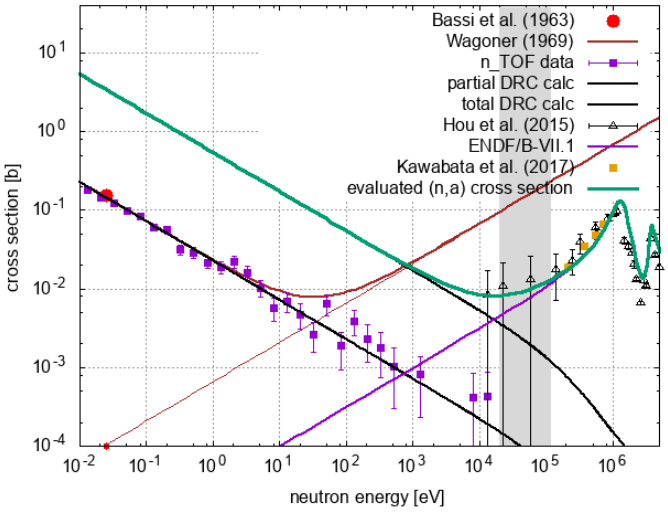

Figure 1.8: The partial $^{7}Be(n,\alpha)^{4}He$ cross section measured at n_TOF between 10 meV and 10 keV (purple squares) compared with the result of Bassi at thermal energy (red circle). The lower black curve represents the DRC calculations of the partial cross section for the excited states in ^{8}Be between 16.6 and 18.2 MeV accessible in the present experiment, while the upper one shows the total cross section obtained by considering the branching ratios between different transitions. The cross section suggested in Ref. [47] and used in BBN calculations is shown by the brown curve. A combination of the present results with ENDF/B-VII.1 evaluation based on indirect measurements, yields the total cross section up to a few MeV (green curve). The hatched area shows the neutron energy region of interest for big bang nucleosynthesis.

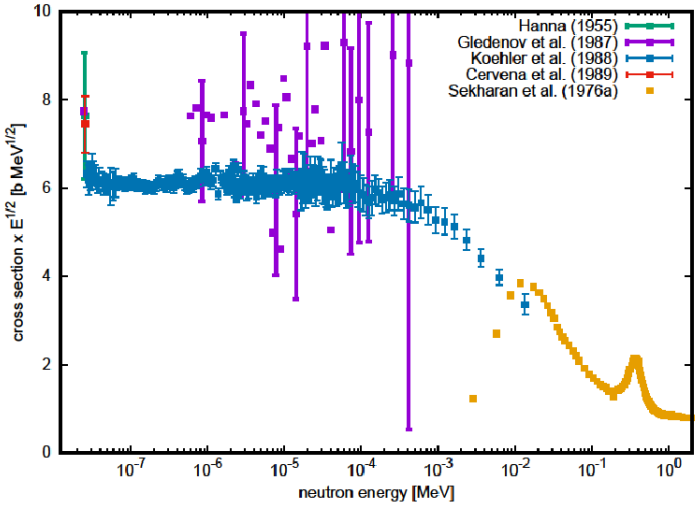

Figure 1.9: The measurements of the $^{7}Be(n,p)^{7}Li$ cross section dating back to the late 1980s. None of them covers the neutron energy region of interest for Big Bang Nucleosynthesis and they are largely inconsistent between each other.

therefore performed at n_TOF and is indeed the topic of this thesis.

1.4.3 Solutions beyond the Standard Model

Finally, we discuss the most radical class of solutions to the Lithium Problem. Specifically, we assume that primordial lithium has been reliably measured and that the nuclear physics of BBN is treated correctly. In this case the only possibility left is to question the basic assumption at the basis of BBN calculations: the Standard Model (SM) of particle physics and the standard cosmology. Various explanations of new physics beyond the SM have been proposed.

In [53], Andreas Goudelis et al., considered the possibility that the presence of light unknown electrically neutral particles X, interacting with nucleons during the Big Bang Nucleosynthesis, can reduce the cosmological abundance of ^{7}Li without affecting the precisely measured abundances of deuterium and helium. This particles must have precise characteristics: the masses and the lifetimes have to be bounded by 1.6 MeV $\leq m_X(E_X) \leq$ 20 MeV and 100 s $\leq \tau_X \leq 10^4$ s. Including the reactions of this unknown X particles into the BBN framework, a substantial reduction of the ^{7}Li abundance has been calculated.

To solve the problem, studies on the dark radiation ρ_{dr} have also been performed. Figure 1.10 [14] illustrates the changes to the abundances of helium, deuterium and lithium as a function of ρ_{dr}/ρ_{SM} (ρ_{SM} is the BBN energy density) and shows that one cannot achieve any significant degree of ^{7}Li suppression without violating other conditions.

Another hypotesis of Physics beyond the Standard Model regards changes in fundamental constants during BBN such as the fine-structure constant α_{EM}, the electron mass m_e, the neutron lifetime τ_n, the neutron proton mass difference m_n - m_p and the deuteron binding energy B_D [54, 55, 56]. The most sensitive of these parameters is the deuteron binding energy. A change of $-0.075 \leq \delta B_D/B_D \leq -0.04$ lowers the ^{7}Li abundance without perturbing ^{4}He or D/H beyond their observed error range. Thus, unified models that predict changes of this order could solve

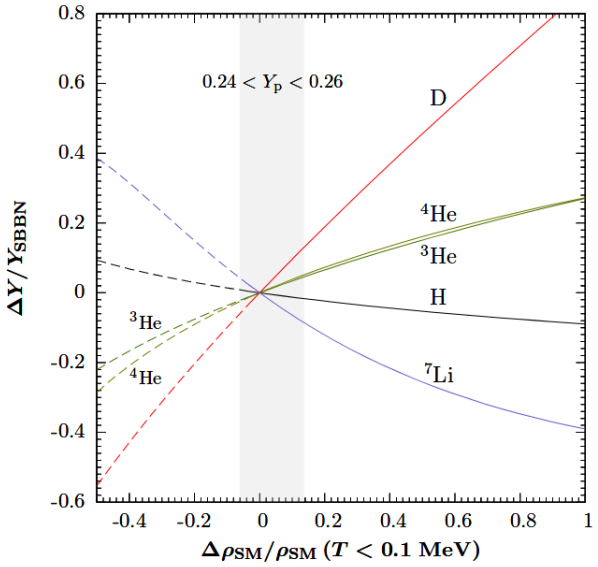

Figure 1.10: Change of nuclear abundances relative to their BBN values as a function of the dark radiation component $\rho_{dr}/\rho_{SM} = \Delta\rho_{dr}/\rho_{SM}$. The vertical band shows the allowed amount of dark radiation that keeps Y_p (The mass fraction for ^{4}He) in the 0.24-0.26 window.

the Lithium Problem.

One of the most exotic hypothesis relies on dark matter. The existence of dark matter is now well established and its cosmic abundance has been inferred precisely [57, 58, 59]. Dark matter must of course be present during BBN and it is assumed to be both nonrelativistic and weakly interacting. Then, if dark matter takes the form of a particle, it must be nonbaryonic and weakly interacting massive particle (WIMPs). On top of this, if the Universe begins with equal abundances of WIMPs and anti-WIMPs, their abundance is determined by the freeze-out of their annihilations.

In order to reproduce $\Omega_m \simeq 0.3$ today, the annihilations must occur at $\sim$ TeV scales (well before BBN). This is also the scale of the weak interaction and of current accelerator experiments. This fortunate coincidence is termed the WIMP miracle. WIMPs today are probably the stable end points of a decay cascade. If the decays occur during or after BBN, the interactions can change light element abundances [60] and therefore could

solve the Lithium Problem [61]. To estimate the effect of decaying massive particles during or after BBN, let's consider a particle x (and $\bar{x}$ if they are distinct) with mass $m_x \gg m_p$, which decays with lifetime τ_x. The decays can have electromagnetic and/or hadronic channels and, given the massive nature of x, the decay products will be very relativistic or, in other words, nonthermal. As these electromagnetic and/or hadronic cascades thermalize in the cosmic enviroment, they interact with the light elements, largely via fragmentation (photodissociation or spallation).
Of particular importance is the conversion of ^{7}Be into ^{7}Li with secondary neutrons

$$n + {}^7Be \Rightarrow p + {}^7Li \tag{1.16}$$

which substantially enhances mass-7 destruction because of the lower Coulomb barrier for ^{7}Li (with the consequent higher rates of charged particle induced reactions). Clearly this process is of great interest for the ^{7}Li problem. Considering the effect of nonthermal particles on light elements abundances, in the regime in which ^{7}Li is reduced, all other constraints are satisfied except D/H, which is unacceptably high due to secondary deuteron production. It is clear that this solution requires a fine tuning.

In conclusions, several possible explanations of the Cosmological Lithium problem have been proposed, but at present none of them is satisfactory. For the nuclear physics solution, one of the few possibilities still to be investigated regards the $^7Be(n,p)^7Li$ reaction, for which few data are presently available. The aim of this thesis is to provide new, accurate and complete data on this important reaction, measured at the neutron time-of-flight facility n_TOF at CERN.

Chapter 2

The n_TOF facility at CERN

The "neutron Time Of Flight" facility n_TOF was proposed at CERN in 1998 in order to satisfy the need of new and accurate nuclear data for Nuclear Astrophysics and various applications in Nuclear Technology. The construction was completed about two years later and n_TOF became fully operational in 2001. In 2008, a new and more robust spallation target was installed with a separate moderation and cooling circuits.
In 2013 the construction of a second beam line with the relative experimental area began (see Figure 2.1) and, one year later, in June 2014 it was completed [62, 63].

The main features of the n_TOF facility, which make it unique, are the high instantaneous flux, the high energy resolution and the wide energy spectrum of the neutron beam. These features, combined with the high-performing detection and acquisition systems, have allowed the n_TOF Collaboration to collect accurate and reliable nuclear data, addressing many open issues in various research fields and satisfying many requests of the scientific community.
At n_TOF the neutron beam is produced via spallation reactions induced by high energy protons (20 GeV) impinging on a lead target. Subsequently, neutrons travel through vacuum tubes toward the experimental areas that host the experimental set-up. The n_TOF facility is based on a spallation neutron source and consists of:

Figure 2.1: Construction of the second experimental area, EAR2 at n_TOF.

- a beam line for protons,
- a spallation target,
- two neutron beam lines,
- two experimental areas: Experimental Area 1 (EAR1) on the horizontal direction and Experimental Area 2 (EAR2) on the vertical of the spallation target [64].

Figure 2.2 shows schematically the location of the two experimental areas relative to the spallation target.

This chapter provides a brief description of the facility together with the main features of the neutron beam in terms of flux, energy resolution and spatial profile. The experimental campaign devoted to the characterization of the neutron beam in the second experimental area is also discussed in this chapter. It is worth to emphasize that the knowledge of the neutron beam characteristics is an important prerequisite to obtain the required accuracy in the cross sections of the neutron-induced reac-

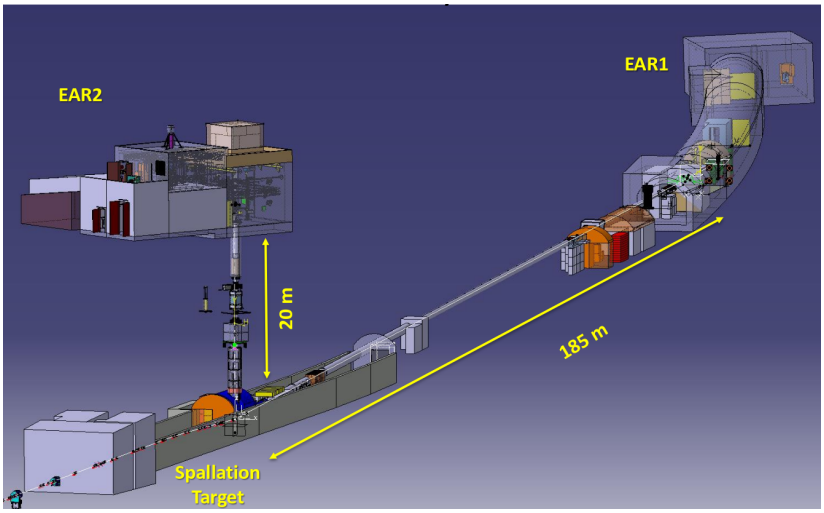

Figure 2.2: Schematic view showing the position of the two experimental areas EAR1 and EAR2, with respect to the spallation target.

tions being investigated. This is also the case of the $^7Be(n,p)^7Li$ reaction discussed in this thesis.

2.1. Time of Flight Tecnique

Measurements at the n_TOF facility are based on the time of flight technique [65], used to determine the neutron energy. The time a neutron takes to travel from the spallation target to the experimental area is given by the difference between the instant t_n in which its reaction products are revealed in the detector and the instant t_0 in which the neutron is generated in the spallation target.

$$TOF = t_n - t_0 \tag{2.1}$$

While t_n is accurately measured, t_0 can not be measured experimentally. However this quantity can be determined from the signal produced in the detectors by the so called γ-flash. Indeed when the protons hit the spallation target, γ-rays and ultrarelativistic particles are produced in a very short time. They reach the experimental area generating a signal in

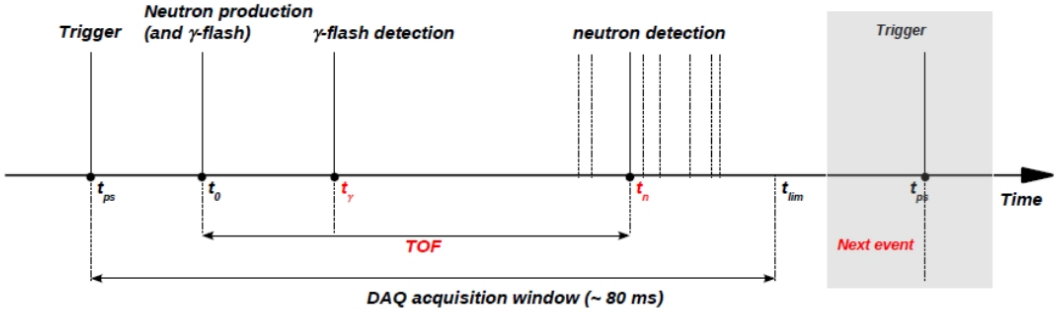

Figure 2.3: Temporal distribution of the signals involved in the determination of the neutron time of flight at n_TOF.

all detectors (the γ-flash) in a time equal to L/c, where L is the flight path. In other words, their measured time-of-flight is $t_\gamma = t_0 + L/c$. From this equation it is possible, by measuring t_γ experimentally, to extract and replace t_0 in the expression of the neutron time of flight above, obtaining:

$$TOF = t_n - t_\gamma + L/c \tag{2.2}$$

The time sequence just discussed is shown in Figure 2.3. When the trigger signal, sent by the proton accelerator, opens the Data Acquisition (DAQ) window, the γ-flash is the first to be registered at the time t_γ, while the reaction products of the neutron are recorded at subsequent times t_n.

Once the time of flight is known, the kinetic energy of a neutron in the relativistic case is determined by means of the following equations:

$$E_n = m_n c^2 \left(\frac{1}{\sqrt{1-\beta^2}} - 1 \right) \ , \quad \beta = \frac{v}{c} = \frac{L}{c \cdot TOF} \tag{2.3}$$

For the not relativistic case the above expression reduces to the simple relationship [66]:

$$E_n = \frac{1}{2} m_n \left(\frac{L}{TOF} \right)^2 \approx \left(72.29826 \cdot \frac{L\,(m)}{TOF\,(\mu s)} \right)^2 \tag{2.4}$$

2.2. The proton beam

The n_TOF facility is based on the proton beam accelerated by the CERN Proton Synchrotron (PS). A proton bunch is first accelerated in the Booster ring and then injected into the PS at 1.4 GeV/c. The PS can accelerate more bunches simultaneously, which are subsequently extracted and sent to different experiments. The bunches dedicated to the n_TOF facility are accelerated by PS up to a momentum of 20 GeV/c with a time width of 7 ns (r.m.s.). The proton beam characteristics, in particular the distance between two consecutive bunches, i.e. the repetition rate, the intensity and time width of the bunch, fit perfectly the need of a pulsed neutron source for time of flight measurements. Indeed the narrow proton bunch guarantees a high resolution on time of flight measurements and consequently on the reconstructed neutron kinetic energy [67]. The PS operates with a duty cycle of 0.8 Hz that corresponds to proton bunches separated by at least 1.2 s. Considering that the slowest neutrons (25 meV) take $\sim$ 100 ms to reach the experimental area at 200 m distance, a 1.2 s time separation avoids the overlap of consecutive bunches, a phenomenon known as "wrap-around". Where the overlap exsists (i.e. in other facilities) slow neutrons in a bunch are identified as fast neutrons in the following one, causing a significant background. At n_TOF such background component is completely eliminated.

2.3. The Spallation Target

The term *spallation* includes all processes that take place when energetic particles hit a heavy target leading to the emission of a large number of reaction products (light charged particles, neutrons, γ-rays, etc ...). During the first phase of the reaction, the interaction of the incident protons with nuclei causes the emission of few nucleons of intermediate energy, as well as the production of other particles. In a massive spallation target, these energetic secondary particles can hit other nuclei and interact with their nucleons. At the end of this phase of intranuclear cascade,

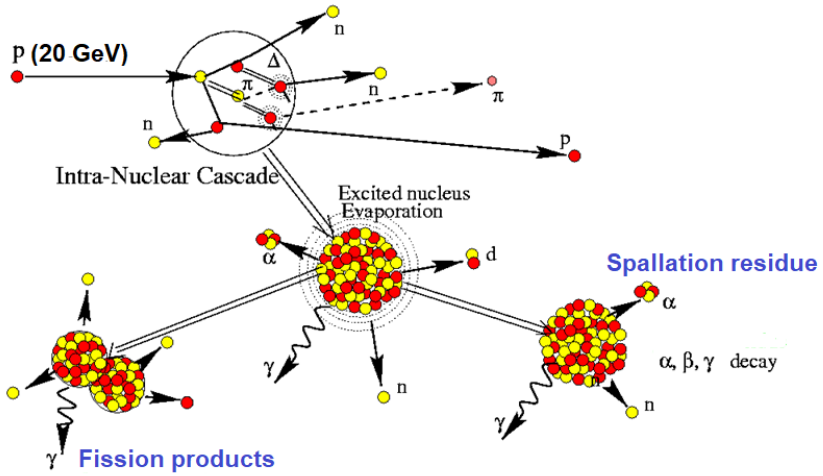

Figure 2.4: Schematic representation of spallation reactions.

residual nuclei are produced with an excitation energy of tens of MeV. The reaction then proceeds through a transitory phase in which the excited nuclei move towards equilibrium; during this phase, the emission of relatively fast nucleons is still possible. This process is known as pre-compound or pre-equilibrium emission. Finally, in the evaporation phase, the exited nuclei de-excite by evaporation with the emission of γ-rays and light particles among which neutrons of MeV energy. Figure 2.4 summarizes all phases involved in the spallation reaction.
The n_TOF spallation target consists of a cylindrical block of 99.99% [68] pure lead, of 60 cm diameter and 40 cm length cooled with demineralized water (Figure 2.5). The lead core is inserted in a pressurized aluminum container and installed in a cavity in a pre-existing tunnel (Figure 2.6).

In the first spallation target, the cooling water was used also as a moderator of the neutron energy. In the second target, the cooling circuit has been partially separated from the moderator to have more flexibility in changing the energy spectrum of the neutron beam. For this reason, the container is divided in two different volumes: the first one, filled with demineralized water and in direct contact with the lead block, is used for cooling, while the second volume, detached from the target and present

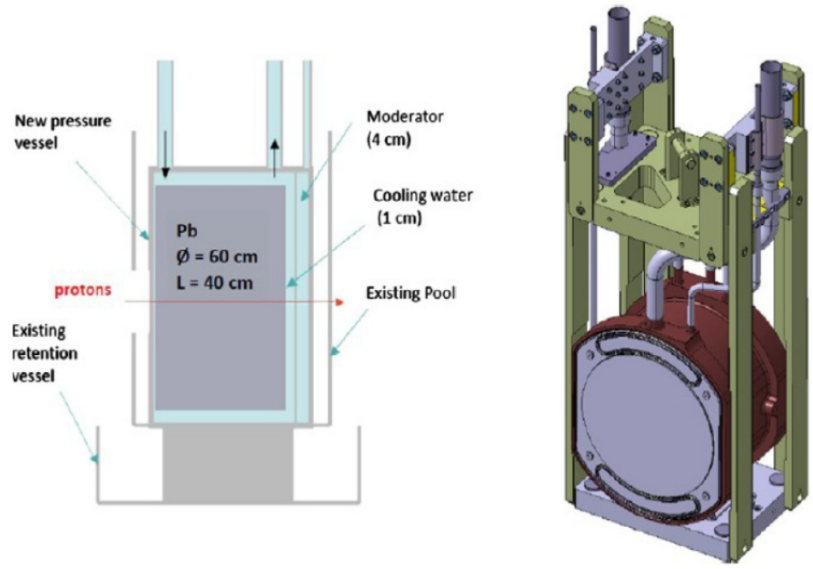

Figure 2.5: Schematic view of the n_TOF spallation target. On the left the various elements of the target are shown: the Pb block, the moderation and cooling circuit, the containment vessel, etc. On the right, the drawing of the fully assembled target is shown.

Figure 2.6: The installation of the new spallation in its cavity.

only in the neutron output side, can be filled with different liquids and acts as a moderator for the emitted neutrons. The current thickness of the water layer used for cooling is 1 cm, while the thickness of the moderator is 4 cm (Figure 2.5). The possibility to use a different liquid, such as borated water as moderator is very convenient. One of the main advantages is that it allows to reduce the background in the experimental area due to the 2.2 MeV gamma rays produced in the capture reaction on hydrogen. Using suitable moderators can substantially reduce, by about a factor 10 [69], this type of background.

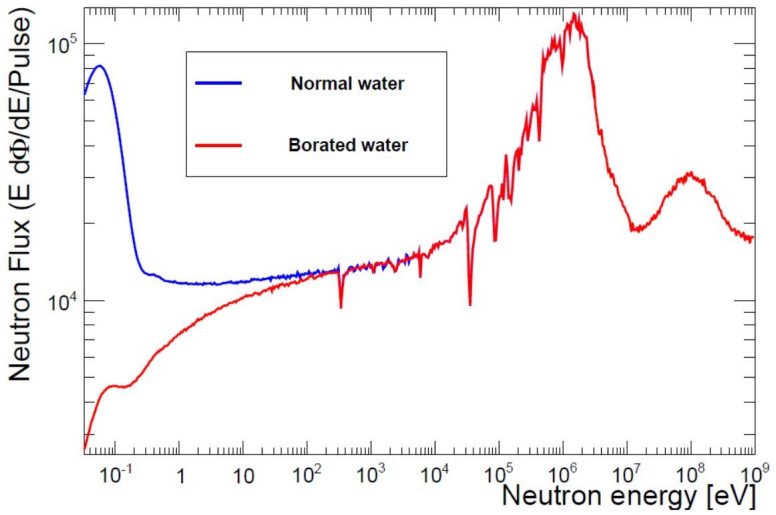

Figure 2.7: Comparison between the neutron flux in EAR1 produced with a moderator of normal water (blue curve) or borated water (red curve).

The use of different moderators also changes the shape of the neutron energy distribution. Figure 2.7 shows the comparison between the flux obtained with 5 cm of demineralized water in EAR1 and the one obtained with the introduction of borated water in the moderation circuit.

2.4. The first beam line and the first experimental area, EAR1

After being produced (and moderated) neutrons leave the spallation target and enter the beam lines. The one leading to the first experimental area is about 200 meters long in the horizontal direction. The neutrons produced in the spallation target propagate through vacuum tubes of different diameters, mounted inside a pre-existent tunnel. Along the flight path, as shown in Figure 2.8, there are several elements (concrete and iron walls, magnets, collimators, etc ...) in order to shape the spatial profile of the neutron beam, to reduce the background of charged particles and photons present in the beam and to minimize the background caused by neutrons scattered in the various elements of the beam line.

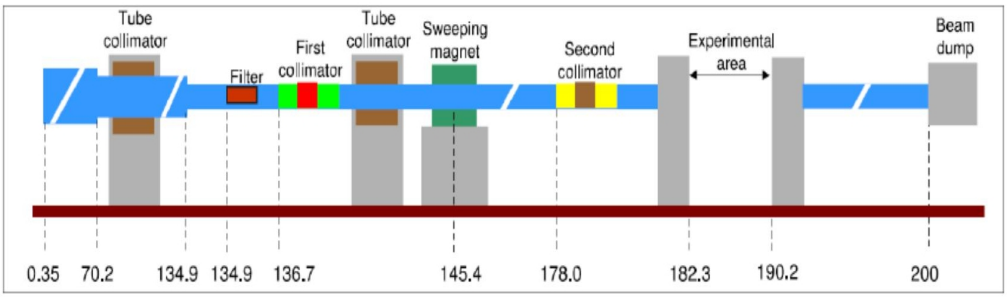

Figure 2.8: Schematic view of the n_TOF tunnel and the first experimental area, from the spallation target up to the beam dump (200 m).

As shown in Figure 2.8, the first experimental area (EAR1) is defined by two concrete walls, the first at about 182 m from the spallation target and the second 7 m downstream. These walls also act as shields against the radiation produced by the last collimator (on one side) and the beam dump (on the other side). The experimental area hosts the sample to be measured, the detectors and all the auxiliary equipment necessary for the measurements (Figure 2.9). It is classified as "Work Sector Type A", i.e. suitable to host unsealed radioactive sources, such as radioactive samples used in many measurements. To this purpose, it is equipped with

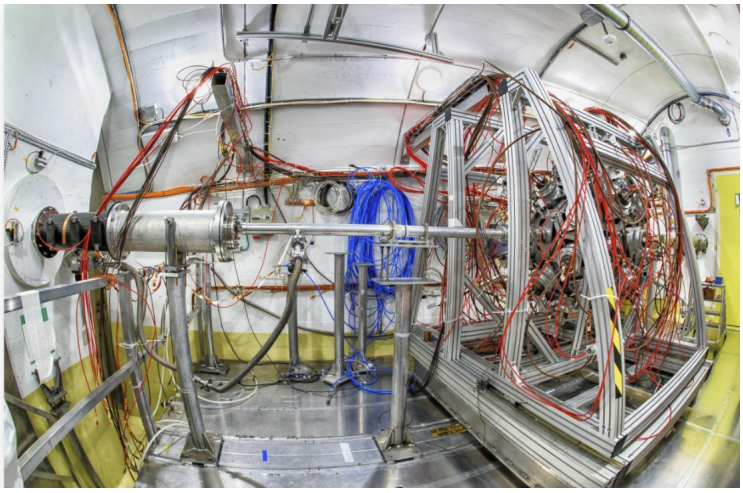

Figure 2.9: The first experimental area, EAR1 at n_TOF.

various safety systems, such as (antifire, overpressure, forced ventilation, decontamination area, etc ...).

At the exit of the experimental area, beyond the concrete wall that is 1.6 m thick, there is the fourth section called "escape lane", where the beam line ends. This area hosts the electronics and the data acquisition system (DAQ). In the whole tunnel, including the experimental area, a series of monitors are installed for checking various parameters, such as the pressure, temperature, radiation level, etc. All these parameters are constantly monitored through a visual interface program in the n_TOF Control Room, located outside the tunnel.

The beam vacuum tube ends on a 50 cm polyethylene block, usually called "beam dump". Neutrons are not completely absorbed by this block, but are partially thermalized and finally captured in the floor and in the tunnel walls.

2.5. The second beam line and the second experimental area, EAR2

The second experimental area, EAR2, is a complementary and at the same time independent area with respect to EAR1 and is one of the few experimental areas in the world using a vertical neutron beam. The floor of the experimental area is positioned on top of the target at a distance of 18.16 m with respect to its center, while the ceiling is at 23.66 m. The beam line elements from 0.2 to 3 m above the floor are easily exchangeable to meet the requirements of the different experiments. Removable vacuum pipes can be mounted along the beam line, with sizes matching the dimension of the beam as illustrated in Fig. 2.10 where the experimental bunker with a setup used for a background measurement is shown. The bunker of the experimental area has a surface of $40.8m^2$ and is 5.5 m in height. Adjacent to the experimental area, other rooms are avaliable for hosting the electronics and the data acquisition system.

Figure 2.10: The second experimental area, EAR2 at n_TOF.

Figure 2.11 shows a sketch of the second beam line. The beam tube has an inner diameter between 32 cm and 6 cm going from the spallation

target up. After crossing the experimental area, the neutron beam is "dumped" in a heavy structure on top of the EAR2 building. This beam dump consists of an iron core which slows down fast neutrons, surrounded by borated polyethylene that thermalizes and finally capture most of the neutrons in the vertical beam. As for the first beam line, a number of elements are mounted along the vertical line to shape the neutron beam. In details, a first 1 m cylindrical collimator made of iron is located about 10 m from the spallation target. A second 3 m long collimator is placed immediately below the floor of EAR2 (see Figure 2.12). For capture measurements a collimator with an internal diameter of 20 mm is used, while for the fission measurements a 60 mm diameter collimator is chosen. Both in fission and in capture mode, the collimators are conical and they are made of two sections, of 2 m iron and 1 m borated Polyethylene respectively.

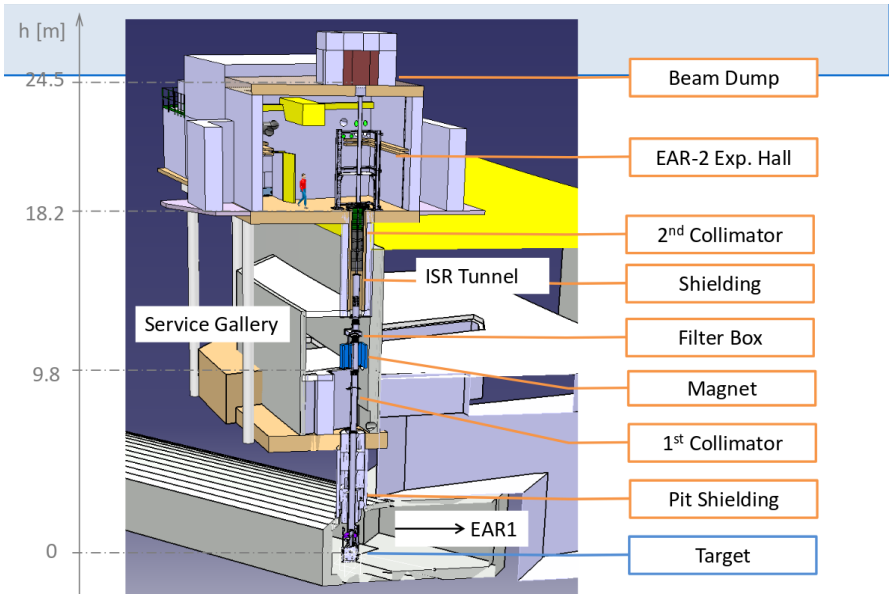

Figure 2.11: Schematic view of the second experimental area and the vertical beam line.

As EAR1, the second experimental area is classified as Class A Laboratory, adeguate for handling unsealed radioactive material. To this end, a dedicated ventilation system keeps the experimental area at an under-

pressure of 150 Pa with respect to the atmospheric pressure, whereas the changing room and the electronics room are held at 50 Pa and 100 Pa respectively, ensuring an appropriate confinement of potential radioactive contaminations. The area is also equipped with safety systems and radiation monitors.

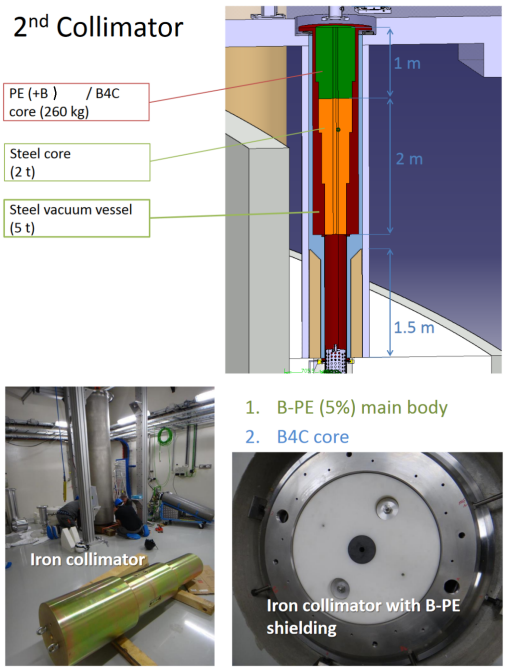

Figure 2.12: From top to bottom: a schematic view of the second collimator and its photos.

To complete the description of the second beam line it is important to consider two additional elements: a permanent magnet (0.2 T· m) and a filter station, similar to those installed in the horizontal beam line. The first one is used to remove charged particles from the neutron beam, while the second one is used in the measurements to check the level of background.

2.6. The facility features

The combination of all the elements in the n_TOF facility, starting from the spallation target all the way to the experimental areas, leads to the production of two neutron beams with unique characteristics suitable for high quality measurements of various neutron induced reactions (capture, fission, (n,cp), etc..). In particular, the high instantaneous flux, the high energy resolution and the low background are foundamental features for obtaining reliable neutron cross section data. Another positive aspect is the very wide neutron energy spectrum, which goes from the thermal region (25 meV) up to 1 GeV.

The upper panel of Figure 2.13 shows a comparison of the instantaneous flux (that is, the number of neutrons per pulse) for the major time of flight facilities in the world: n_TOF (EAR1 and EAR2), GELINA located in Geel (Belgium), LANSCE in Los Alamos (USA) and NFS in GANIL (France), while the bottom panel shows a comparison between the average neutron fluxes. The total number of neutrons produced in the spallation target from a single proton bunch and reaching EAR1 is orders of magnitude higher than the one presently avaliable in other existing facilities. The number is even higher in EAR2. The source intensity, i.e. the number of neutrons per second produced in the spallation target, allows the flight path to be considerably increased, keeping the average neutron flux comparable to the one of other facilities, while the instantaneous flux is three orders of magnitude higher, thanks to the very low repetition rate of the proton beam.

The energy resolution of a time of flight facility is given by:

$$\frac{\Delta E_n}{E_n} = 2 \times \sqrt{\left(\frac{\Delta T}{T}\right)^2 + \left(\frac{\Delta L}{L}\right)^2} \tag{2.5}$$

Therefore the use of a long flight path results in a very good energy resolution, which is important for studying the resonance structures in the cross sections. Due to a shorter flight path the neutron flux in EAR2 is 25/30 times higher than the one in EAR1, althought at the expense

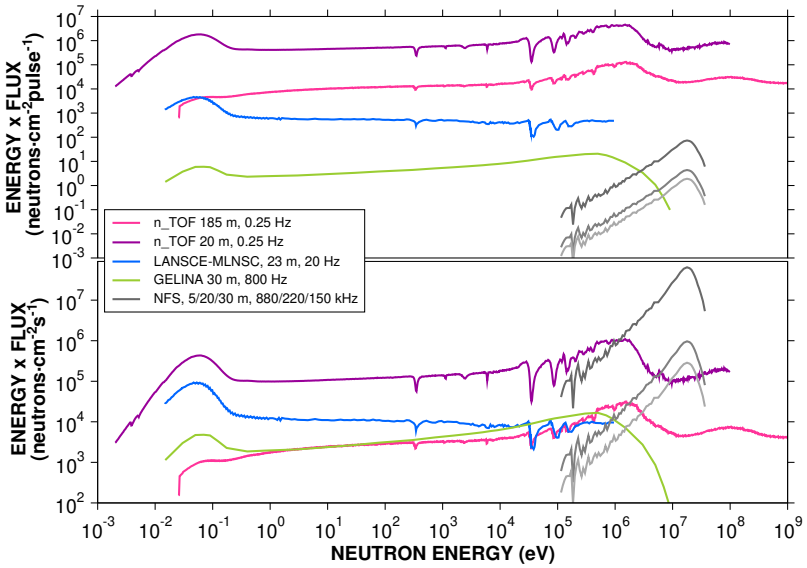

Figure 2.13: The upper panel shows a comparison of the instantaneous flux for the major time of flight facilities in the world: n_TOF (EAR1 and EAR2), GELINA located in Geel (Belgium) LANSCE in Los Alamos (USA) and NFS in GANIL (France), while the bottom panel shows a comparison between the average neutron flux [70]. All fluxes are expressed in units of lethargy.

of the energy resolution. The flux of the two experimental areas are compared in Figure 2.14, while in Table 2.1 the neutron flux present in EAR1 and EAR2 is reported for different energy intervals.

The higher neutron flux in EAR2 (relative to EAR1) allows to perform challenging measurements that cannot be carried out anywhere else. In particular, it makes possible to perform experiments with samples of very small mass (< 1 mg) of short-lived isotopes (i.e. highly radioactive sample) and of isotopes with small cross sections. The possibility to obtain samples with a mass smaller than 1 mg is essential for reducing the activity of isotopes with short half-life, or in case of rare materials. The very high flux of EAR2 also allows the use of very thin samples, a great benefit for the measurement of reactions leading to the emission of charged particles.

The EAR2 configuration has another very important advantage compared to EAR1: due to the shorter flight path in EAR2, the neutron time

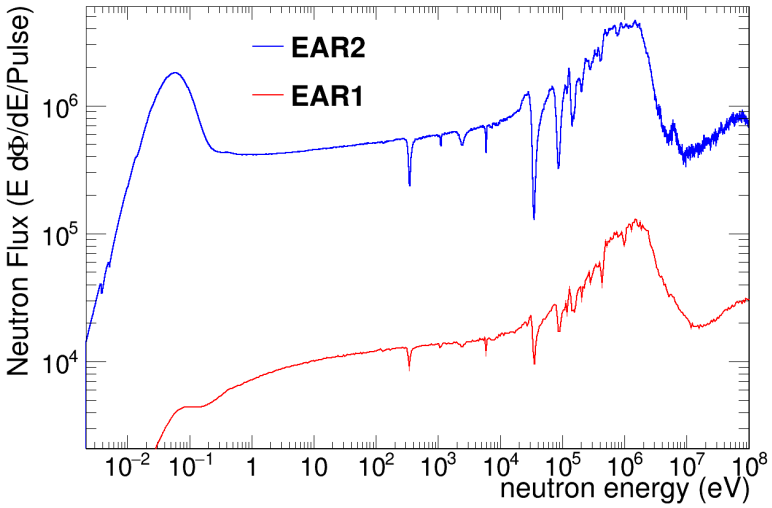

Figure 2.14: Comparison between the measured flux in EAR1 (in red) and EAR2 (in blue) [48].

Energetic range	EAR2 n/cm^2pulse	Statistic uncertainty [%]	EAR1 n/cm^2pulse [%]	Statistic uncertainty	Gain
0.02-10 eV	$1.64 \cdot 10^6$	2.0	$1.07 \cdot 10^5$	0.2	15.4
10 eV-1 keV	$1.07 \cdot 10^6$	1.4	$3.98 \cdot 10^4$	0.3	26.8
1 keV-100 keV	$1.36 \cdot 10^6$	1.3	$5.02 \cdot 10^4$	0.2	27.0
0.1-10 MeV	$3.00 \cdot 10^6$	0.9	$1.76 \cdot 10^5$	0.1	17.1
10-200 MeV	$4.78 \cdot 10^5$	2.0	$4.15 \cdot 10^4$	0.3	11.5
Total range (0.02 eV-200 MeV)	$7.54 \cdot 10^6$	0.6	$4.14 \cdot 10^5$	0.08	18.2

Table 2.1: Neutron flux in EAR1 and EAR2 for different energy ranges and the respective gains [71].

of flight at a given energy is ten times shorter than the one in EAR1. The smallest time of flight, in combination with the higher neutron flux, results in an increase of the ratio between the true signals and the background produced by the radioactivity of the sample. This characteristic is extremely important for studies of radioactive isotopes with a short half life, since in this case the intrinsic activity of the sample represents the dominant background component. All these features made possible the measurements of neutron-induced reactions on ^{7}Be and, in particular, the $^{7}Be(n,p)^{7}Li$ reaction presented in this thesis. The measurement was performed in EAR2 after a dedicated experimental campaign aimed at the characterization of the neutron beam. The results of such campaign are presented here below.

2.7. Characterization of the neutron beam in the second experimental area (EAR2) at n_TOF

In order to study the neutron-induced reaction cross sections, an accurate characterization of the neutron beam in terms of flux and its energy dependence, of the spatial beam profile, resolution function and background is needed. For this reason a large effort was devoted to the commissioning of the neutron beam in EAR2, with a series of dedicated measurements.

2.7.1 Determination of the neutron flux in the second experimental area at n_TOF-EAR2

Typically, the flux is defined as the number of neutrons crossing a surface of unit area in a second. At n_TOF, where the spatial profile of the neutron beam is not uniform and neutrons are distributed in low-frequency bunches ($\geq$ 0.8 Hz), it is more convenient to consider the number of neutrons per pulse of incident protons (with the nominal proton pulse made of 7 x 10^{12} protons), integrated over the whole spatial profile of the beam. A

Reaction	Standard energy range
$^{6}Li(n,t)$	0.0253 eV to 1 MeV
$^{10}B(n,\alpha)$	0.0253 eV to 1 MeV
$^{235}U(n,f)$	0.0253 eV and 0.15-200 MeV
$^{197}Au(n,\gamma)$	0.0253 eV and 0.2-2.5 MeV

Table 2.2: Neutron induced reactions used to characterize the neutron flux in EAR2 at n_TOF, and the energy range in which the respective cross sections are considered standard.

more suitable definition of this quantity would be "neutron intensity", but for simplicity we will refer to it as "the neutron flux". Furthermore, considering the wide energy spectrum of the neutron beam, it is important to express this flux as a function of the neutron energy. It should be noted that the knowledge of the neutron flux is extremely important for the determination of cross sections.

To determine the flux with high accuracy in a wide energy range, from thermal energy up to 100 MeV, a combination of several detection systems and neutron converting reactions, considered standards, are used.

The term "standard" identifies all neutron-induced reactions whose cross sections are smooth, large and accurately known in specific energy regions, and for this reason generally adopted as reference [72, 73]. The neutron induced reactions used to characterize the neutron flux, and the energy range in which the respective cross sections are considered standard are reported in Table 2.2.

The wide energy range of the n_TOF neutron beam makes it necessary to use different standard reactions in order to cover the full energy range. Furthermore, using different detectors, even for the same reaction, it is possible to minimize systematic uncertainties related, for example, to the detection efficiency.

For the characterization of the neutron flux in EAR2 different detectors have been used, in combination with the different reactions:

- A low-mass Silicon Monitor, SiMon2 [74], permanently installed in the neutron beam to continuously monitor the flux in any measure-

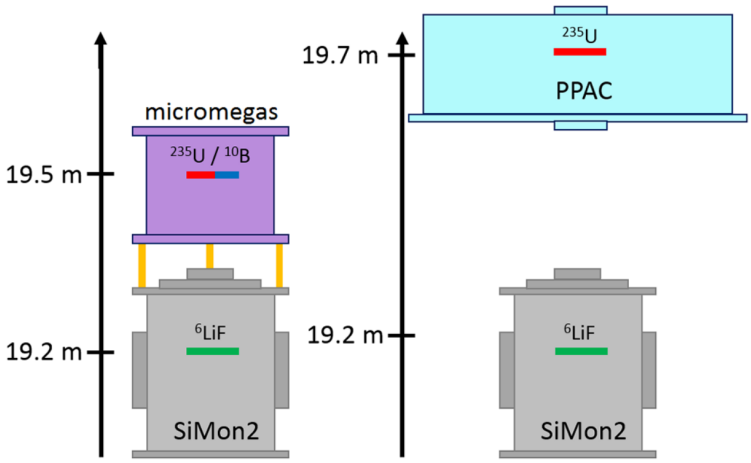

Figure 2.15: Scheme of the experimental setup for the neutron flux measurement. Two configurations were used, one based on Micromegas detectors (shown on the left), and the other one with PPACs (right panel). The SiMon2 chamber was always in place, located at 18.42 m from the spallation target. The flight paths of each neutron converter with respect to the spallation target is also reported.

ment. A more detailed description of this detector will be given in the next chapter where the experimental set-up used to determine the $^{7}Be(n,p)^{7}Li$ cross section is described;

- A gaseous detector, based on the MicroMegas microbulk technology [75, 76, 77] with a high signal-to-background ratio, high radiation resistance and low mass. The detector was equipped with samples of ^{10}B and ^{235}U, and filled with a mixture of Ar and CF_4 at atmospheric pressure.

- Finally, a set of position-sensitive Parallel Plate Avalanche Counters (PPAC [78, 79]) with ^{235}U deposits was used. The detectors are mounted on both sides of the deposit to detect fission fragments in coincidence. Figure 2.15 shows the two experimental setups adopted.

The evaluation of the neutron flux is made using this expression:

$$\Phi(E_n) = \frac{C(E_n) - B(E_n)}{\epsilon(E_n) \cdot (1 - e^{-n\sigma_t(E_n)}) \frac{\sigma_r(E_n)}{\sigma_t(E_n)}} \tag{2.6}$$

Where C(E_n) represents the total recorded number of counts per bunch and B(E_n) the background contribution in the bin centered at E_n, ϵ(E_n) is the efficiency for detecting the product of the neutron interaction, while σ_r and σ_t are, respectively, the reaction and total cross section for the isotope used as neutron converter.

The neutron kinetic energy in the equations above is determined from the time-of-flight according to the following relativistic expression:

$$(E_n(T)) = m_n \cdot c^2 \cdot (\frac{1}{\sqrt{1 - (\frac{L+\lambda(T)}{c \cdot T})^2}} - 1) \tag{2.7}$$

where T is the calibrated time-of-flight reconstructed from the signal, c the speed of light, m_n the neutron mass and L is the flight path length, i.e. the distance between the spallation target and the experimental area. This quantity is accurately calibrated by looking at the energy of the resonances in the $^{235}U(n, f)$ cross section. The quantity $\lambda(T)$ is related to an additional distance travelled by the neutron inside the spallation target and moderator circuit, and represents the so-called resolution function of the n_TOF neutron beam that will be discuss in the next section.

The comparison and combination of all measurements performed with the detectors described above allowed to determine the neutron flux in EAR2 from 2 meV to 100 MeV. The results of all measurements are shown in Figure 2.16 [48]. Since each measurement is affected by a few percent uncertainty on the absolute value of the flux, all measurements were re-normalized at thermal neutron energy, using the data from SiMon2 as reference. It should be considered, however, that for the purpose of the present measurement it is important to determine the shape of the neutron flux, i.e. its energy dependence, rather than its absolute value. In fact, in all measurements at n_TOF, the cross section of a given reaction is always extracted relative to a reference cross section, measured with the same setup. This technique is equivalent to determine the absolute

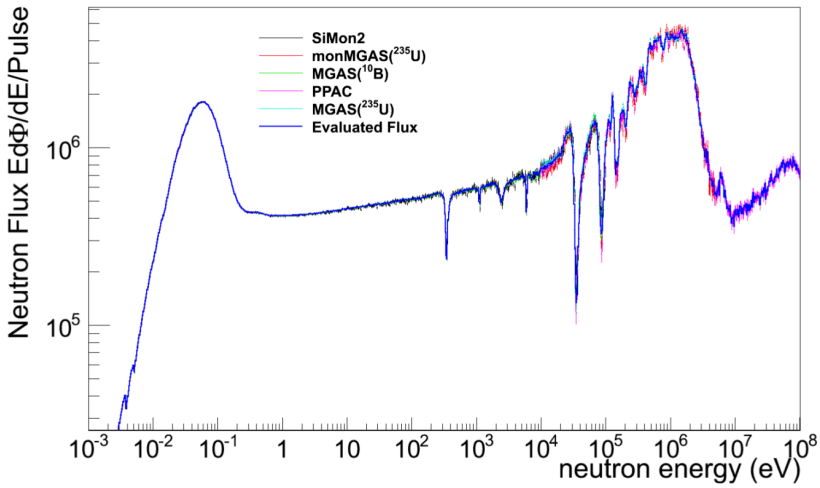

Figure 2.16: Results of all measurements performed for the neutron flux determination. The thick blue line corresponds to the evaluated flux. Each result has been normalized close to the thermal point to the value provided by the SiMon2 measurement [48].

value of the neutron flux in each measurement. As it will be shown in the following chapters, in the case of the $^{7}Be(n,p)$ cross section, the reference reaction is the $^{6}Li(n,t)$. For this reason, only the shape has to be accurately known "a priori".

2.7.2 Spatial Beam Profile

Another feature of the neutron beam that has to be determined with good accuracy for the measurement of the $^{7}Be(n,p)$ cross section in EAR2, is the spatial distribution or beam profile. In fact, the analysis of almost all measurements relies on the knowledge of the beam profile, especially if the samples have transverse dimensions smaller than the neutron beam dimension so that only a fraction of the beam is intercepted. This is indeed the case of the ^{7}Be sample, as shown in the next chapter. The measurements and results of the neutron beam profile in EAR2 are here briefly discussed. The neutron beam profile is determined by the geometry and distance of the collimators in the beam line. In particular the one

placed just before the experimental area, gives the desired spatial profile of the neutron beam. As previously mentioned, this collimator is made of two conical sections, that make the beam slightly convergent on a focal point, 1.08 m above the floor of the experimental area.

2.7.3 Beam profile simulations

The simulations done with FLUKA and GEANT4 show that the shape of the beam changes with the distance from the collimator.

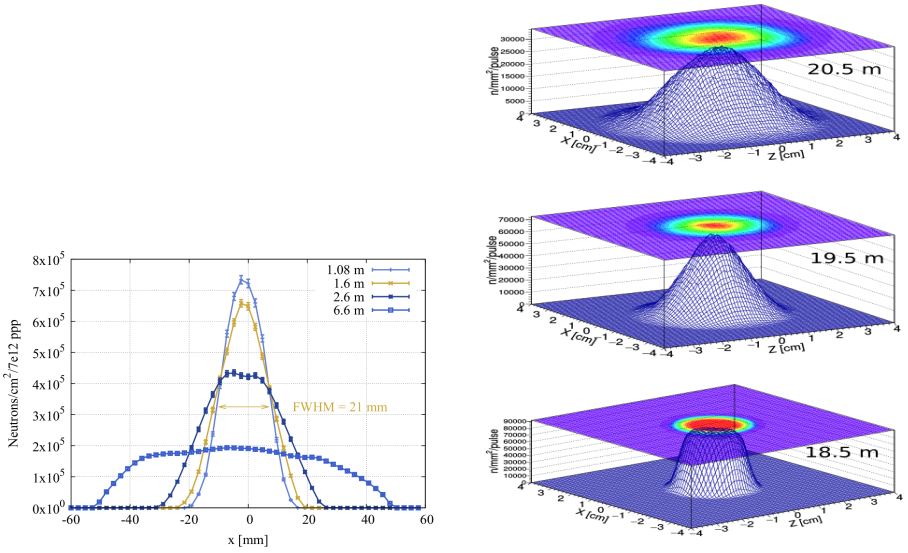

Figure 2.17: On the left, the neutron beam profile (projected on one direction) simulated at different heights in the experimental area, for thermal neutron energies [80]. The heights are given as distance from the floor of the experimental hall. The beam profile at the nominal capture sample position, 1.6 m from the floor, has FWHM = 21 mm. The neutron beam enters the beam dump at 6.6 m from the floor. On the right the simulated 3D beam profile in EAR2 at different flight paths is shown [81].

Figure 2.17, left panel, shows the projected neutron beam profile for thermal neutron energies at different heights from the floor of the experimental bunker. The curve at 6.6 m corresponds to the beam profile at the entrance to the beam dump. The right panel shows instead the simulations of the beam profile in 3D at different distances with respect to the exit of the collimator.

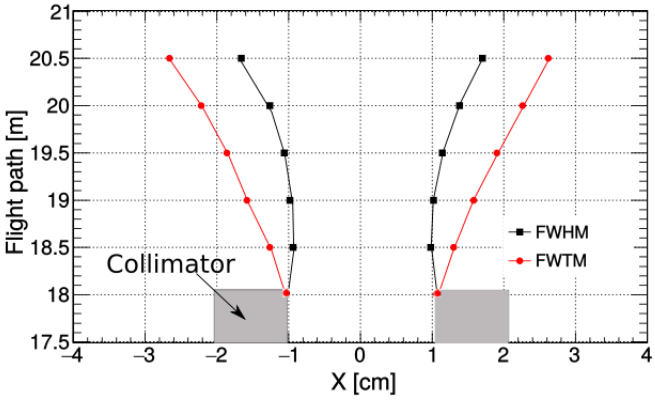

Figure 2.18: Limits of the neutron beam profile at one half (FWHM) and one tenth (FWTM) of the maximum for different flight path distances along EAR2 [81].

The beam profile changes from a 22 mm diameter flat distribution at 18.05 m flight path (i.e. at the entrance of the EAR2), to a Gaussian-like neutron beam with a FWTM of 36 and 50 mm at flight paths of 19.5 and 20.5 m respectively (i.e. 1.5 and 2.5 meters from the floor, approximately). The values of the beam size (in terms of FWHM and FWTM) as a function of the vertical flight path are displayed in Figure 2.18. It can be noted that the FWHM is smallest approximately 1 m above the collimator, where the focal point is located; while at the nominal sample position, 1.6 m above the floor, the beam FWHM increases and reaches the value of 2.1 cm [80]. It should be noted, however, that the beam has an important tail that makes the FWTM increase continously with the distance from the collimator.

The neutron beam profile for different TOF values is shown in Figure 2.19, for the nominal sample position. The beam halo at this position is 50 mm in diameter.

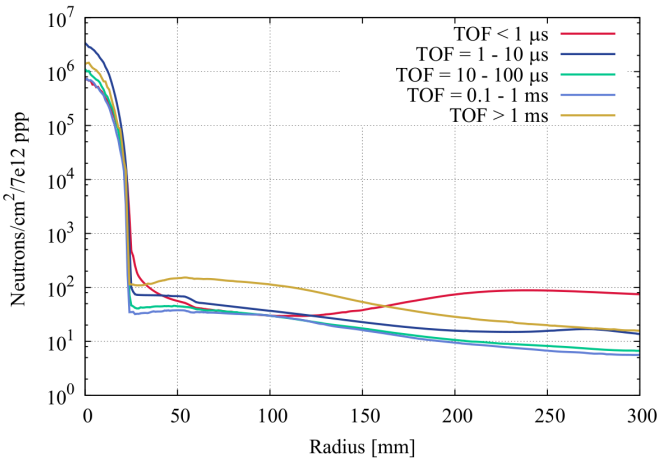

Figure 2.19: Neutron beam spatial distribution for different TOF ranges at 1.6 m from the floor of the experimental area. With all shielding elements installed, the neutron background is 4-5 orders of magnitude smaller than the peak of the profile [80].

2.7.4 Beam profile measurement

In addition to simulations, beam profile measurements have been performed in EAR2 with the small collimator. Three detection systems have been used in the measurements: the PPAC monitor (2015), SiMon2D monitor (2017) and XY-Micromegas (2017). Photos of the detectors are shown in Figure 2.20.

Figure 2.20: The three detection systems used for the beam profile measurement in EAR2.

PPAC monitor beam profile measurement

The Parallel Plate Avalanche Counters used for the measurements of the neutron flux have also been used to measure the beam profile, thanks to the position sensitivity of the detectors. The configuration used in EAR2 consists of 3 PPACs and 2 ^{235}U targets mounted perpendicular to the neutron beam.

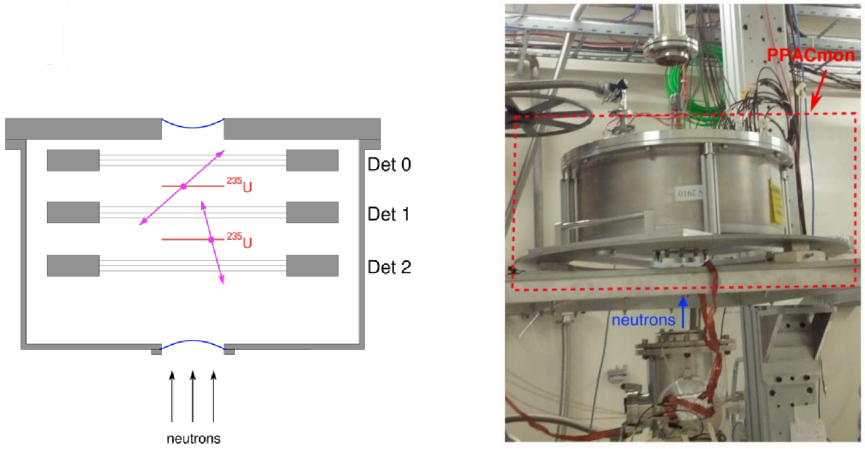

Figure 2.21: Sketch of the PPAC monitor and the setup mounted on the beam line in EAR2.

Each ^{235}U target, deposited on a 0.7μm aluminium backing with a thickness of $\sim 70\mu g/cm^2$, is surrounded by 2 PPACs so that fission events can be selected by the coincident detection of the two fission fragments. This coincidence method is highly selective on fission reactions, rejecting alpha particles from the radioactive decay of the samples. A sketch of the configuration and the set-up used in EAR2 are reported in Figure 2.21.

The beam profile can be reconstructed taking into account the hit positions on the two PPACs (Det 1 and Det 2 in Figure 2.21). The position distributions of the fission fragments are shown in Figure 2.22, while the beam profile reconstruction, based on the back to back emission of fission fragments, is reported in Figure 2.23. More details on the measurement and analysis of the beam profile made with the PPAC are reported in Ref. [82]. The measurement with the PPAC gives the most accurate and high

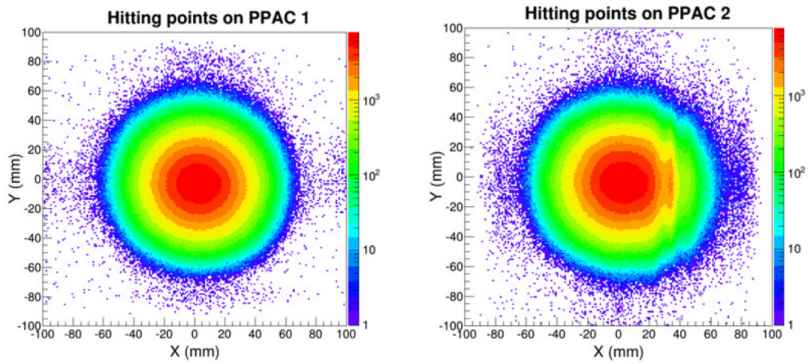

Figure 2.22: Fission fragment position distribution on PPAC and PPAC 2 (left and right respectively) [82].

resolution results on the beam profile. However, additional measurements have been performed for confirmation.

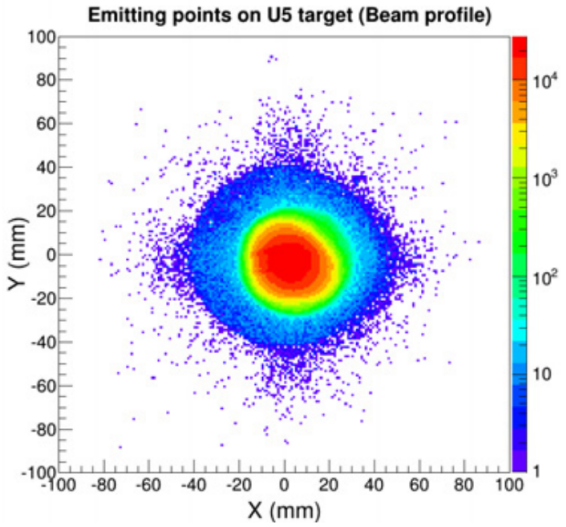

Figure 2.23: Neutron beam profile in EAR2 measured with the PPAC system [82].

SiMon2D and XY-Micromegas beam profile measurement

The neutron beam profile monitor SiMon2D is a 16 × 16 strips double sided silicon detector having 5 x 5 cm^2 total active area and 500 μm

FWHM-X Profiles LOWER POSITION				
Energy range (eV)	MicroMegas	SiMon2D	PPAC	Simulations
0.001-0.01	25.9	29.1		25.0
0.01-0.1	25.7	29.1	24.9	23.1
0.1-1	25.8	29.7	25.2	23.0
1-10	26.2	29.6	26.6	23.3
10-10^2			25.9	23.4
10^2-10^3			25.7	23.5
10^3-10^4			26.3	23.9
10^4-10^5			25.7	23.4
10^5-10^6			25.1	23.6
10^6-10^7			23.5	24.2
FWHM-Y Profiles LOWER POSITION				
Energy range (eV)	MicroMegas	SiMon2D	PPAC	Simulations
0.001-0.01	25.0	25.2		24.2
0.01-0.1	24.4	28.8	24.6	24.4
0.1-1	25.1	29.3	25.0	24.3
1-10	24.7	29.1	26.2	23.3
10-10^2			25.8	25.2
10^2-10^3			25.4	25.4
10^3-10^4			25.9	23.5
10^4-10^5			25.8	24.1
10^5-10^6			24.5	24.7
10^6-10^7			25.2	26.1

Table 2.3: Comparison at the lower-position (19.5 m flight path) between FWHM simulated and measured with MicroMegas, SiMon2D and PPAC detectors in the second experimental area (EAR2) [83].

thickness [84] (the strips on the two faces are perpendicular to each other).

In order to measure the neutron beam profile, a ^{6}LiF converter layer, deposited onto a carbon fibre plate (1 mm thick) is placed in front of the detectors as shown in Figure 2.24. The converting reaction is:

$$^6Li + n \Rightarrow^3 H(2.73MeV) + \alpha(2.05MeV) \tag{2.8}$$

The XY-Micromegas detector is a position-sensitive gaseous detector, [85], made of 58 x 59 strips covering a 36 cm^2 area and filled with a

FWHM-X Profiles UPPER POSITION			
Energy range (eV)	MicroMegas	SiMon2D	Simulations
0.001-0.01	28.6	32.8	28.1
0.01-0.1	28.2	30.6	26.8
0.1-1	28.8	32.2	26.7
1-10	26.5	32.4	27.7
FWHM-Y Profiles UPPER POSITION			
Energy range (eV)	MicroMegas	SiMon2D	Simulations
0.001-0.01	26.6	31.3	27.4
0.01-0.1	26.1	29.4	26.9
0.1-1	27.1	29.1	28.0
1-10	26.7	31.1	28.3

Table 2.4: Comparison at the upper-position (19.82 m flight path) between FWHM simulated and mesured with MicroMegas, SiMon2D and PPAC detectors in the second experimental area (EAR2) at n_TOF [83].

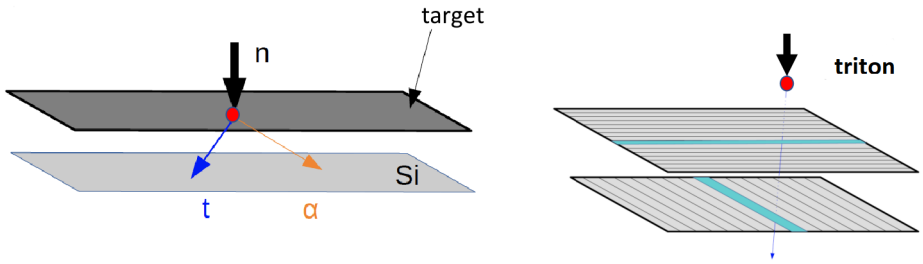

Figure 2.24: Scheme of the interaction of the incoming neutron with the converter layer and detection of the produced particles in coincidences between the xy strips in the SiMon 2D detector.

mixture of argon-isobutane at atmospheric pressure. It consists of a drift gap of 3 mm and an amplification gap of 100 mm, separated by a 5 mm thick nickel micromesh. A deposit of ^{235}U was used as neutron converter.

For the measurement of the beam profile, these detectors were mounted in EAR2 in two configurations as shown in Figure 2.25. In the first one, Config. A, SiMon2D was placed in lower position with respect to the Micromegas detector, facing directly the neutron beam coming from the bottom, while in the second configuration, Config. B, the position of the detectors is inverted.

In order to extract the beam profile with SiMon2D, coincidence events

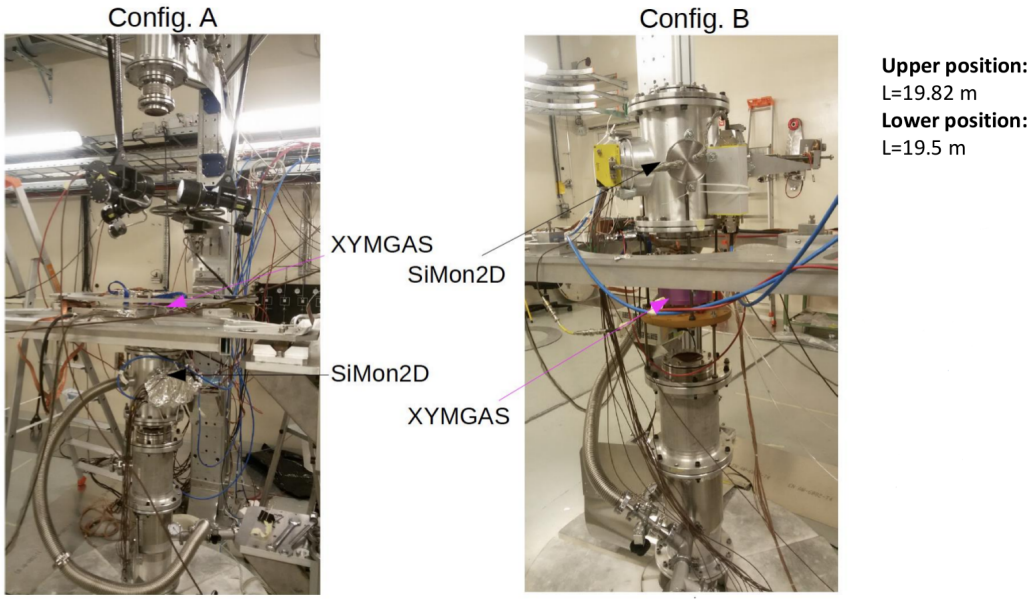

Figure 2.25: The two configurations used for the beam profile measurement with SiMon 2D and XY-Micromegas. In Config. A SiMon2D is at the lower position, at 19.5 m respect to the spallation target, while the XY MicroMegas is in the upper part at 19.82 m from the spallation target. In Config. B the position of the two detectors are inverted.

between strips on the front side and on the back side were taken in consideration. As shown in Figure 2.26, the triton peak is well separated from the alpha particle peak and from the signals induced by background and electronic noise, and therefore in the data analysis only the triton peak was used as a signature of the neutron hitting the detector.

With the XY MicroMegas, the analysis procedure consists in identifying signals caused by the fission fragments produced by the interaction of neutrons with the ^{235}U converter. For every interaction, the position was identified by considering the strip that had a signal. As for the PPAC, apart from the position, the SiMon2D and XY-Micromegas detector provide also a time information that allows to study the beam profile as a function of the time-of-flight and therefore of the neutron energy.

Contrary to the PPAC, SiMon2D and XY MicroMegas could provide accurate data only up to 10 eV, since beyond this energy they are not

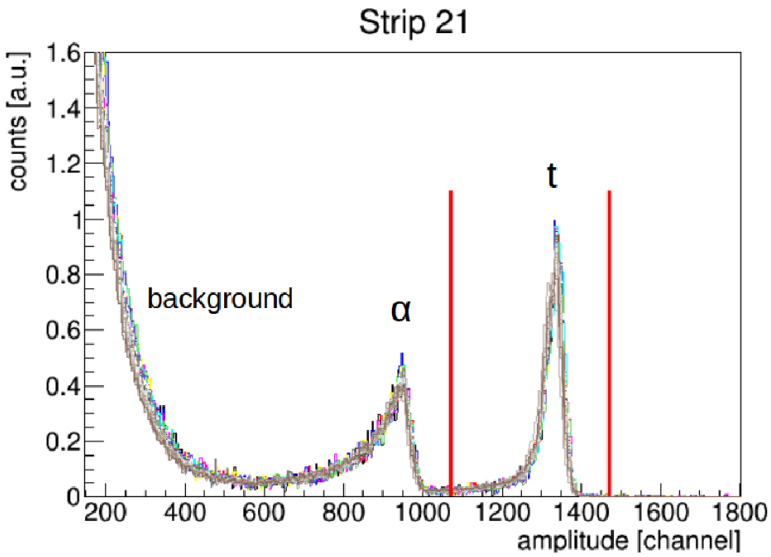

Figure 2.26: Amplitude spectrum for strip 21 and for different runs: each run is drawn in a different color in order to check the stability of the response of the detector.

reliable anymore because of various problems affecting the detectors at smaller time-of-flights. The profile integrated over the whole energy range obtained with SiMon2D and XY MicroMegas is shown in Figure 2.27.

To compare all measured profiles in a consistent way, the central part of the 2D distribution was projected on each dimension (X and Y) and fitted with the function:

$$F(x) = bgr + A * [Erf(\frac{a + (x - x_0)}{\sqrt{2}\sigma_1}) + Erf(\frac{a - (x - x_0)}{\sqrt{2}\sigma_2})] \qquad (2.9)$$

Here A is a normalization factor, α is the size of the step function chosen (the plateau), σ_1 and σ_2 are the standard deviations, different for the two error functions to account for asymmetries in the profile, and Erf is the following function:

$$Erf(u) = \frac{2}{\sqrt{\pi}} \int_0^u e^{-t^2} dt \qquad (2.10)$$

As an example, Figure 2.28 shows the distribution of counts on the strips

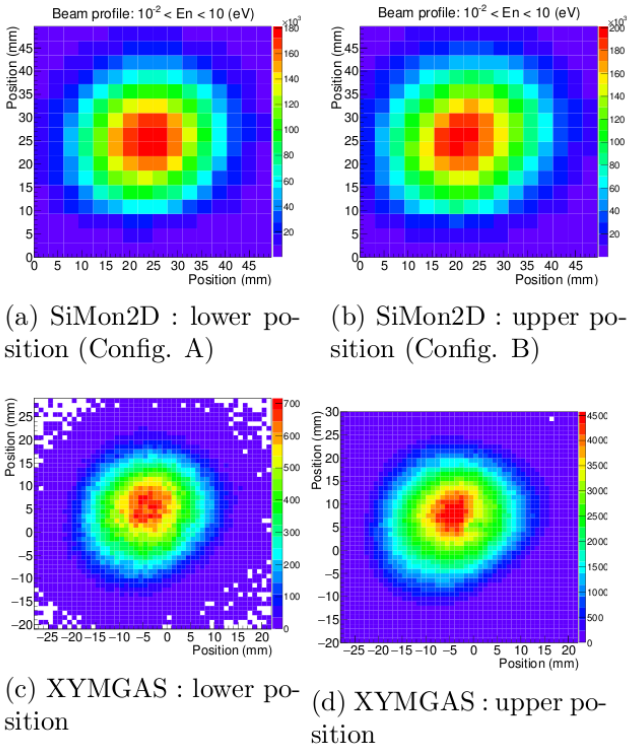

(a) SiMon2D : lower position (Config. A)

(b) SiMon2D : upper position (Config. B)

(c) XYMGAS : lower position

(d) XYMGAS : upper position

Figure 2.27: Beam profile obtained with SiMon2D and XYMGAS for both configurations [83].

in the Y direction, when the central strip in the X direction is selected.

The measurements of the beam profile in EAR2 confirm the shape predicted by the simulations. When comparing the FWHM (or sigma) extracted with Eq. 2.9, an agreement between the simulations and the measurement of around 10% is found. Table 2.3 and 2.4 show a comparison between the width of the neutron beam in the X and Y directions simulated and measured with Micromegas, SiMon2D and PPAC, at 19.5 m flight path (lower position) and at 19.82 m (upper position) respectively. Considering that the measurements validate the simulated beam profile, in the analysis of the $^{7}Be(n,p)$ reaction, only the simulated beam profile was used, since Monte Carlo simulations provide a spatial distribution with high statistics, as a function of neutron energy.

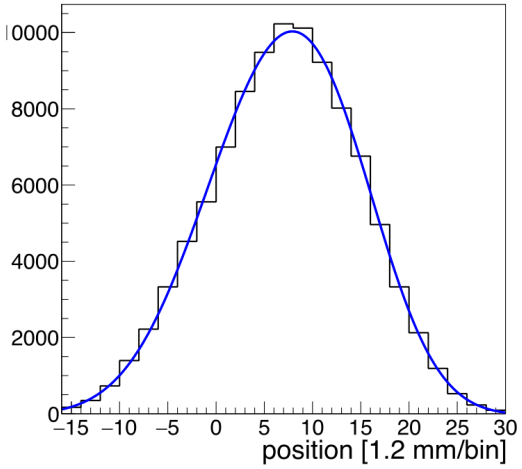

Figure 2.28: Fit of the XY MicroMegas middle strip with the function of equation 2.9 [83].

2.7.5 Resolution function

A common feature of neutron time-of-flight facilities is the fact that neutrons of a given energy do not exit the target-moderator assembly at the same time, thus making the time-to-energy relation non-univocal [81]. This is particularly true for spallation neutron sources, whose production target has large dimensions and neutrons spend more time inside it before entering the beam line. Althogh in the measurement of the $^{7}Be(n,p)$ cross section the resolution function does not play an important role (since there are no resonances), for completeness the Resolution Function in EAR2 at n_TOF is here briefly described.

As schematically shown in Figure 2.29, a neutron with real energy E_n corresponds to an ideal time of flight t_i for a fixed flight path length L. The resolution function $R(t_m,t_i)$ relates the ideal time-of-flight t_i to the measured one t_m and transforms an ideal time-of-flight spectrum $S_i(t_i)$ to a measured time-of-flight spectrum $S_m(t_m)$:

$$S_m(t_m) = \int S_i(t_i)R(t_m,t_i)dt_i; \tag{2.11}$$

Over a short energy range, the response function is considered constant.

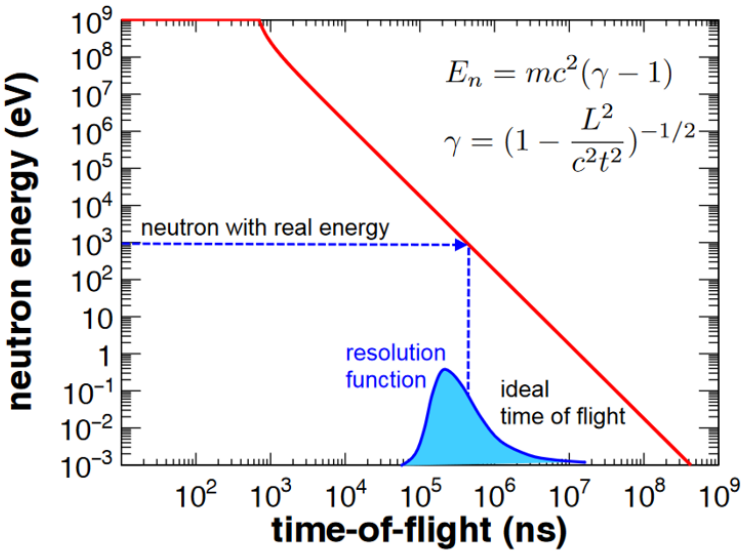

Figure 2.29: In red, the ideal relation between the energy and the time of flight of a neutron. In blue, the resolution function.

The integral becomes a convolution:

$$S_m(t_m) = \int S_i(t_i) R(t_m, t_i) dt_i = S_i(t_i) * R(t_m); \tag{2.12}$$

where R is called Resolution Function (RF). Effectively, in a time-of-flight facility, the resolution function indicates the uncertainty in the reconstructed neutron energy for a fixed time-of-flight. Since this broadening affects the shape of resonances in the cross sections, it has to be determined with good accuracy in order to make a reliable R-matrix fit of the resonances and extract accurate resonance parameters. The spread of the true neutron energy for a given time-of-flight, shown in Figure 2.29, is caused by the stochastic moderation process of neutrons undergo inside the spallation source and the moderation circuit. This spread can be expressed as an additional effective flight path:

$$l = v \times t_{mod} \tag{2.13}$$

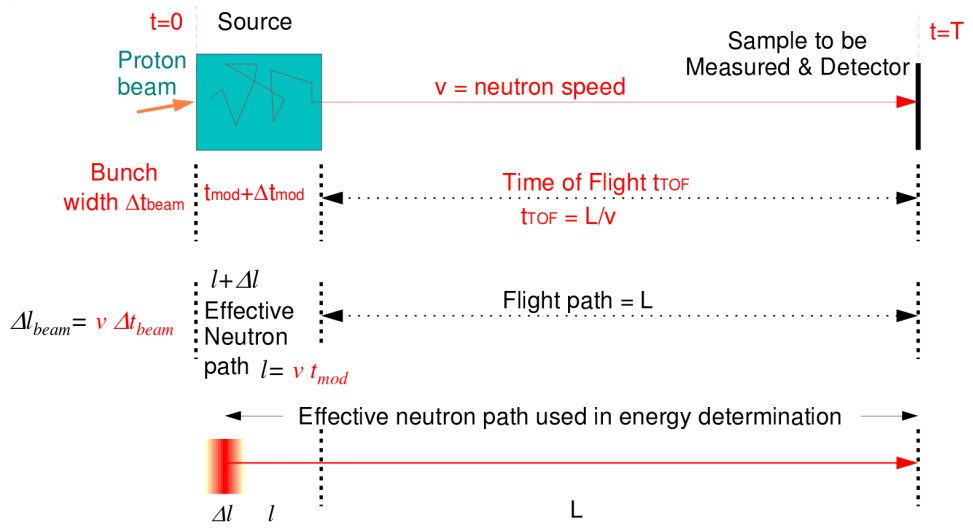

Figure 2.30: Sketch of the flight path that neutrons have to travel from the spallation source to the sample to be detected.

that neutrons have to travel inside the target and the moderator system before entering the beam line (see Figure 2.30). In Eq. (2.13), t_{mod} is the moderation time, i.e. the time spent by the neutron inside the target-moderator assembly. This means that one can consider $L + l$ as the total neutron flight path and the neutron velocity v is derived from the effective neutron path $v = (L + l)/t$ with an uncertainty $\Delta v = \Delta l/t$.

The Resolution Function (RF) can only be determined by means of simulations, which can then be validated with experimental data. The resolution function of the neutron beam in EAR2 is displayed in Figure 2.31. In this figure one can already see that the relative time spread is larger for thermal energies and above 10 MeV; consequently, these energy ranges present a lower energy resolution. Quantitatively, this resolution is around 2% at thermal energy, decreasing to a few per thousand in the eV and keV region and increasing again to several percent at high energy, due to the time resolution of the proton beam.

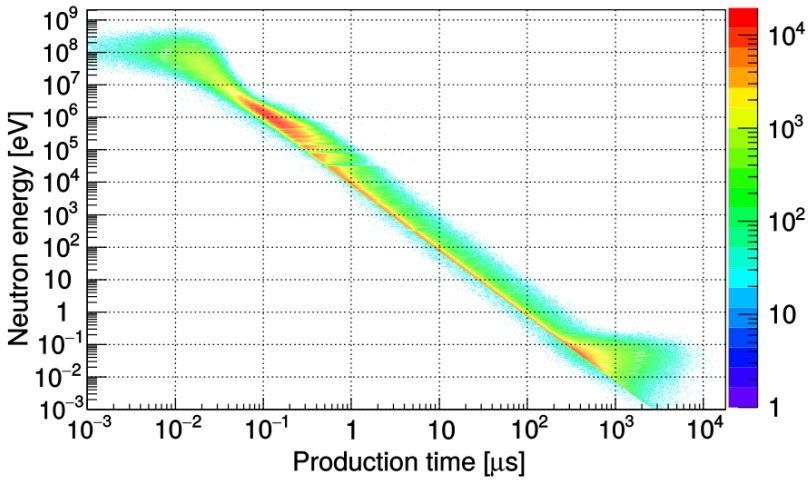

Figure 2.31: Resolution function of the n_TOF-EAR2 neutron beam expressed in the form of neutron energy vs production time (i.e. time of arrival to a plane 1.5 m above the center of the target) [80].

Chapter 3

Experimental setup for the measurement of the ^{7}Be(n,p)^{7}Li reaction at n_TOF

As mentioned in Chapter 2, in July 2014 the second experimental area (EAR2) of the n_TOF spallation neutron-time-of-flight facility at CERN came into operation. The main advantage of EAR2 consists in a flux up to 40 times higher than in EAR1. The combination of the higher flux with a time-of-flight (for a given energy) 10 times lower due to the shorter flight-path, results in more than two orders of magnitude higher signal-to-background ratio for radioactive samples. These features of the EAR2 neutron beam, opened the way to measurements of neutron-induced reactions on very thin samples, reactions with a low cross sections or radioactive isotopes with short half-life. In view of these properties, EAR2 was immediately considered the ideal place for measuring neutron-induced reactions on ^{7}Be ($t_{1/2}$ = 53 days) of interest for the Cosmological Lithium Problem.

The first experiment done at EAR2 was the measurement of the $^{7}Be(n,\alpha)^{4}He$ cross-section [49]. As already discussed in the Introduction, the results indicated that the cross section of this reaction was too low to significantly affect the abundance of primordial Lithium. The last piece

of information missing in investigating a Nuclear solution of the CLiP was an accurate measurement of the $^7Be(n,p)^7Li$ reaction cross-section. As shown in Chapter 1, only few and highly discrepant data exist on this reaction, dating back to the 80's and covering only partially the neutron energy region of interest for the Big Bang Nucleosynthesis.
The features of the neutron beam in EAR2 provided the unique opportunity of a high quality direct measurement of the $^7Be(n,p)^7Li$ cross-section. This chapter describes the experimental set-up, the ^{7}Be sample preparation and the procedure used in the measurement.

3.1. Experimental setup

The (n,p) reaction has two peculiarities:

- on one hand it has a higher cross section, of thousand of barns, at thermal energy and several barns in the range of BBN interest (from $\sim$ 20 keV to $\sim$ 200 keV);

- the emitted protons have a low energy, slightly above 1 MeV, consequence of the low Q-value of the reaction.

While the first feature makes the measurement relatively easy in terms of sample mass and activity (as it will be discussed later on), the low energy of the emitted protons represents a challenge since it requires a low noise and a high sensitivity detector set-up. In the following, the detectors specifically designed for this measurement and the procedure used for the sample preparation are described.

3.1.1 The Silicon Monitor, SiMon2

In order to measure the neutron flux in EAR2, an essential information for the measurement of the $^7Be(n,p)^7Li$ cross section, a silicon monitor was used: SiMon2.

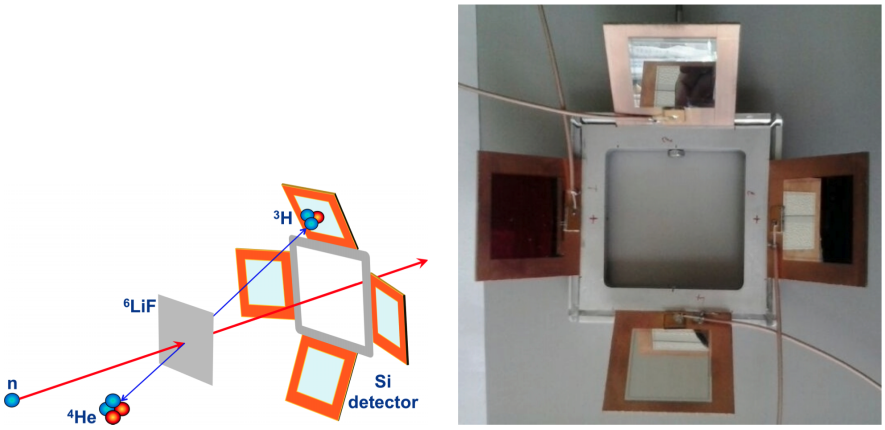

Figure 3.1: Left panel: a schematic drawing of the SiMon2 neutron beam monitor. Right panel: a photo of the four silicon detectors.

This device was suitably designed to minimize the amount of material inserted into the beam. It consists of a thin neutron converter target, placed in the beam and surrounded by four silicon detectors that are out of the beam, as shown in Figure 3.1. The detector is housed in an aluminum vacuum chamber (with pressure of the order of 10^{-2} mbar), as shown in Figure 3.2.

The measurement and monitoring of the neutron flux are based on the detection of products from the neutron-induced reaction on ^{6}Li:

$$n +^6 Li \Rightarrow \alpha + t + Q \tag{3.1}$$

with a Q value positive and equal to 4.78 MeV. For neutrons of thermal energy the products are emitted in opposite directions and the kinetic energy is 2.73 MeV for the tritons and 2.05 MeV for the α particles. The reaction n+^{6}Li is therefore particularly convenient, both because it is characterized by a high cross section (from approximately 1000 barn to some barn in the range of interest), known with an accuracy of around 0.5 %, and because the products of the reaction are charged and with an energy, in principle, easily discriminable from the background. The charged particles generated by the interaction of the neutron with the converter, reach the Silicons (according to the geometric acceptance of

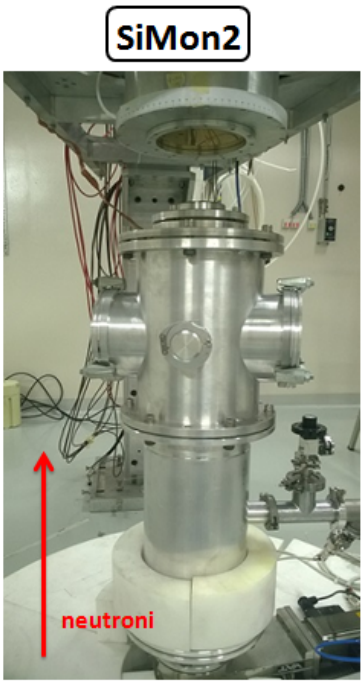

Figure 3.2: The aluminum chamber of SiMon2 mounted on the vertical neutron beam line in EAR2.

the detector) and are stopped inside, depositing their full energy.

The choice of the target thickness represents a compromise between the need to have a high count rate and the possibility to identify the tritons and the α particles, identification that is worsened by the energy loss of the particles inside the converter itself. In order to obtain the right thickness, Monte Carlo simulations were performed with the GEANT-4 toolkit, as reported in Ref. [63]. In particular, simulations were performed for a deposit of ^{6}LiF, instead of a pure ^{6}Li. In fact, since pure Lithium is a highly reactive metal and it oxidizes when exposed to air, the use of one of its compounds is a convenient alternative. For very thin deposits, alpha particles and tritons can be clearly identified on the basis of their well separated deposited energy but, the corresponding counting statistic is low and may be not sufficient for a precise flux measurement in particular energy regions, i.e. where the reaction cross section is small.

Typically, tritons produce a peak centered at 2.5-2.6 MeV, as they

lose only a small fraction of their energy within the deposit. On the contrary, due to their higher loss of energy, the alpha particles show a wider spectrum that reflects the uniform distribution of their production within the Li deposit. Thus when the thickness of the layer increases, the number of reactions in the converter increases, but the energy resolution becomes worse due to the energy loss of the reaction products in the converter itself. Moreover, for very thick layers, some particles can be completely absorbed inside the deposit, leading to a saturation in the number of detected events.

The results of the simulations indicate that a deposit of pure ^{6}Li can be more convenient in terms of alpha/triton separation and efficiency, provided that an appropriate protection is used to prevent the degradation of the pure Lithium deposit, highly hygroscopic. On the other hand, if a high count-rate is not required, a LiF target is more appropriate in terms of implementation and manageability.

The target used in SiMon2 is a LiF deposit of thickness of 420μg/cm^2 and Figure 3.3 shows a comparison between data and simulations of the deposited energy spectrum of tritons and alpha particles. As it can be seen from the figure, the regions corresponding to α and t are well separated.

Unlike the pure ^{6}Li, the LiF is not reactive with air but compared to pure ^{6}Li it has the disadvantage of having less ^{6}Li nuclei for the same deposited total mass. In any case, this is not a limitation because the high flux in EAR2 ensures an absolutely satisfactory yield and counting statistics.

The silicon detectors used in SiMon2 have 3 x 3 cm^2 surface and thickness of 300 μm each. The detector is coupled to a dedicated electronics, able to handle the count-rate and avoid or minimize problems such as pile-up and dead-time. In particular, the charge produced in the Silicons is collected and amplified by charge preamplifiers and, subsequently, by fast Timing Filter Amplifier (ORTEC TFA 474) with formation times of 100 ns. The signals thus obtained are recorded by the n_TOF acquisition system that uses Flash Analogue to Digital Converter (FADC), in which they are

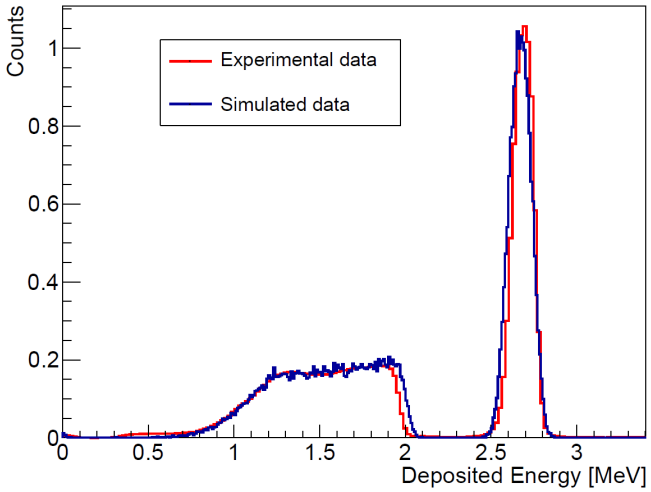

Figure 3.3: Comparison between the simulated and the experimental deposited energy spectrum for a LiF deposit of 420 μg/cm^2 thick in one of the silicon detectors of SiMon2 [71].

digitized.

3.1.2 The Silicon Telescope

The main goal of the setup used in the measurement is the identification of the emitted 1.44 MeV protons as a signature of the $^7Be(n,p)^7Li$ reaction. To this aim, a silicon telescope detector was chosen. Both ΔE and E stages have an active area of 5x5 cm^2 and are made of 16 strips 3 mm wide and 50 mm long, with an inter-strip gap of 0.1 mm. The thickness is 20 and 300 μm for the ΔE and E detectors respectively, with a 7 mm distance between the two.
The telescope was mounted at a polar angle of 90 degrees relative to the beam direction, at a distance from the center of the sample of 5 cm. To minimize the energy straggling of emitted protons inside the ^{7}Be deposit, the sample was tilted relative to the neutron beam direction by 45 degrees. The use of strip detectors has two main advantages:

- it minimizes pile-up of 478 keV γ-rays produced in the natural decay of the ^{7}Be target nuclei into ^{7}Li, thus reducing the background issue;

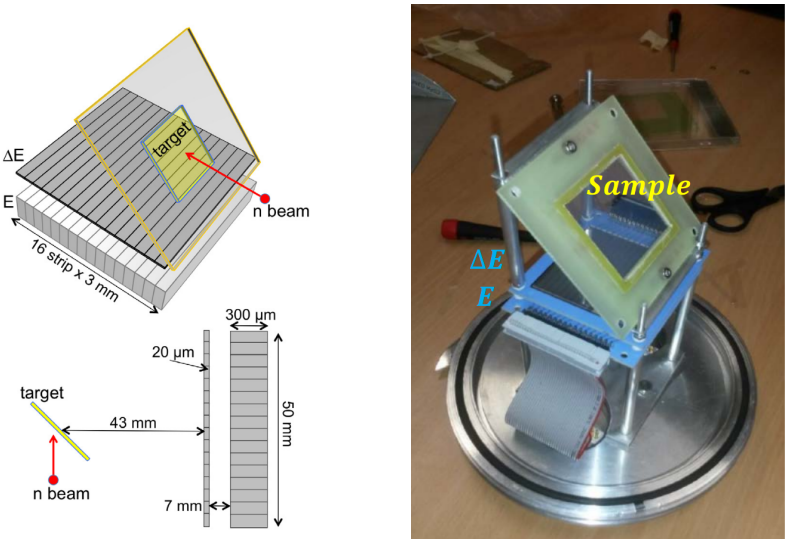

Figure 3.4: Left panel: 3D sketch (top) and vertical profile (bottom) of the detector setup. The drawings are not to scale, and the ΔE and E thicknesses are exaggerated for clarity. On the right a photo of the detector setup on the bench before installation.

- it minimizes the large prompt signal generated by γ-rays and relativistic charged particles produced in the n_TOF spallation target (the so-called γ-flash).

These issues would have caused a limitation on the performance of the set-up. In Fig. 3.4, left panel, a 3D sketch and a vertical profile of the experimental setup are shown, not in scale and with exaggerated thickness of the E and ΔE silicon detectors for better clarity. On the right panel, a photo of the real setup on the bench before its installation in EAR2 is showed. The Silicon Telescope was housed in an aluminum chamber in vacuum (10^{-2} mbar). Figure 3.5 (left panel) shows the housing of the ^{7}Be target in the aluminum chamber. The choice of silicon detectors was made because they have a low sensitivity to γ-rays and scattered neutrons, indeed γ-rays and neutrons up to 1 MeV basically produce low amplitude signals with an interaction probability $< 10^{-3}$-10^{-4}. Furthermore, since they can practically interact only with one of the elements of a telescope, they are efficiently rejected by the coincidence technique between ΔE and E detectors.

Figure 3.5: Left panel: the insertion of the ^{7}Be in the aluminum chamber. Right panel: the vacuum chamber with the front-end electronics, installed on the vertical neutron beam line in EAR2. The target and the telescope detector are inside.

Finally the choice of a strip-like geometry was made to:

- allow a rejection of spurious background by means of a more selective geometrical choice of the ΔE-E coincidences;
- have a better tool to evaluate the geometrical efficiency and the target alignment from the data, which can be easily compared with numerical simulations;
- check the expected isotropy of the angular distribution of the emitted protons.

The target and the telescope, inside the aluminum scattering chamber, were installed on the vertical neutron beam line in EAR2. Fig. 3.5 shows the chamber in beam, with the front-end electronics boxes also visible. A standard commercial front-end and readout electronics was chosen for the setup. The preamplifiers consisted of 16 units of CAEN-A1422H-F3 [86] for the ΔE stage (90 mV/MeV gain) and 16 units of CSPA 03M.02a [87] for the E stage (50 mV/MeV gain). The rise time of the signals

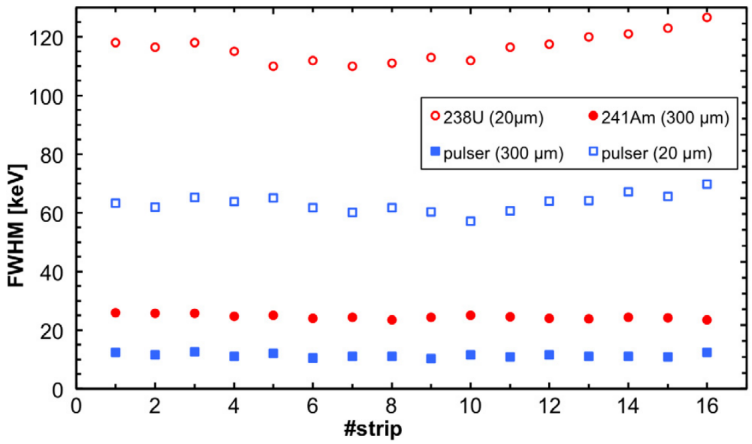

Figure 3.6: Resolution of each ΔE and E detector strip, tested with a pulser and with α particles from ^{238}U (for the ΔE detector) and ^{241}Am (for the E detector).

from the preamplifiers used for the ΔE and E stages were 100 and 50 ns respectively. Two 16-channel CAEN-N568B modules were used as shaping amplifiers and their shaping time was optimized at 0.2 μs. The analog signals were then digitized using flash ADCs with up to 14 bit resolution and up to 2 GHz sampling rate. The ΔE and E silicon detectors, along with the front-end electronics, were tested on the bench by means of α -sources. The behavior of the energy resolution was rather uniform for all strips as it can be seen in Fig. 3.6, showing the FWHM resolution for each ΔE and E detector strip tested with a pulser and with ^{238}U source (for the ΔE detector) and ^{241}Am source (for the E detector).

3.2. Sample preparation

One of the issues of this measurement was the preparation and characterization of the ^{7}Be target. As already mentioned, the $^{7}Be(n,p)^{7}Li$ reaction has a very high thermal cross-section (several 10^4 b) and this feature allows the use of a small mass ^{7}Be sample (few ng). But, on the other hand, the $^{7}Be(n,p)^{7}Li$ reaction produces rather low-energy protons of 1.44 MeV which could be easily confused with background from other reaction channels on the sample backing or contaminants. For this reason,

one of the requirements for the measurement was to use a target material as pure as possible and distributed over a thin layer.
Implantation of mass separated ^{7}Be appeared to be the best technique to produce a sample with suitable purity and homogeneity. To this aim, ^{7}Be had to be produced, chemically purified and isotopically separated before being implanted. Such a preparation required a joint effort of two different laboratories, namely Paul Scherrer Institut (PSI) and Isolde.

3.2.1 Preparation of the starting ^{7}Be material

Beryllium isotopes (^{7,9,10}Be) are produced in the cooling water of the Swiss Spallation Neutron Source (SINQ) facility at Paul Scherrer Institut (PSI), Switzerland, by proton spallation reactions on ^{16}O [88]. An ion exchange filter was used to extract Beryllium, with other cations, from the cooling water. A second and more refined chemical separation was performed using the method described in [88, 89] to obtain chemically pure beryllium in a diluted HNO_3 solution.

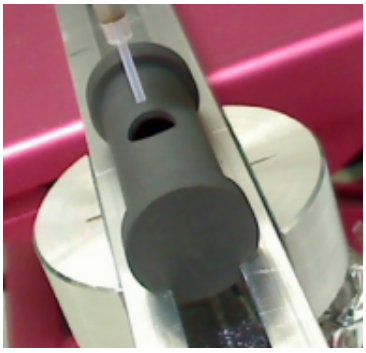

Figure 3.7: Photo of the cylindrical graphite crucible in which the beryllium solution is loaded. The crucible is part of the source used at ISOLDE.

Approximately 90 GBq of ^{7}Be were taken from the solution and loaded into a cylindrical graphite crucible, in a lead shielded manipulator box, and heated at 333 K until the solution became dry. The crucible is shown in Figure 3.7.

Afterwards, the crucible was transferred to another laboratory of PSI, where, using remotely controlled manipulators, it was inserted into an

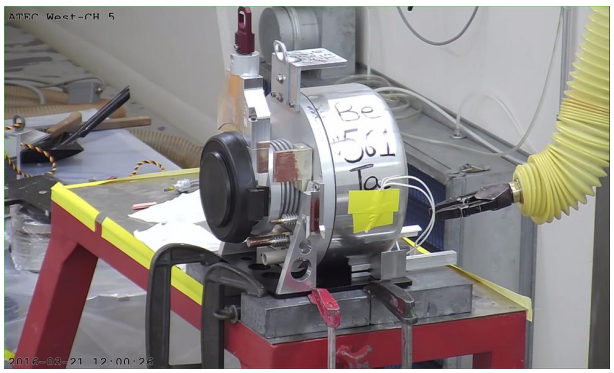

Figure 3.8: Empty tantalum container where, using remote controlled manipulators, the crucible was inserted.

empty tantalum target container (20 mm inner diameter and 200 mm length). After been loaded with the ^{7}Be sample, the Ta container was sealed with a Ta plug, the surrounding vacuum chamber was closed and the entire unit (shown in Figure 3.8) was then placed into a lead shielded transport container and transferred to the ISOLDE facility at CERN [90].

3.2.2 Implantation of ^{7}Be into aluminum foils

After the production and the chemical separation, the next step was the implantation of ^{7}Be into aluminum foils. To this purpose, the unit containing the ^{7}Be sample was placed on the front-end of the ISOLDE General Purpose Separator (GPS) at CERN.

The ionizer and target container were heated up to 1673 K for one day to get rid of surface ionized impurities (Li, Na, Al, K, Ca, etc.) present in the unit. The ionizer was then heated up to 2373 K, while the target container with the ^{7}Be sample was heated progressively from 1673 K to 1873 K. Beryllium was ionized by means of laser ionization. The first step transition (234.9 nm) was generated by third harmonic generation of a red dye laser beam and the second step transition by second harmonic generation of a yellow dye laser beam. The generated ions were accelerated to 30 keV and mass-separated with the GPS. The mass-7 ion beam was then implanted into an aluminum backing (1 in Figure 3.9) of 50 x 50 x 0.018 mm^3, placed between two aluminum frames (2 in Figure 3.9) of 50

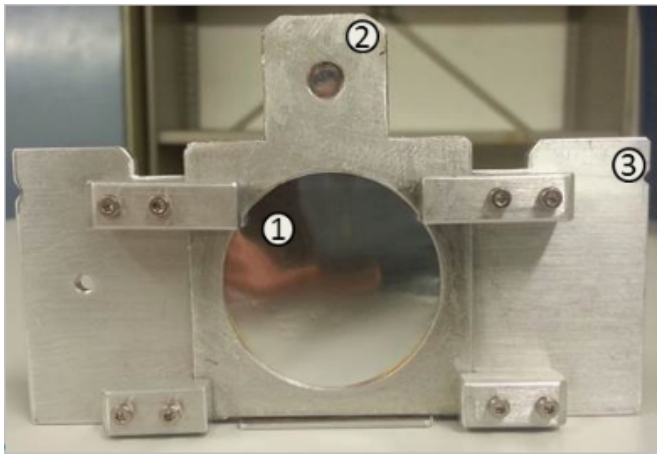

Figure 3.9: Target assembly for ^{7}Be implantation: (1) aluminum backings, (2) aluminum frame, (3) target holder.

x 50 x 1 mm^3 with a central hole of 40 mm diameter. Finally the target was placed in a target holder (3 in Figure 3.9) specifically designed to facilitate insertion and extraction of the radioactive sample.

In order to obtain a uniform target of ^{7}Be, a new tecnique, never performed before at ISOLDE, was tested with simulations. It consisted in moving the beam with two magnet deflectors, one horizontal and one vertical with equal amplitude and out of phase, in order to cover the desired surface uniformly.

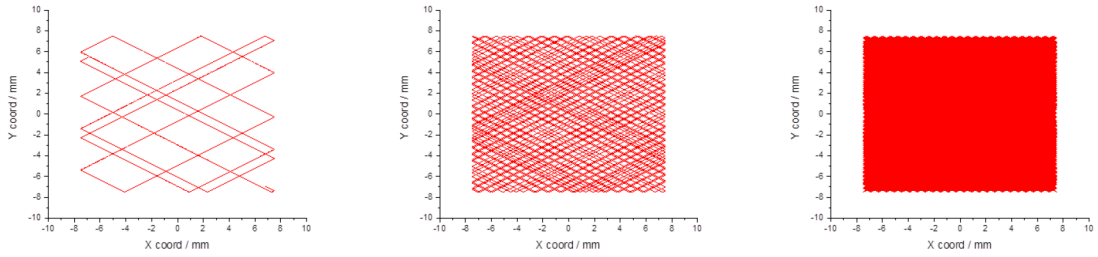

Figure 3.10: Results of the simulation of two magnet deflectors describing two different Lissajous curves in order to cover uniformly a surface of 1.5 cm^2 with ^{7}Be. The three panels are showing the covering of the surface at three different times [91].

Figure 3.10 shows the result of a simulation performed using a frequency of ω_x=241 Hz for the horizontal deflector and a frequency of

ω_y=150 Hz for the vertical one; the three panels show the covered surface at different times, t. The path done by the two deflectors is described by two Lissajous curves:

$$x = A_x f(\omega_x t + \Phi_x) \tag{3.2}$$

$$y = A_y f(\omega_y t + \Phi_y) \tag{3.3}$$

In the equations A_x and A_y are the amplitudes (in the simulations A_x=A_y), as already mentioned ω_x and ω_y are the frequencies and Φ_x and Φ_y the phases of the two deflectors. In order to cover a surface of 1.5 cm^2 uniformly, as shown in the last panel of Figure 3.10, 7.2 x 10^{15} ions, corresponding to an activity of about 1 GBq, were estimated to be implanted over 10 hours. Due to technical problems, this method was never performed and the final implantation of ^{7}Be into aluminum foils was made using a fixed ^{7}Be beam of $\sim$ 1 mm diameter.

Two ^{7}Be targets were produced at Isolde for the n_TOF measurement. The first one (Target_22MBq) contained 1.47 x 10^{14} atoms, corresponding to an activity of about 22 MBq. During the implantation, that lasted 10 hours, the ^{7}Be beam current was quite low, between 0.15 nA and 3 nA. The second ^{7}Be sample (Target_1GBq), also produced with a 10 hour implantation, had a much higher amount of material (7.2 x 10^{15} atoms, corresponding to an activity of about 1 GBq) thanks to a more efficient extraction from the source. In this case the beam intensity during the implantation was between 5 nA and 44 nA. The corresponding mass of Target_1GBq is $\sim$ 80 ng. It is worth to stress that the $^7Be(n,p)^7Li$ cross section measurement performed at n_TOF has been the first neutron measurement performed with a sample produced at a Radioactive Beam Facility (ISOLDE).

3.3. Characterization of the n_TOF ^{7}Be targets

The aim of the characterization of ^{7}Be was to identify the distribution of the target and the position of the implanted area with respect to the beam. After both Target_22MBq and Target_1GBq were used at n_TOF for the $^{7}Be(n,p)^{7}Li$ cross-section measurement, they were both sent to PSI where the total activity and distribution of the implanted ^{7}Be atoms were measured.

3.3.1 Activity measurement

The activity of Target_22MBq was measured by means of a coaxial HPGe-detector (crystal dimensions: 35 mm diameter and 52 mm length) providing an energy resolution of 1.77 keV at 1333 keV in combination with Canberra modules for high-voltage supply, spectroscopy amplification and a 100 MHz Wilkinson 8192 channel ADC. The distance between the sample and the detector endcap was 11 cm. The value of activity was derived via comparison with a certified standard reference point source ^{152}Eu placed at the same distance in front of the detector. The same system and method were used for the activity measurement of ^{7}Be Target_1GBq. In this case, due to the higher activity, the target was placed at 389 cm from the detector in order to keep the count rate at a reasonable level.

3.3.2 ^{7}Be distribution measurement

Since the new implantation technique of ^{7}Be into aluminum foils was not used at the end, the characterization of the ^{7}Be spatial distribution was an important and necessary step in order to understand the uniformity of the sample. The spatial distribution was measured with two different methods: radiographic imaging (RI) and semi-automatic γ-scanning (GS).

Radiographic imaging (RI)

The RI method was used to measure the spatial ^{7}Be distribution of both targets. A laser scanner, GE TyphoonTM FLA 7000, with spatial resolution of 25 μm was used in combination with reusable Fujifilm imaging plates. This is a two-dimensional radiation detector with a phosphor layer of photostimulable barium fluorobromide, usually doped with europium (BaFBr:Eu^{2+}) that traps the radiation energy. The stored energy is stable until scanned with a laser beam, that causes a release of the energy as luminescence.

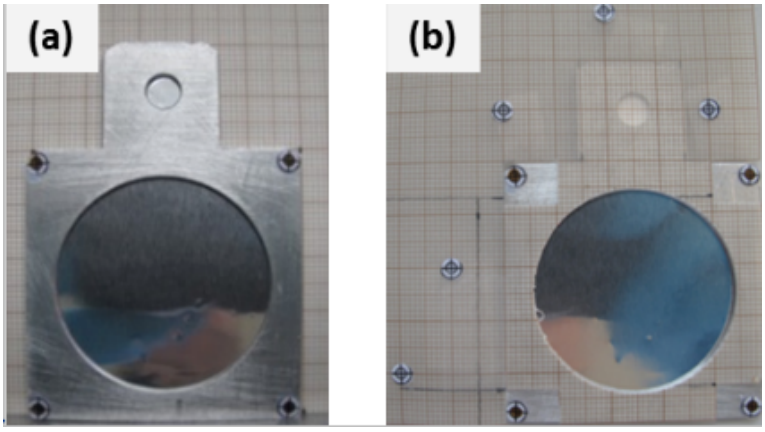

Figure 3.11: Panel (a): Target_1GBq consisting of an aluminum frame and an aluminum foil where ^{7}Be was implanted. Four spots of radioactive markers at the edges of the aluminum frame are used to establish an absolute coordinate system. Panel (b): Target_1GBq placed behind a millimetre graph paper. The holes in the millimetre graph paper at the corresponding positions of the radioactive parts prevent the attenuation of emitted β-particles.

The emitted light is collected and transformed into an electrical signal by a photomultiplier tube. The electrical signal is then converted from analog to digital information for image display and analysis. Figure 3.11, panel (a), shows a photograph of Target_1GBq that is representative also of Target_22MBq. Four point-like sources of about 50 Bq of ^{44}Ti were placed at the edges of the aluminum frame. Those markers were used to link the obtained relative coordinates of the image to the geometrical centre of the target. The target was placed on a millimeter graph paper with marks corresponding to the central hole of the aluminum frame and

to the four ^{44}Ti markers, as shown in Figure 3.11 (b). Five more ^{44}Ti markers were added onto the millimeter paper to improve the accuracy of the established absolute coordinates. The recorded 2-dimensional RI-data display the energy dose deposited locally by photons or charged particles (in our case only electrons). An image with a resolution of 0.25 x 0.25 mm^2 was obtained.

Semi-automatic γ-scanning

In order to investigate the high activity Target_1GBq, a new set-up was developed, based on a semi-automatic γ-scanning system. This system is suitable for investigating the activity distribution of highly radioactive samples (i.e. activities from few MBq up to several GBq). It was used to measure the ^{7}Be distribution of Target_1GBq three months after the ^{7}Be implantation, when its activity was about 0.3 GBq. In order to allow precise positioning ($\pm$0.01 mm) in front of a coaxial HPGe-detector, Target_1GBq was placed in a 3D positioning system. A 10 cm thick lead collimator with a 2 mm aperture hole was placed between the target and the HPGe-detector as shown in Figure 3.12. The distance between the target and the detector endcap was 32.4 cm.

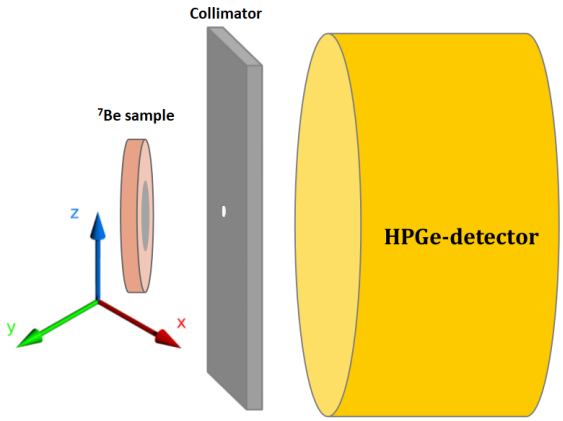

Figure 3.12: Schematic drawing of the γ-scanning system used for the ^{7}Be sample imaging. A 10 cm thick lead collimator with a 2 mm diameter hole is placed in front of a coaxial HPGe-detector.

The geometrical centre of the target was aligned with the 2 mm

aperture hole and with the centre of the detector using a laser pointer. The target was moved along the x and y directions in 2 mm steps. A total target area of 4 cm^2 was investigated, counting 121 points. In order to improve the spacial resolution, 12 additional measurements were made with 1 mm step size around the deduced centre of the activity distribution. The resulting ^{7}Be distribution was compared with the distribution obtained with the RI method, to validate the set-up and the accuracy of the results.

3.4. Results

The ^{7}Be activity of Target_22MBq was found to be 0.26 ± 0.04 MBq after one year from its implantation, corresponding to 21.6 ± 0.4 MBq on the date of its implantation (12 April 2016). The measured ^{7}Be activity of Target_1GBq was 0.46 ± 0.02 GBq two months after its implantation, corresponding to 1.03 ± 0.02 GBq on the date of its implantation (14 May 2016). Figure 3.13 (a) shows the Radiographic Image (RI) of the entire Target_1 GBq set-up including the ^{44}Ti markers.

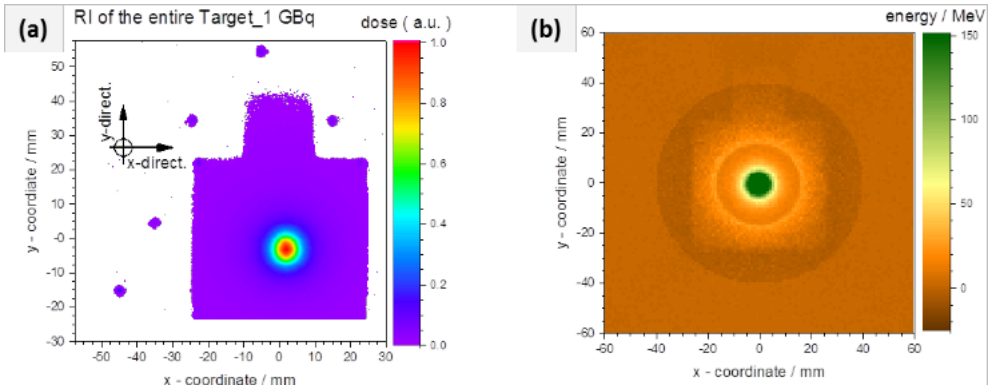

Figure 3.13: Panel (a): Two-dimensional Radiographic Image of Target_1GBq. Panel (b): GEANT4 simulation of the deposited energy in the Imaging Plate (IP) under exposure to 477 keV γ-rays [91].

The area with higher dose (bright coloured region) represents the direct projection of the implanted area due to the primary photons of 477.6 keV, emitted following ^{7}Be electron capture decay to the excited

state of ^{7}Li (branching ratio 10.44%). The photons scattered by both backing and frame impinging on the Imaging Plate, produce an image of the entire target (violet area in Figure 3.13 (a)). This image, together with the images of the ^{44}Ti markers, allows to have a perfect representation of the entire target geometry and, more importantly, to locate the implanted area with respect to the geometrical centre of the sample itself.
In order to verify the observed image of the sample backing, simulations were performed with GEANT4 [92]. The implanted ^{7}Be activity was simplified as an ideal point source located in the geometrical centre of the aluminum foil, at a depth of 100 nm below the surface. In total 1.5 billion γ-rays with an energy of 477 keV and an isotropic angular distribution were generated in the simulations. This number corresponds roughly to 240 minutes of exposure in the case of the autoradiography of Target_1GBq. The energy deposition caused by radiation in the sensitive layer of the Imaging Plate was recorded on a grid with a resolution of 1 mm x 1 mm. The results of the simulation can be seen on Figure 3.13 (b). The shape of the target frame highlighted by secondary radiation is clearly present in the simulated spatial dose distribution, reproducing the phenomena seen on the autoradiography image of the ^{7}Be targets.

The width and the positions of implanted ^{7}Be in both targets were extracted from the meaurements. The results indicate that the implanted area of both targets has a planar cross section of an ellipse, with the implanted area of Target_22MBq more elongated (its eccentricity is closer to one) than the one of Target_1GBq. Furthermore, the implanted area of Target_22MBq is shifted with respect to the geometrical centre of the target. A different location of the implanted area was found for Target_1GBq, showing a shift with respect to the geometrical centre of the respective target in opposite direction compared with Target_22MBq (further details are reported in Table 3.1).

Figure 3.14 shows the RI 2D autoradiography images of Target_22MBq and Target_1GBq, panel (a) and (b) respectively, both superimposed to the n_TOF neutron beam profile with the centre of the beam profile coinciding with the geometrical centre of the target.

Target	x-center [mm]	x-width [mm]	y-center [mm]	y-width [mm]	rotation [◦]
RI of Target_22 MBq	-4.978 ± 0.008	1.006 ± 0.006	-4.252 ± 0.012	1.263 ± 0.011	-0.14
RI of Target_1 GBq	-1.699 ± 0.183	2.064 ± 0.011	-5.200 ± 0.112	2.440 ± 0.012	-0.13
GS of Target_1 GBq	0.940 ± 0.002	1.861 ± 0.002	-1.880 ± 0.003	2.375 ± 0.003	0.23

Table 3.1: Position with respect to the geometrical center of the target and width of the deposit area of Target 22 MBq and Target 1 GBq [91].

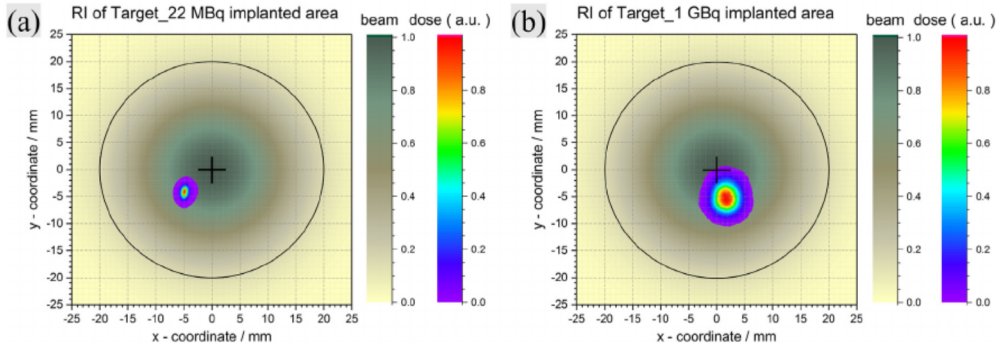

Figure 3.14: 2D spatial reconstruction of the distribution of the implanted ^{7}Be (right colour code) of the Target_22MBq and Target_1GBq, panel (a) and (b) respectively. Superimposed are the expected neutron field at EAR-2 (left colour code) and the geometrical centre of the target frame (black cross). All 2D distributions are normalized to the respective maximum [91].

It can be noticed that, due to the shift of the ^{7}Be deposit relative to the center of the target, the implanted area of Target_22MBq was exposed to the neutron beam in a region where its intensity is 60%-80% lower than the maximum, while for Target_1GBq the intensity was between 75% and 85%.

Finally Figure 3.15 presents the γ-scan obtained using the semi-automatic γ-scanning system described above for Target_1GBq. Comparing the distribution obtained with the Radiographic imaging and the semi-automatic γ-scanning (see Table 3.1), allowed to identify the position of the implanted area with an error smaller than the resolution of each set up, i.e. 2 mm.

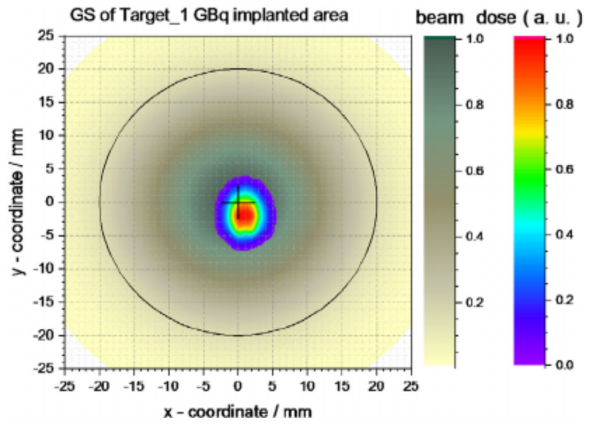

Figure 3.15: γ-scanning image of Target_1GBq. The data were scaled to a resolution of 0.25 mm 0.25 mm using the Kriging algorithm [93, 94].

In conclusion for the first time, thanks to a well-established collaboration between PSI and CERN (ISOLDE and n_TOF), two high activity samples of ^{7}Be were successfully produced by implantation of a ^{7}Be beam from ISOLDE. These samples were then succesfully used in the measurement of the $^7Be(n,p)^7Li$ cross section in the energy range of interest for the BBN at EAR2 of n_TOF.

3.5. Alignment and insertion of the target in the beam

In order to identify the position of the beam, two gafchromics foils (Gafchromic no 1 and Gafchromic no 2), based on the thermoluminescence principle, were installed at a height of $\sim$ 93 cm and $\sim$ 123.5 cm.

The measurement setup is schematically shown in Figure 3.16. The irradiation lasted for 10 hours, and an Al foil was placed in front of both gafchromic foils in order to accelerate the process of beam impression, (that results from charged particles produced by neutron interaction with Al). In order to have an external reference for the beam position, 6 lasers (L_1-L_6) were installed in the area and impressed on the same gafcromic foils, covering the two different heights.

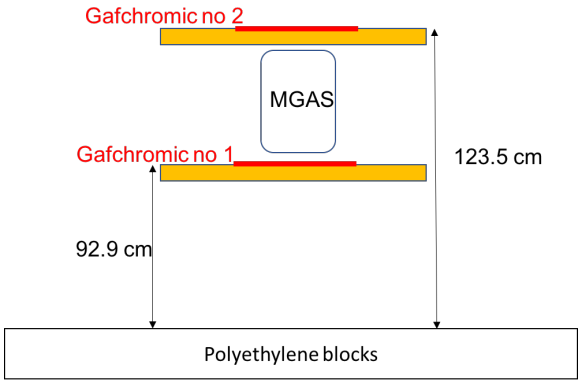

Figure 3.16: Position of the two gafchromics used for the beam position measurements in EAR2

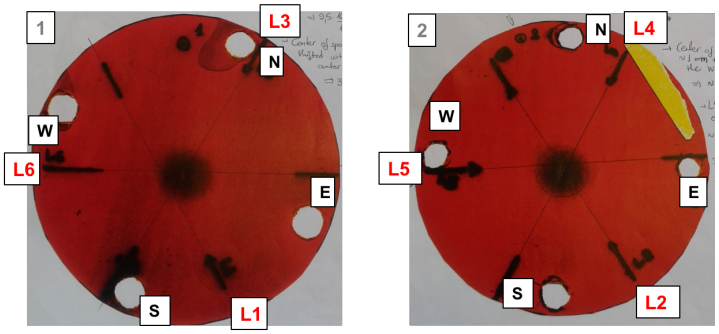

Figure 3.17: The processed images of the two gafchromics foils. The laser labels (red) are noted at the side from which the laser comes. The wall labels (black) are also noted (North, South, East, West).

In particular, as it can be seen in Figure 3.17, lasers L_1, L_3 and L_6 produced a mark on gafcromic 1, while L_2, L_4 and L_5 on gafcromic 2. The photo in Figure 3.17 clearly shows the image of the neutron beam in the center of the gafchromic foil, together with the marks produced by the laser beams. This procedure allows one to determine the position of the beam with respect to the lasers, which can then be used as reference for the allignment of the experimental setup used for the $^7Be(n,p)^7Li$ measurement. This procedure allowed to align the geometrical center of both the ^{6}Li and ^{7}Be samples (more precisely the center of the sample backings) to $\pm$ 1 mm relative to the beam center position. Therefore, the

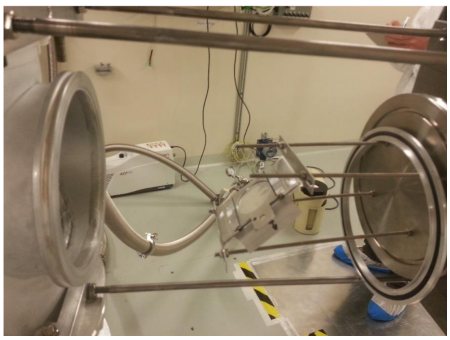
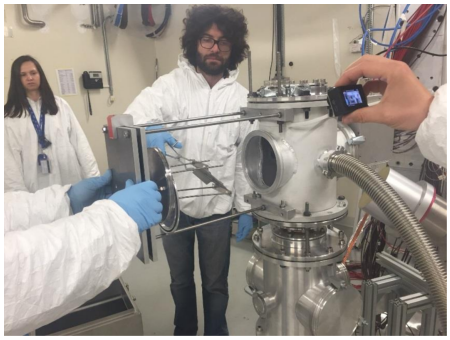

Figure 3.18: Insertion of the ^{7}Be sample in the aluminum vacuum chamber.

maximum possible displacement between the two samples was ± 2 mm. This value can be considered as the uncertainty related to the centering of the two samples with respect to the beam position.

Once the set-up was aligned, the ^{7}Be target assembly, was put in beam. The operation was done in the shortest possible time, in order to minimize the absorbed radiation dose: the final collected dose was less than 10 μSv. Figure 3.18 shows the ^{7}Be target assembly insertion in the aluminum vacuum chamber, the last operation before the starting of the $^7Be(n,p)^7Li$ cross section measurement.

Chapter 4

Data Analysis and Simulations

4.1. Pulse Shape Analysis routine

In order to determine the amplitude and the position in time of every recorded signal, an offline pulse shape analysis routine was used to analyze the raw data [95]. The pulse shape analysis framework was developed as a general purpose tool and it can be applied to all detectors used at n_TOF. The routine can be adapted to a specific detector by adjusting a set of external input parameters.

In order to identify a pulse (or signal) in the recorded waveform, the standard pulse shape analysis is used. Briefly, a pulse in recognized when the derivative of the waveform crosses a given threshold. In order to reduce noise fluctuations that could be mistakenly identified as signals, an integration of the waveform over a given time is performed before taking the derivative according to the following formula:

$$\sigma_i(N) = \sum_{k=1}^{N} s_{i+k} - \sum_{k=1}^{N} s_{i-k} \tag{4.1}$$

Here, s represents the original waveform, while σ_i(N) is the derivative of waveform integrated over a step-size N, essentially representing the

time (in nanoseconds). The optimal value of the step-size is determined manually so to achieve the best signal-to-noise ratio in the calculated derivative. A small value of N may not filter the noise completely, while an excessive increase of the step-size would prevent the separation of two pulses when they are too close in time. Figure 4.1 shows that if a pile-up of signals is not recognized at first, using an appropriate choice of the step-size the routine is able to recognize the two different pulses instead of one. A similar argument applies to the choice of the threshold used for signal recognition which has to be set as low as possible to avoid loss of good events, but high enough to reject most of the electronic noise that could be recognized as a real signal.

Before applying the procedure described above, in order to speed-up the pulse shape analysis, a threshold on the amplitude is applied so to avoid processing fluctuations in the waveform related to the electronic noise. This is a preliminary step, where a minimum threshold is used to reject most of the electronic noise.

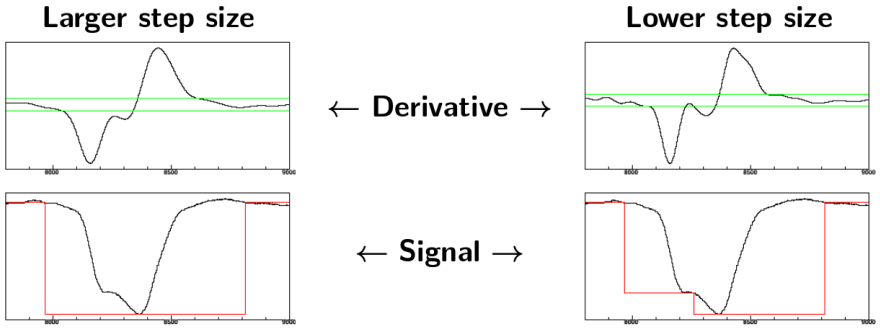

Figure 4.1: Effect of the step size parameter in the discrimination of two pulses when a pile-up occurs. The left side shows the case of a too large step size: the two signals are recognized as a single one with a width equal to that of the red window. The right side shows a correct recognition of the two signals.

In a neutron bunch, the first pulse detected is the so called γ-flash signal (mentioned in the second Chapter). It is very important to correctly identify such a pulse in order to obtain a correct time-to energy conversion. An example of γ-flash signal is visible in Figure 4.2, top panel. The γ-flash

is marked with a yellow line and is recognized as the first signal satisfying a certain set of conditions [96]. It may be recognized as the first pulse crossing a given threshold or the first "saturated" signal, i.e. with a flat top (its amplitude is larger than the maximum conversion range of the FADC). In some cases, the Silicon Telescope suffered from the occurrence of false γ-flash, such as signals able to cross the selected threshold. For these cases a threshold in the γ-flash width was used and this was enough to discriminate the real γ-flash from the false ones.

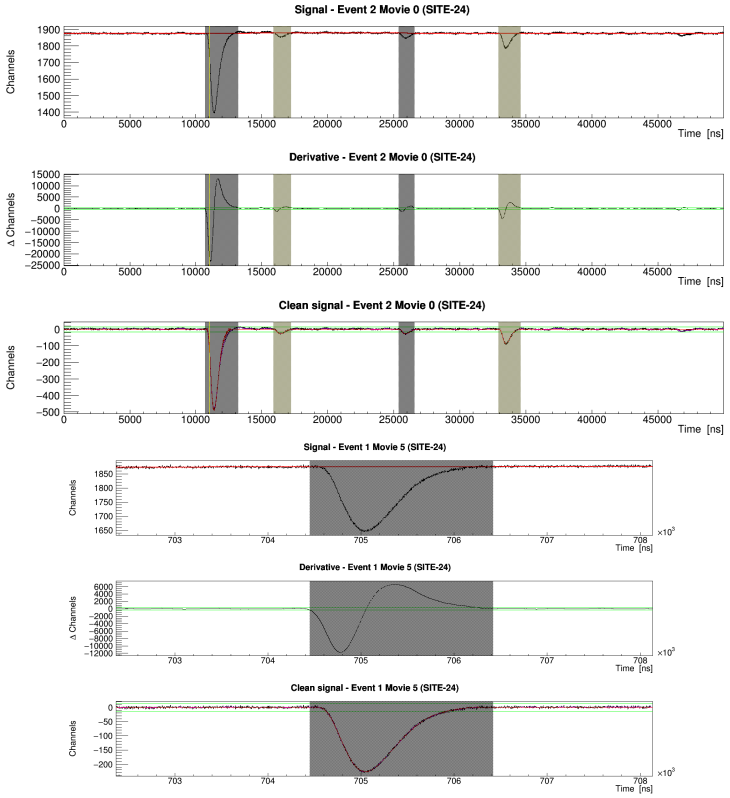

Figure 4.2: On the top the γ-Flash pulse of strip 24 in the E detector. On the bottom an example of proton pulse in the same strip.

The bottom panel of figure 4.2 shows an example of one of the signals recorded in one of the 16 strips of the E detector. As previously mentioned, in order to recognize the presence of the signals in the recorded waveform, a given threshold in the amplitude has to be crossed. Such a threshold

needs to be chosen so to reject most of the noise, but not to discard the smallest signals. In order to reject the noise accidentally crossing the threshold, further conditions can be applied in the shape analysis routine by means of external input parameters. These conditions include the threshold on the derivative discussed before, a lower and upper limit for the signal width, as well as a lower and upper limit for the area-to-amplitude ratio. The first condition, based only on the signal width, is applied immediately after the signal recognition procedure. The final discrimination, based on the signal amplitudes and areas, may only be performed at a later stage, after the baseline has been calculated. The baseline is treated differently below and above a given "time limit", set by the user. It defines the range where the effect of the γ-flash, such as baseline oscillation or undershot, is still present and an adaptive baseline calculation is needed (based on a weighted waveform averaging). Above the time limit, a constant baseline is calculated.
To find the amplitude of the signal, several options are available: one can search for the highest level of the pulse or can activate a predefined Pulse Shape fitting. In the latter case, a standard shape for the signals needs to be provided and both the final amplitude and area will be determined from the fitted pulse. For the Silicon Telescope the chosen option was to activate the parabolic fitting to the top of the pulse and, in this case, the area under the pulse is calculated by simple pulse integration.
For both protons and γ-flash, figure 4.2 shows the selection of the recorded signals in the top panel, while the central panel shows its derivative. Finally the bottom panel shows the result of the pulse reconstruction procedure. From the reconstructed signal, the relevant parameters were extracted: time of flight, amplitude, area, baseline, etc.

4.2. The reference reaction ^{6}Li(n,t)^{4}He

Once the amplitude and the time of every recorded signal were determined, a calibration of the setup was performed in order to determine the energy

released by the particles in the detectors. For the calibration, the following reaction was used:

$$^{6}Li + n \Rightarrow (2.73MeV)\, t + (2.05MeV)\, \alpha \tag{4.2}$$

Apart from the energy calibration, this reaction is used as a reference for the cross section determination. In fact, this is a "standard" reaction, i.e. characterized by a cross section known with an accuracy of less than or around 1% [73]. For this measurement, a LiF sample of mass 1.1 mg, produced by evaporating a 1.8 μm thick ^{6}LiF layer onto a 2μm thick mylar foil was used [97]. The size of this sample was 5cm x 5cm, but a 1.5cm x 1.5cm aluminum mask was used during the measurement to "simulate" an effective target area consistent with the planned area of the ^{7}Be sample.

4.2.1 Energy calibration

Once the neutrons interact with the LiF sample, tritons and alpha-particles of 2.73 MeV and 2.05 MeV respectively are produced. While the alphas

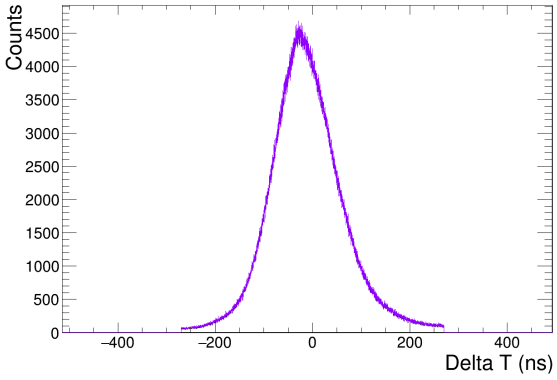

Figure 4.3: Time difference spectra between signals in the ΔE and E detector.

are stopped in the ΔE detector, the tritons cross it releasing ∼ 1 MeV energy and then they are completely stopped in the E detector where they deposit the remaining energy of ∼ 1.7 MeV.
In order to calibrate the set-up, the particles have first to be selected by

the coincidence between the ΔE and E detector. The coincidence time window chosen was 260 ns. This value was decided by looking at the time difference (ΔT) between signals in the E and in the ΔE detector shown in Figure 4.3. This choice includes all coincidences and rejects most of the background. Since the α particles are stopped in the ΔE detector, the coincidence identifies just tritons. For this reason, the α particles are not included in the analysis. To understand the correlation between

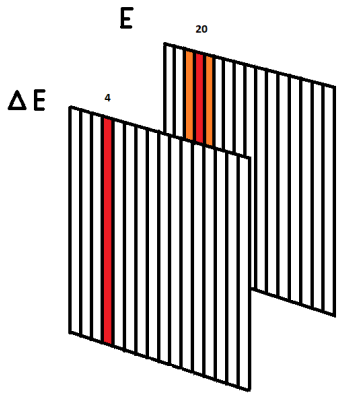

Figure 4.4: Sketch of the method used to evaluate the coincidences strip by strip. As an example for the strip n 4 in the ΔE detector, coincidences with the strips number 19, 20 and 21 in the E detector are considered.

the strips, simulations were performed with GEANT4. The number of coincidences in each strip of the ΔE detector was counted as a function of the stips chosen in the E detector. Simulations indicated that the best coincidence selection is obtained by putting in correlation each ΔE strip with three strips in the E detector as shown in Figure 4.4, i.e. the strip directly behind the ΔE strip and the two adiacent ones. Figure 4.5 shows the ΔE vs E plot obtained from the simulations with the strip correlation choice described above: each plot shows the coincidence between each ΔE strip with the strip directly behind and the two adiacent ones in the E. The tritons spot is clearly visible in all the plots except in the last one

where the coincidences between the last strip in the ΔE (strip 16) and the corresponding last two strips in the E (strip 31 and 32) are reported. This lack of coincidences is due to the fact that the proton trajectory at that angle (above 90 degrees relative to the beam direction) crosses the edge of the ΔE detector, but goes outside the edge of the E detector. The ΔE vs E plot obtained with the data confirms the same finding (see Figure 4.6).

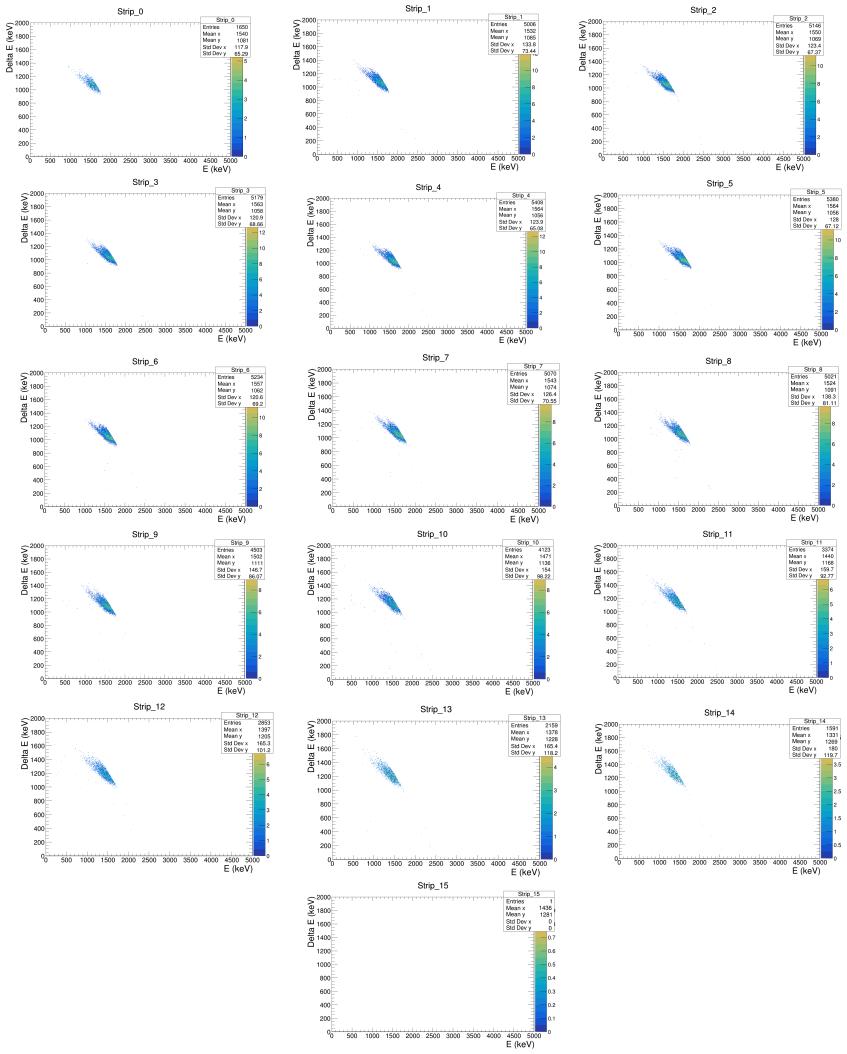

Figure 4.5: Simulated two-dimentional E-ΔE plots recorded with a ^{6}Li target, for each strip in the ΔE detector, in coincidence with the three corresponding strips in the E detector.

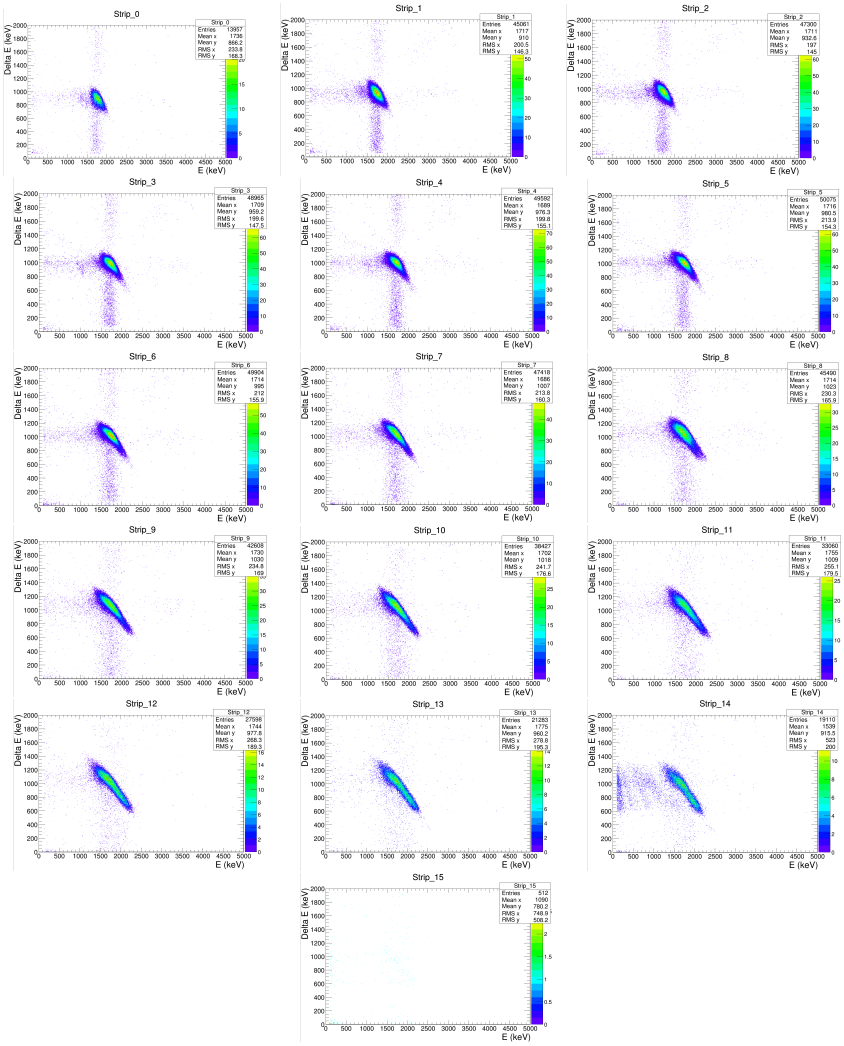

Figure 4.6: Same as Figure 4.5 for the real data.

Figure 4.7, left panel, shows the amplitude spectra for tritons in FADC channels. Since the kinetic energy of the tritons emitted from the $^6Li(n,t)^4He$ reaction is well known and equal to 2.73 MeV, the setup was calibrated by associating this value to the peak in the amplitude spectra. Figure 4.7, right panel, shows the corresponding calibrated energy deposited spectrum.

Another important step in the analysis is the background rejection. Figure 4.8, left panel, shows a 2D ΔE vs E plot obtained from the interaction of

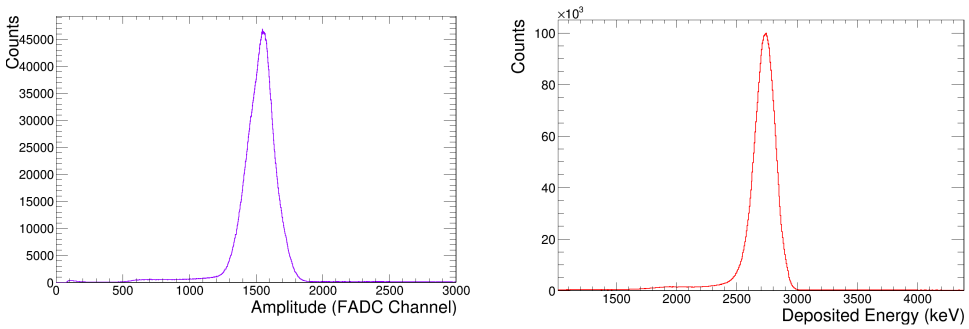

Figure 4.7: On the left the amplitude spectra of the tritons from the n+^{6}Li interaction. On the right the Energy deposited spectra of the tritons summing the ΔE and E calibrated signals.

neutrons with the LiF sample deposited onto a 2μm thick mylar foil and surrounded by the aluminum mask. In the plot one can clearly see the region corresponding to tritons, together with some background.

In order to better identify the background, data were taken with a "dummy" sample in the beam, i.e. a mylar backing and the aluminum mask but without the LiF deposit. The corresponding 2D ΔE vs E plot in the right panel of Figure 4.8, shows the background events, mainly concentrated at low amplitude and presumably mostly related to random coincidences between electronic noise. As expected, the centroid in the 2D distribution for the ^{6}LiF sample corresponds to the nominal values of the energy that the tritons deposit in the ΔE and in the E detector, i.e. $\sim$ 1 MeV and $\sim$ 1.7 MeV respectively. However, one can notice that even if the triton pattern is clearly visible, it is widely spread in both directions. This is due to a variation in the energy loss in the target, depending on the emission depth and angle, and to the spread of incidence angles on the detector. Apart from the central peak, one can notice vertical and horizontal bands as well as the counts in the low ΔE-E region. The vertical and horizontal bands above the triton peak are due to pile-up events, while the bands below the peak are most probably related to particles crossing only part of the strips and thus releasing a fraction of the energy. Finally, the counts in the low ΔE-E region are caused by random coincidences of electronic noise discussed above.

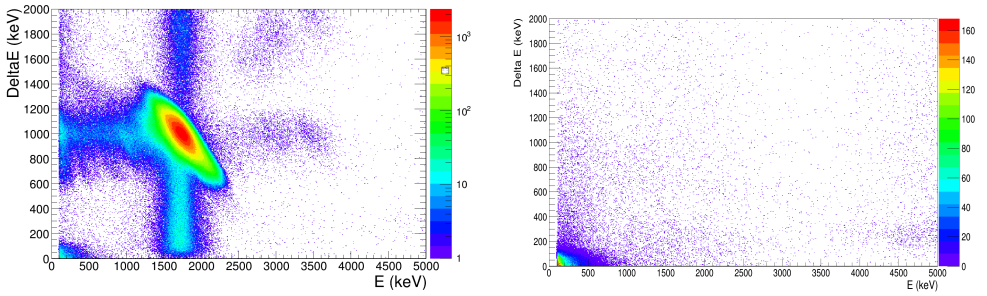

Figure 4.8: On the left the 2D ΔE vs E plot of the deposited energy of the tritons in coincidence. On the right the ΔE vs E scatter plot obtained from the interaction of the neutron beam with 25μm Kapton foil and the aluminum mask.

4.2.2 Efficiency

In order to extract the cross section, it is essential to determine the efficiency of the set up. As a first step, the relative detection efficiency for the tritons produced in the $^6Li(n,t)$ reaction as a function of the strip position was evaluated. For this purpose, a ΔE vs E plot was produced for each strip, applying to the data the coincidence technique explained in the previous section: the coincidence is studied between each ΔE strip and the closest three E strips. The relative efficiency of each strip was extracted by selecting the events falling within the triton peak in the corresponding ΔE vs E plot and dividing them for the total number of coincidences in all the strips. The results have been obtained for thermal neutrons, i.e. selecting neutrons with energy between 0.015-0.035 eV.

The relative detection efficiency of the setup was also determined from simulations applying the same evaluating method, considering, also in this case, just the thermal neutrons and using the same coincidence tecnique applied for the selection of tritons in the real data. The simulations have been performed with the Monte Carlo code GEANT4, generating a beam of neutrons impinging on a ^{6}LiF sample; the selected physics lists were FTFP_INCLXX_HP and emstandard_opt0 as already used in previous works on the n_TOF neutron flux [98] and neutron detection [99]. The simulated neutron beam profile was Gaussian with a σ of 1 cm and a radius of 2 cm (the radius defines the region in which the beam is

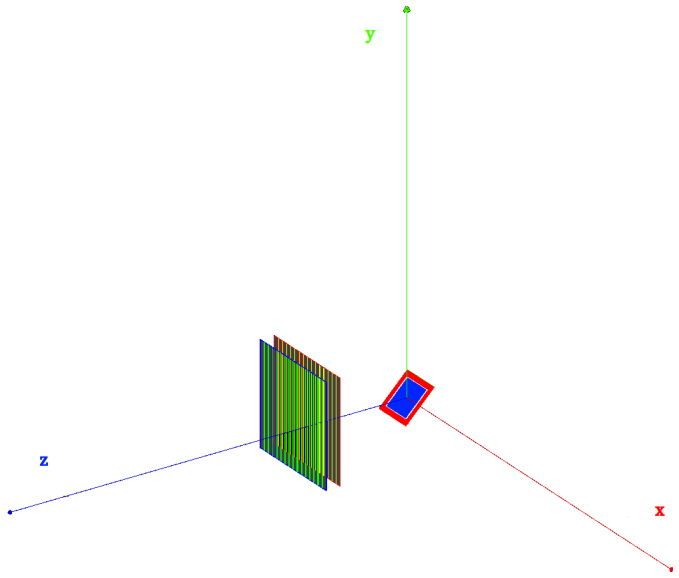

Figure 4.9: Simulated set up by means of the Monte Carlo code GEANT4

confined). A total of 10^8 neutrons were generated along the y axis (90 degrees with respect to the xz plane) at -2 μm distance from the center of the target whose thickness was 1.8 μm. A sketch of the simulated setup is shown in Fig. 4.9 where in blue the target of LiF is shown, tilted by 45 degrees and surrounded by the Aluminum mask in red, while the silicon telescope is on the left.

The plot in Figure 4.10 shows the relative detection efficiency for the tritons produced in the $^6Li(n,t)$ reaction as a function of the strip number, compared with the GEANT4 simulation. The slight difference between data and simulation in Figure 4.10 indicates a small misalignment of the detector relative to the target center. In fact, it can be noticed that the maximum number of counts is not at the 8^{th} strip as it should be if the telescope would have been centered with respect to the target, but it is shifted to the 6^{th} strip. Modifying the GEANT4 simulated set up in order to obtain the maximum rate at the 6^{th} strip, the mismatch between the target and the Silicon Telescope position has been identified, indicating that the telescope was shifted, relative to the center of the sample, by 10

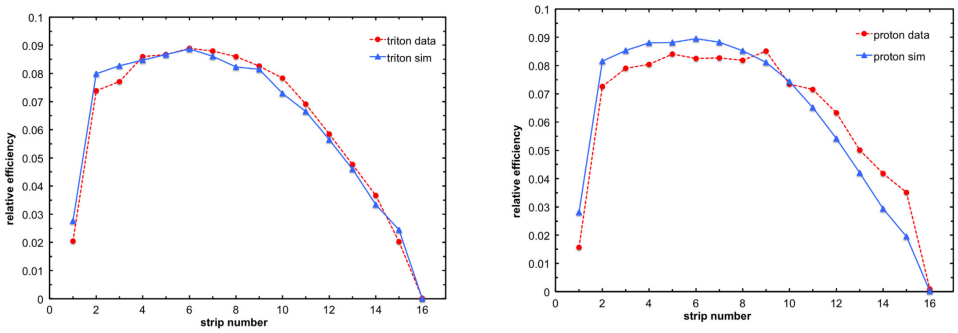

Figure 4.10: Left panel: detection efficiency of the setup normalized to unity area, as a function of strip number, obtained in the GEANT4 simulation (isotropic emission was assumed) and with ^{6}LiF target (triton detection in the validation test). Right panel: detection efficiency of the setup normalized to unity area, as a function of strip number, obtained in the GEANT4 simulation (isotropic emission was assumed) and with ^{7}Be target (proton detection).

mm to the right and 3 mm up.

GEANT4 simulations were also used to evaluate the total detection efficiency as a function of the incident neutrons energy. In this case the efficiency has been determined by taking a ratio between the coincidences of tritons detected in all the strips and the number of tritons produced in the interaction of the neutrons with the LiF sample. Every time a triton was produced in the simulation, its history was recorded on a file. Afterwards, the simulated triton was analyzed by means of the same coincidence technique used for the selection of tritons in the real data. Simulations were performed with monoenergetic neutron beams of 26 different energies, with 10^8 neutrons impinging on the sample for each run. Since the cross section of the $^{6}Li(n,\alpha)^{3}H$ reaction, as shown in the next section, has a 1/v (v being the neutron velocity) trend, the detected number of tritons decreases as the neutron energy increases. For this reason as the energy of simulated neutrons increases, more runs have been performed in order to produce statistically significant results. Despite the large number of iterations, as it can be seen from Figure 4.11, statistical fluctuations were still present. In order to avoid them, a parameterization of the efficiency was obtained by means of a fitting procedure. The curve in Figure 4.11 shows the results of such a procedure. The efficiency is

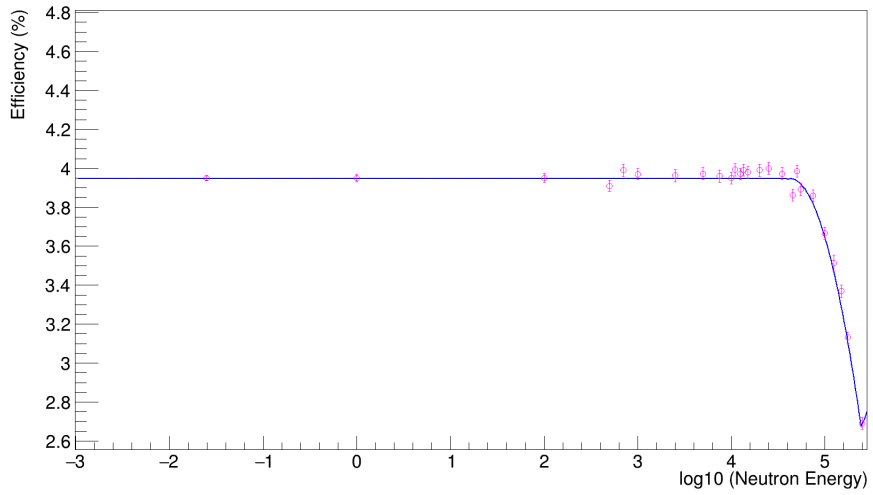

Figure 4.11: The pink dots represent the efficiency for the detection of tritons from the ^{6}Li(n,t) reaction, simulated by means of the Monte Carlo code GEANT4. The blue curve represent the fit of the simulated efficiency.

flat up to a few tens of keV, but it starts to decrease above this energy. This is related to the angular distribution of the tritons emitted in the reaction. In fact, the emission is isotropic up to 40 keV, after this value the emission presents a forward-backward angular anysotropy that affects the detection efficiency. In particular, the angular distribution of emitted tritons becomes forward focused at higher energies, and so the efficiency for detecting them around 90 degrees, where the telescope is mounted, decreases. Further details regarding the simulations are reported in Table 4.1, where the energy of the neutron beam, the number of tritons produced in the target, the efficiency averaged over the number of runs and the statistical errors are listed.

Neutron beam energy (eV)	Iterations	Tritons	Average efficiency (%)	Statistical error
0.025	1	2500	3.95	0.01
1	2	1813	3.95	0.02
100	2	1567	3.95	0.023
500	3	1213	3.91	0.028
700	3	1033	3.99	0.031
1000	4	1209	3.97	0.029
2500	6	1048	3.96	0.031
5000	8	1025	3.97	0.031
7500	10	1028	3.96	0.031
10000	13	1035	3.95	0.031
11000	12	1005	3.99	0.032
12500	17	1268	3.97	0.028
13500	13	1076	3.99	0.030
15000	14	1032	3.98	0.031
20000	18	1049	3.99	0.031
25000	18	1023	4.	0.031
35000	20	1044	3.97	0.031
45000	23	1053	3.86	0.031
50000	23	1031	3.98	0.031
55000	23	1100	3.89	0.033
75000	26	1091	3.86	0.031
100000	26	1012	3.66	0.032
125000	27	1003	3.51	0.041
150000	22	1008	3.37	0.032
175000	19	1149	3.13	0.030
250000	9	1015	2.69	0.031

Table 4.1: Results of Geant4 simulations, in particular the energies of the neutron beam, the number of tritons produced in the target, the efficiency averaged on the number of iterations and the statistic errors are here reported.

4.2.3 The ^{6}Li(n,t)^{4}He cross section

The $^{6}Li(n,t)^{4}He$ reaction represents a very reliable absolute reference to normalize the $^{7}Be(n,p)^{7}Li$ data, as the cross-section is standard from thermal up to 1 MeV neutron energy. Therefore, in order to verify the reliability of the analysis procedure, the $^{6}Li(n,t)^{4}He$ cross-section was reconstructed from the n_TOF data according to the following equation:

$$\sigma_{n,t}(E_n) = \frac{C_t(E_n) - B_t(E_n)}{\epsilon(E_n) \cdot \Phi(E_n) \cdot n_{LiF} * f_C} \tag{4.3}$$

Here C_t represents the counts of tritons per nominal neutron bunch (obtained by dividing the total counts by the total number of protons and multiplying by 7×10^{12} the number of protons in a nominal bunch), B_t the background events per neutron bunch, ϵ is the detection efficiency of the set-up (Figure 4.11), n_{LiF} is the total number of atoms of the LiF sample and f_C is a factor that represents the convolution of the normalized neutron beam spatial profile with the target nuclei distribution (described in the next section). $\Phi(E_n)$ is the total number of neutrons per bunch

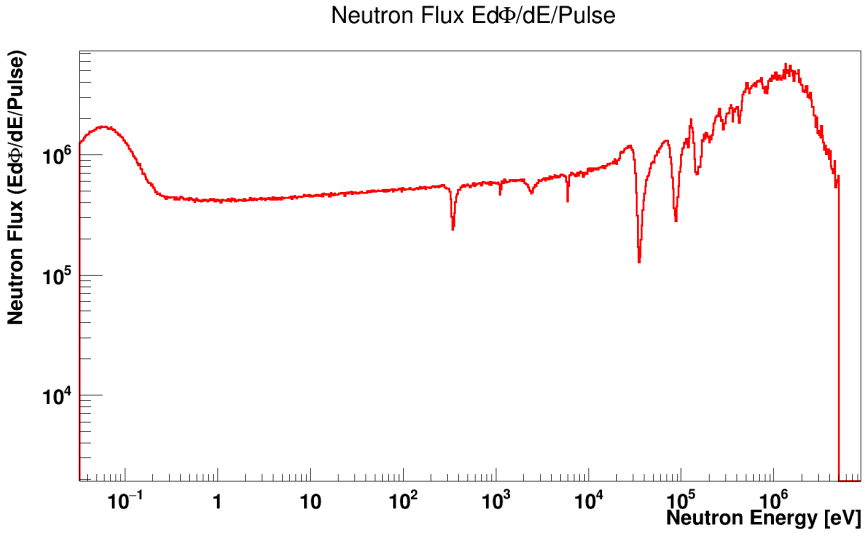

Figure 4.12: Evaluated neutron flux in EAR2, used in the present analysis.

at a given energy E_n in EAR2 (Fig. 4.12). As shown in Chapter 2, this has been determined using a set of independent measurements based on

different reference reactions and employing different detector technologies [48]. The obtained $^6Li(n,t)^4He$ cross section agrees with the standard one within 5%, in the whole neutron energy range from thermal to 1 MeV. This is a consistency check of the method and gives an idea of the accuracy of the estimated values for the efficiency and beam-sample convolution factor f_C, specifically calculated for the LiF sample. The

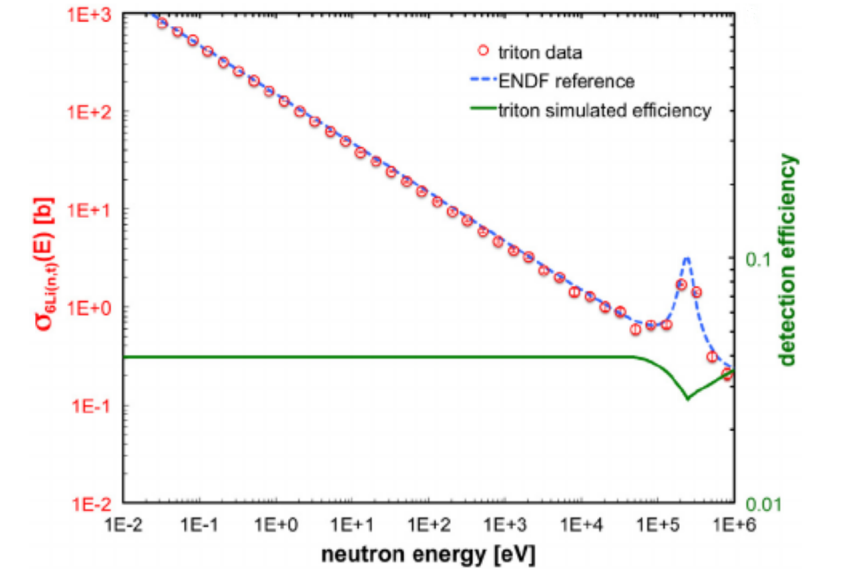

Figure 4.13: The measured $^6Li(n,t)^4He$ cross section (circles), compared with the international standard (dashed blue line). The good agreement allows the use of this reaction for normalization. The green continuous line, to be read on the right-hand axis, represents the triton detection efficiency as simulated by means of GEANT4.

good agreement between the measured cross-section and the standard one [100] is shown in Fig. 4.13, where the dip in the detection efficiency corresponds to the well-known resonance in the $^6Li(n,t)^4He$ cross-section which has a mostly p-wave forward-backward angular distribution [74].

4.3. The f_C factor

As previously mentioned, the factor f_C represents the convolution of the normalized neutron beam spatial profile with the target nuclei distribution

and has a dimension of cm^2 (or b^{-1}). In order to calculate this factor, used to account for potential target inhomogeneities (as in the case of ^{7}Be), one has to determine the spatial profile of the neutron beam and the spatial distribution of the deposit in the target. As discussed in the two previous chapters of this thesis, the deposit distribution was measured for both target used in the measurements (the ^{6}LiF and the ^{7}Be) [91], while the neutron beam profile was obtained from GEANT4 simulations of the spallation process and subsequent transport through the vertical beam line [81]. As will be better explained in the next section, the $^7Be(n,p)$ cross section is extracted relative to that of $^6Li(n,t)$. To this end, it is important to calculate f_C for both samples. This factor was estimated in two different ways: i) by analytical convolution of a gaussian distribution representing the neutron beam and a flat distribution of 1.5 x 1.5 cm^2 representing the ^{6}LiF sample, as well as a gaussian distribution representing the ^{7}Be deposit; ii) by means of simple Monte Carlo simulations considering the real distributions for the neutron beam and the samples. The ratio of the f_C factors calculated for the two samples (the only value that enters in the cross section determination), $R_f = f_C(Be)/f_C(Li)$, is practically the same using the two methods and in both cases is very close to unity. For both methods of calculation, the difference between the factors f_C for the two samples is around 2%, a value that is indicative of the uncertainty associated with the determination of the convolution factor.
However, there is an additional source of uncertainty that has to be considered for f_C, which is related to the centering of the two samples on the beam. In the measurement, the geometrical center of both the ^{6}LiF and ^{7}Be samples (more precisely the center of the sample backings) were aligned to $\pm$ 1 mm relative to the beam center position, identified by means of gafchromic foils, as discussed in the previous chapter. Therefore, the maximum possible displacement between the two samples was $\pm$ 2 mm.

In the Monte Carlo simulation approach, one can vary the relative position between the centers of the samples according to a Gaussian distribution with $\sigma = 2$ mm. Note that, as already mentioned in Chapter

3, the center of the ^{7}Be deposit is shifted relative to the center of the sample backing, but clearly this displacement is always taken into account in the simulations. The resulting distribution of R_f is approximately Gaussian, with average close to 1, as already mentioned, and with a standard deviation of 8%.

4.4. The ^{7}Be(n,p)^{7}Li reaction

As for the $^6Li(n,t)^4He$ reaction, in order to obtain the $^7Be(n,p)^7Li$ cross section, the first step in the analysis was to identify and select protons emitted following the interaction of neutrons with the ^{7}Be sample in the E-ΔE telescope. The coincidence window chosen is the same, 270 ns, and the method used to select the coincidences strip by strip is the one already described in section 4.2.1.

In order to select the protons and exclude the background, a 2D ΔE vs E plot, shown in Figure 4.14, was produced. The pattern of the

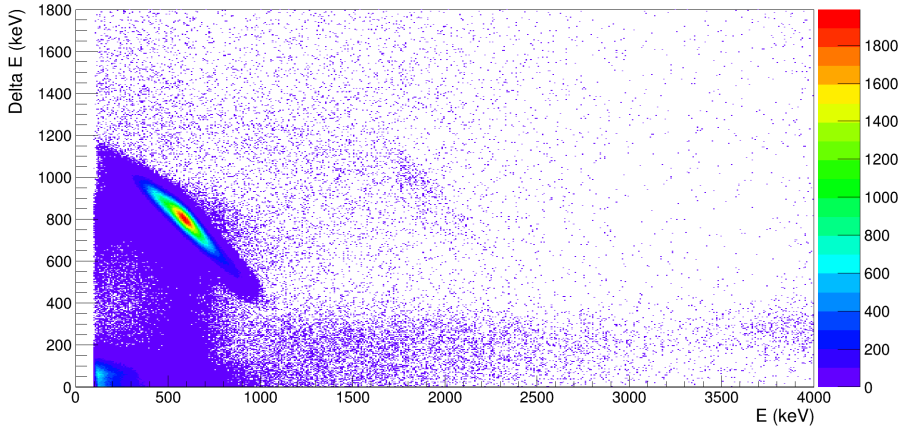

Figure 4.14: ΔE vs E scatter plot measured for the $^7Be(n,p)^7Li$ reaction, with the proton locus clearly visible.

coincidences is clearly visible. The protons release $\sim$ 800 keV in the ΔE detector and are stopped in the E layer, where they deposit $\sim$ 600 keV. Furthermore the proton region is well separated from the background. Considering the sample activity, it is mandatory to study the probability

of random coincidences produced by different γ-rays in the telescope. Although such a coincidence is possible, its probability is very low: in fact to be identified as a proton, the two γ-rays must deposit $\sim$ 800 keV in the ΔE and $\sim$ 600 keV in the E detector. It should be considered that the γ-ray has $\sim$ 500 keV of energy and, on top of this, when it interacts with the strip of the Silicon Telescope releases a small energy. This means that in order to produce a signal corresponding to $\sim$ 800 keV or $\sim$ 600 keV energy deposition, a pile-up in the same strip of two or more γ-rays is necessary. Finally, as already mentioned, in addition to the pile-up in the strips, a coincidence between the ΔE and E detector within the chosen time window of 270 ns is also needed.
Since in only 10% of cases the electronic capture produces an excited ^{7}Li that emits a γ-ray to de-excite, 1 GBq of total activity of the ^{7}Be sample used in the measurement, corresponds to 100 MBq of γ-ray activity. Considering the low geometric efficiency of $\sim$ 5%, the low interaction probability of a γ-ray ($\sim$1%) and the low energy deposited by the electrons produced by Compton or Photo-electric effect, the probability of pile-up and random coincidences between E and ΔE strips is extremely low, practically negligible.

4.4.1 Study of the background

As previously mentioned, the high purity of the sample, the use of a telescope for particle identification and the very high instantaneous neutron flux of EAR2 resulted in a practically negligible background associated with the natural γ-ray activity of ^{7}Be. The only source of background affecting the measurement is related to the $^{14}N(n,p)$ reactions in the sample backing on which the ^{7}Be was implanted. In order to identify such a background, a measurement was performed with an empty backing, i.e. without a ^{7}Be deposit, inserted in the beam. Figure 4.15 shows a comparison between the counts of protons coming from the interaction of the neutrons with the ^{7}Be sample (red curve) and the counts coming just from the interaction of the neutron beam with the empty backing (black

curve).

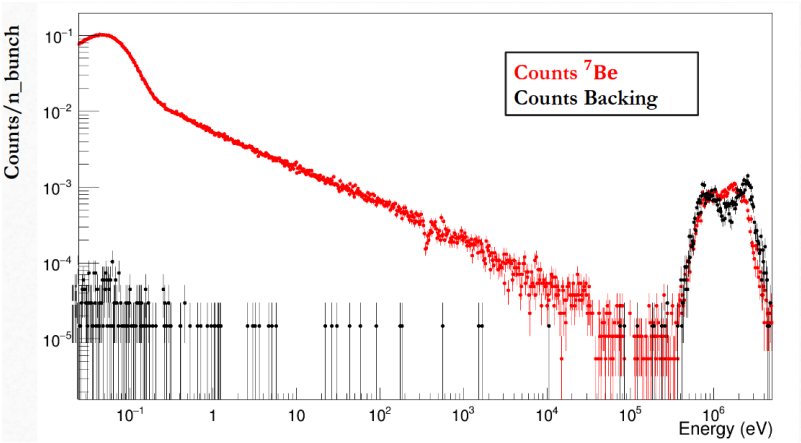

Figure 4.15: Comparison between the counts of protons coming from the interaction of the neutrons with the ^{7}Be plus the backing (red curve) and the counts coming just from the interaction of the neutron beam with the empty backing (black curve).

From the figure it can be clearly seen that this background contribution is important only for neutron energies above 500 keV, where in fact it dominates the measured yield. This energy represents the limit of the measurement as the background makes it impossible to extract the $^7Be(n,p)^7Li$ cross section above this energy. Figure 4.16 shows the ΔE vs E scatter plot obtained from the interaction of the neutron beam with the empty backing.

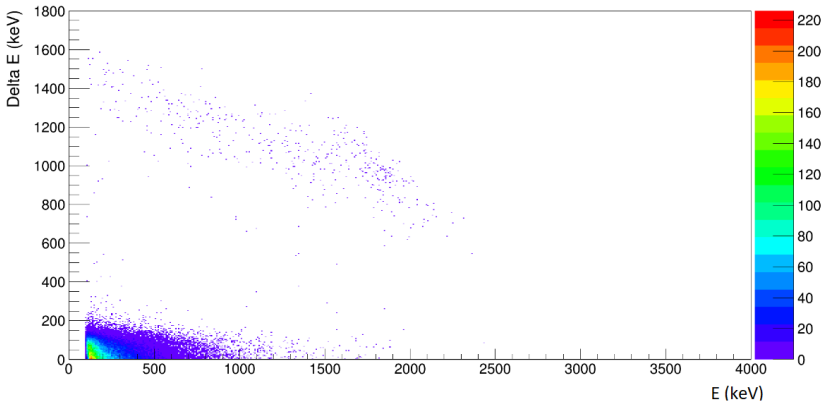

Figure 4.16: ΔE vs E scatter plot obtained from the interaction of the neutron beam with the empty backing.

The region corresponding to protons produced by the $^{14}N(n,p)$ reaction can be clearly seen, together with the background related to the electronic noise (or random γ-ray coincidences), which however is rejected by the conditions applied in the analysis.

4.4.2 Methods for the extraction of the ^{7}Be(n,p)^{7}Li cross section

To extract the $^{7}Be(n,p)^{7}Li$ cross section two independent methods were used according to the following equations:

Method 1:

$$\sigma_{n,p}(E_n) = \frac{C_{Be}(E_n) - B_{Be}(E_n)}{\epsilon_{Be}(E_n) \cdot \Phi(E_n) \cdot N_{Be} \cdot f_{C_{Be}}} \tag{4.4}$$

Method 2:

$$\sigma_{n,p}(E_n) = \frac{C_{Be}(E_n) - B_{Be}(E_n)}{C_{LiF}(E_n) - B_{LiF}(E_n)} \cdot \frac{\epsilon_{LiF}}{\epsilon_{Be}} \cdot \frac{f_{C_{LiF}}}{f_{C_{Be}}} \cdot \sigma_{LiF} \cdot \frac{N_{LiF}}{N_{Be}} \tag{4.5}$$

The first method is the same used for the reference reaction: C_{Be} represents the proton counts per bunch, B_{Be} the background per bunch, ϵ is the total detection efficiency of the set-up, Φ is the neutron flux, N_{Be} is the total number of atoms in the sample and $f_{C_{Be}}$, introduced to account for the target inhomogeneity mentioned above, is the convolution of the normalized neutron beam spatial profile and the nuclei distribution of the ^{7}Be target.

The second method, also called "the ratio method" allows to neglect the neutron flux, as the $^{7}Be(n,p)^{7}Li$ cross section is extracted with respect to the standard $^{6}Li(n,t)^{4}He$ cross section. However, in this case a few issues had to be addressed. In fact, as described in the previous chapter, while the implantation was originally designed to produce a uniform sample of 1.5 x 1.5 cm^2 area, the obtained deposit was highly inhomogeneous and with a gaussian profile of approximately 0.5 cm FHWM. Furthermore, the efficiency of the apparatus for the two reactions

is different, especially in the keV neutron energy region due to differences in the angular distribution of emitted particles. A correction for the inhomogeneities of the sample and for the efficiency had therefore to be applied in the analysis. In other words, the $^{7}Be(n,p)$ cross section cannot be simply determined from the rate of the $^{6}Li(n,t)$ reaction, considering that the fraction of the neutron beam intercepted by the two samples, as well as the detection efficiency, is significantly different for the two samples. For this reason, in the second method the $^{7}Be(n,p)^{7}Li$ cross section is extracted relative to that of the $^{6}Li(n,t)^{4}He$ reaction, from the ratio of the number of counts but taking into account the ratios of the efficiencies and beam-sample convolution factors. With this method, since the energy-dependent flux cancels out, the uncertainties are minimized and the systematic effects on the simulated efficiencies mostly compensate each other, except at higher energies.

The efficiency for the $^{7}Be(n,p)$ reaction was estimated by means of Monte Carlo simulations performed with GEANT4. However, contrary to the $^{6}Li(n,t)^{4}He$ case, for which the known angular distribution above 1 keV is used in the simulations, the emission of protons in the $^{7}Be(n,p)^{7}Li$ reaction is assumed to be isotropic at all energies as there are no data on such reaction. This assumption was verified a posteriori, on the basis of the levels of ^{8}Be contributing to the cross section. In fact, as it will be shown in the next chapter, up to 50 keV the cross section is dominated by negative parity compound levels, favoring s-wave proton emissions. Above this energy, this assumption may not hold anymore, leading to an additional 10% systematic uncertainty in the extracted cross section.

The selected physics lists in GEANT4 simulations were FTFP_BERT_HP and emstandard_opt0 and the efficiency has been evaluated by making a ratio between the coincidences of protons detected in all the strips and the number of protons produced in the interaction of a monoenergetic neutron beam with the ^{7}Be sample. Whenever a proton is produced in the simulations, it is recorded in a file, from which at the end the total number of protons is determined, at that particular neutron beam energy. The proton is then tracked, and if it enters the telescope, it is

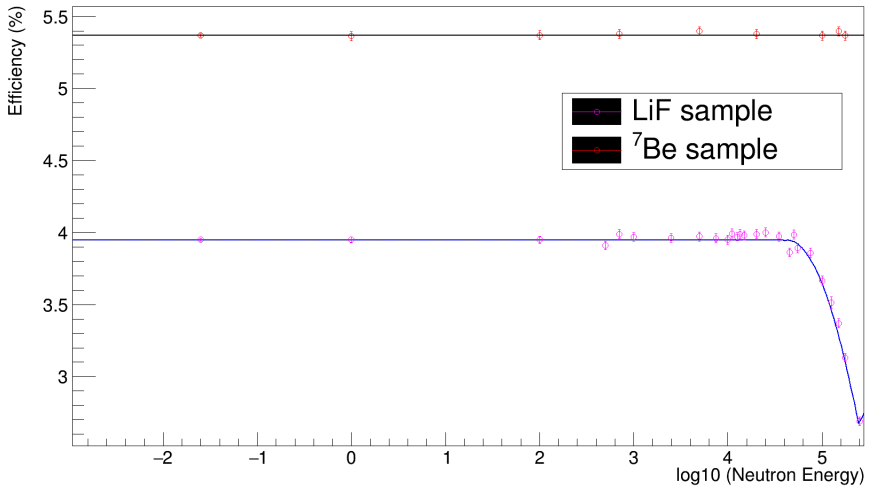

Figure 4.17: Efficiency for proton detection for the $^7Be(n,p)^7Li$ reaction compared with the efficiency of the triton detection for the $^6Li(n,t)^4He$ reaction.

analysed by means of the same coincidence tecnique used for the selection of protons in the real data. Also in this case the neutron beam profile simulated is Gaussian with a σ of 0.5 cm and a radius of 1 cm to match the spatial profile of the ^{7}Be deposit (and hence of the interaction region). The neutrons were generated along the y axis at -2 μm distance from the center of the target. The monoenergetic neutron beam energies used for the simulations were in total 9 and the number of neutrons for each energy was 10^8.

Figure 4.17 shows a comparison of the efficiencies for ^{7}Be and LiF samples. As expected, in the case of ^{7}Be the efficiency is flat, due to the assumption of an isotropic angular distribution. Further details regarding the simulated efficiency for ^{7}Be sample are reported in Table 4.2: the energy of the neutron beam, the number of protons produced in the target, the efficiency averaged over the number of iterations and the statistic errors are listed there.

Figure 4.18 shows the ratio between the $^7Be(n,p)^7Li$ cross section extracted with both methods described before. As it can be seen, the two methods lead to results compatible with each other.

As mentioned in the previous chapter, thanks to a collaboration

Neutron beam energy (eV)	Iterations	Protons	Average efficiency (%)	Statistic error
0.025	1	2700	5.368	0.01
1	2	2654	5.364	0.01
100	2	2500	5.37	0.023
700	3	2345	5.378	0.028
5000	7	1837	5.398	0.03
20000	9	1568	5.378	0.03
100000	11	1532	5.368	0.031
150000	12	1498	5.398	0.031
175000	12	1376	5.368	0.031

Table 4.2: Results of Geant4 simulations, in particular energies of the neutron beam, the number of protons produced in the target, the efficiency averaged on the number of iterations and the statistical errors are here reported.

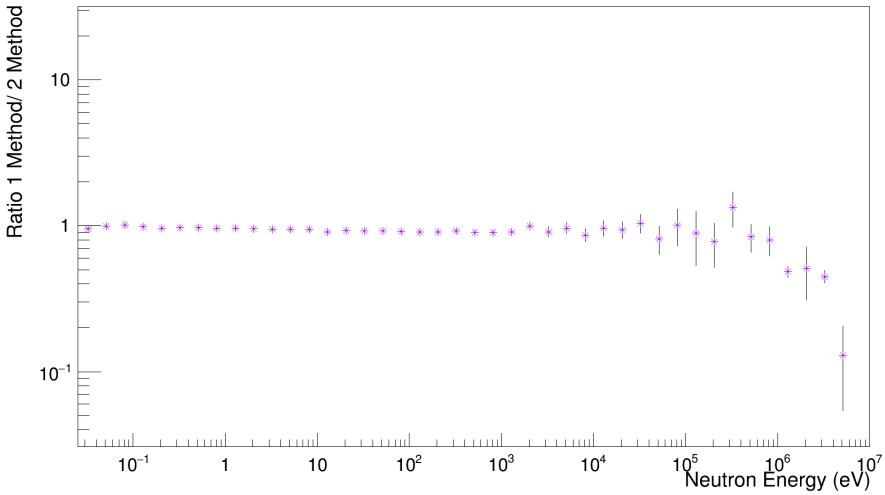

Figure 4.18: Ratio between the ^{7}Be(n,p)^{7}Li cross section extracted with Method 1 and 2 described in the text.

between PSI and ISOLDE, two ^{7}Be sample were produced with an activity of 20 MBq and 1.1 GBq respectively. In order to double check the results, data collected with the 20 MBq sample were analyzed following the same procedure described above. Figure 4.19 shows the ratio between the $^{7}Be(n,p)^{7}Li$ cross section extracted with the two ^{7}Be samples. A good agreement is observed, with the bigger error bars at higher energies due

to the low statistics for the 20 MBq sample. This agreement proves that there are no effects related to the sample preparation, the mass or the activity, while it does not provide information on the uncertainty effecting other factors (such as the detection efficiencies).

A final remark regards the systematic uncertainty on the $^7Be(n,p)$ cross section. As already mentioned, the main source of uncertainty in the cross section determination is related to the ^{7}Be sample inhomogeneity, which is approximately 8%. Other sources of uncertainty are related to the total mass of the sample, measured with an accuracy better than 2%, and the detection efficiency estimated to be affected by a 5% uncertainty. As a consequence, the total uncertainty on the $^7Be(n,p)$ cross section is 10% from thermal to 50 keV and could reach 15% above it, due to the estimated uncertainty related to assumption on the angular distribution of emitted protons.

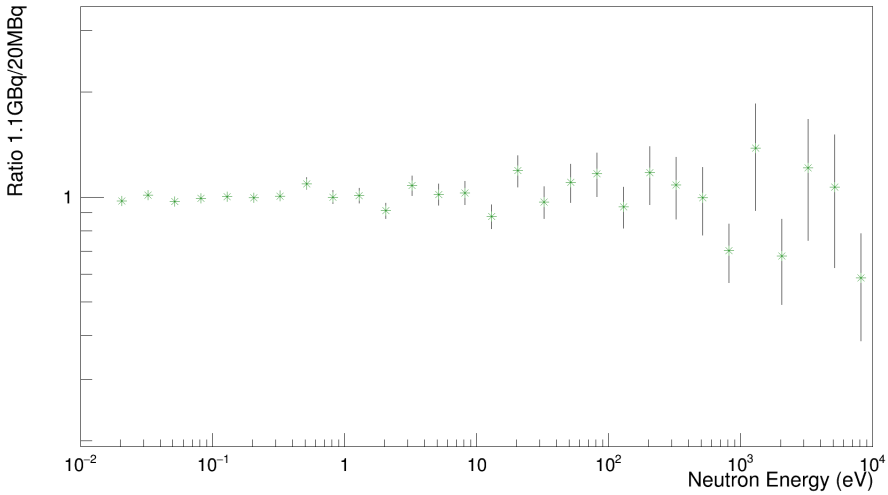

Figure 4.19: Ratio between the $^7Be(n,p)^7Li$ cross section extracted with the 20 MBq and 1.1 GBq ^{7}Be samples

Finally, Tabel 4.3 lists the combined estimated uncertainties in the measured (n,p) cross section, all in percent, with the systematics added in quadrature.

The symbol $*$ indicates the effect of the sample mass, flux normalization and detection efficiency. The 5% uncertainty above $E_n = 50$ keV

Energy	Statistical	Systematics			
		f_c	ang. dist	others (∗)	Total
0.01 eV $\leq E \leq 1keV$	1 - 5	8	0	5	10
1 keV $\leq E \leq 50keV$	5 - 10	8	5 - 10	5	10 - 15
E $\geq 50keV$		5			

Table 4.3: The estimated uncertainties in the measured (n,p) cross section, all in percent, with the systematic error added in quadrature.

is assumed considering that the time-reversal $^7Li(p,n)^7Be$ cross section, used above this energy instead of the n_TOF data (as discuss in the next chapter), is known with this level of accuracy.

Chapter 5

Results and Astrophysical implications

As shown in the previous chapter, to extract the $^7Be(n,p)^7Li$ cross section two independent methods were used. Since the results obtained were compatible with each other (see Figure 4.18), the choice fell on "the ratio method", which is not affected by uncertainties related to the flux and resolution of the neutron beam. In this method, the $^7Be(n,p)^7Li$ cross section is determined relative to the standard $^6Li(n,t)^4He$ one, by the following formula:

$$\sigma_{n,p}(E_n) = \frac{C_{Be}(E_n) - B_{Be}(E_n)}{C_{LiF}(E_n) - B_{LiF}(E_n)} \cdot \frac{\epsilon_{LiF}}{\epsilon_{Be}} \cdot \frac{f_{C_{LiF}}}{f_{C_{Be}}} \cdot \sigma_{LiF} \cdot \frac{N_{LiF}}{N_{Be}} \qquad (5.1)$$

that considers only the ratios of the number of counts (normalized to the respective total neutron fluence), of the efficiencies, of the beam-sample convolution factors and of the total number of atoms in the samples. Since the neutron flux doesn't play any role in this method, the uncertainties are minimized and systematic effects on the simulated efficiencies mostly compensate each other.

5.1. ^{7}Be(n,p)^{7}Li cross section

Figure 5.1 shows the $^{7}Be(n,p)^{7}Li$ reduced cross section (i.e. the cross section multiplied by the square-root of the neutron energy) as a function of neutron energy, compared to the previous direct measurements and to the ENDF evaluation. At thermal neutron energy, the n_TOF data

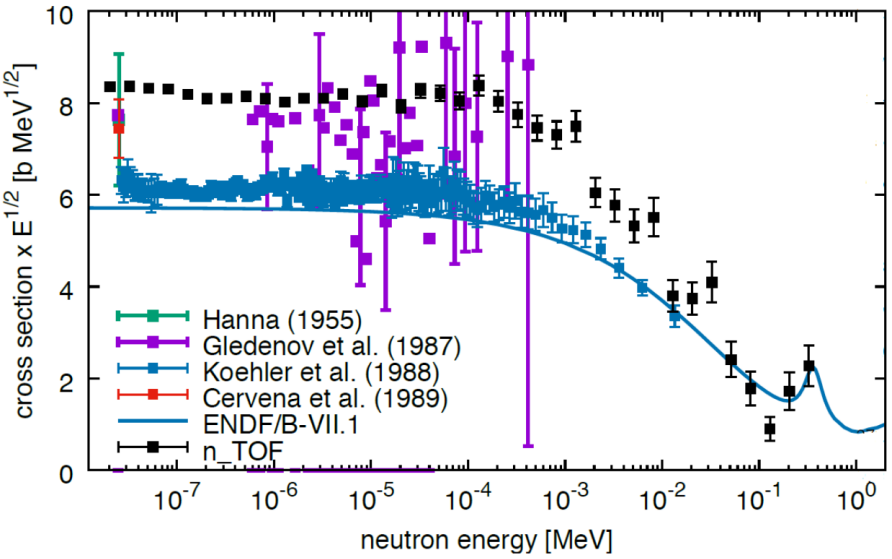

Figure 5.1: The $^{7}Be(n,p)^{7}Li$ reduced cross section measured at n_TOF compared with the results of previous measurements [50, 102, 51, 103] and with the ENDF/B-VII.1 library [101].

are 35% and 40% higher than the ones of Koehler et al. [50] and of the ENDF/B-VII.1 evaluation [101] respectively, while they are consistent with the results of Hanna [102], Gledenov et al. [51], and *Červená* et al. [103]. Our experimental value at thermal energy is 52.3 ± 5.2 kb. The quoted error represents only the systematic uncertainty, while the statistical errors are shown in the figure and at low energy (up to 1 keV) are between 1-5 %. Starting from 1 keV, the n_TOF data start to deviate less and less from ENDF, especially in the energy region of interest for the Cosmological Lithium Problem.

As mentioned in the previous chapter, due to the background generated by $^{14}N(n,p)$ reactions in the sample backing on which the ^{7}Be was

implanted, the n_TOF measurement extends only up to $\sim$ 325 keV, while above this energy the background dominates. In order to perform a reliable fit of the cross section, necessary to derive the corresponding reaction rate in the wide temperature range required by Big Bang Nucleosynthesis (BBN) network calculations, the n_TOF data must be complemented with data derived from the time-reversal reaction $^7Li(p,n)^7Be$. Indeed, at present, this reaction is the only way to obtain accurate data on the upper energy side of the energy spectrum. Therefore, due to their high statistic, the $^7Li(p,n)^7Be$ reaction data were used in the present work from 35 keV to $\sim$ 2 MeV. In particular, the $^7Li(p,n)^7Be$ cross section results have been adopted from Sekharan et al. [52] in conjunction with the following detailed balance relation, from time-reversal invariance of strong interaction:

$$\sigma_{n,p} = \frac{\sigma_{1,2}}{\sigma_{3,4}} \frac{k_{3,4}^2}{k_{1,2}^2} \frac{(2J_3+1)(2J_4+1)}{(2J_1+1)(2J_2+1)} \frac{1+\delta_{1,2}}{1+\delta_{3,4}} \tag{5.2}$$

Here, the direct and inverse reactions $1 + 2 \leftrightarrow 3 + 4$ are characterized by the center-of-mass momenta $k_{1,2}$ and $k_{3,4}$ and by the total angular momenta J_i of the reacting particles, while the δ's avoid double counting in the case of identical particles in the entrance and/or exit channel. This general expression simplifies to:

$$\sigma_{n,p} = \frac{k_p^2}{k_n^2} \sigma_{p,n} \tag{5.3}$$

in the specific case of p + ^{7}Li $\rightarrow$ n + ^{7}Be since $J_1 = J_3 = 1/2$ and $J_2 = J_4 = 3/2$, where k_p and k_n are the incident proton and outgoing neutron relative momenta in the center-of-mass system.

In Figure 5.2 the experimental data from the $^7Be(n,p)^7Li$ cross section measured at n_TOF, combined with the data obtained from the time-reversal $^7Li(p,n)^7Be$ reaction are shown. The data from the inverse reaction are reliable in the energy range above $\sim$ 35 keV (below this energy, threshold effects in the (p,n) data inhibit its use), and the good agreement with the n_TOF data in the region where they overlap provides

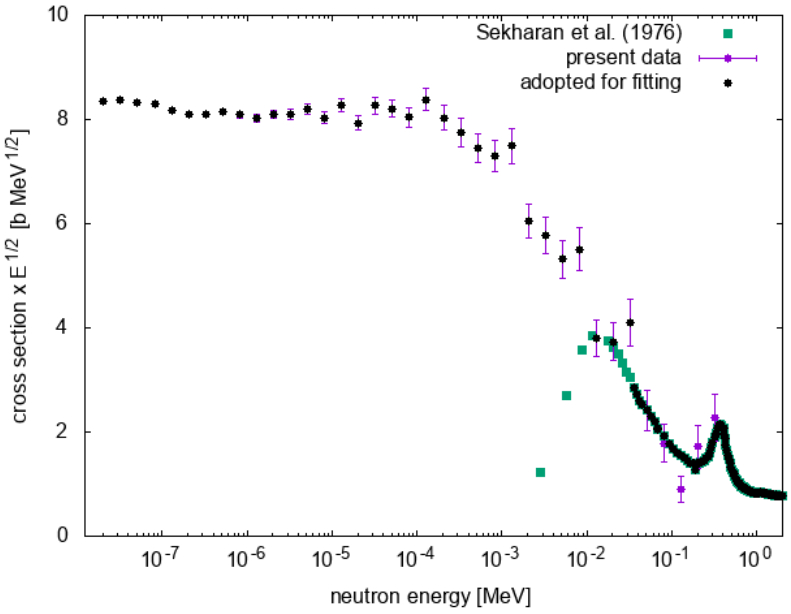

Figure 5.2: Experimental data from the $^{7}Be(n,p)^{7}Li$ cross section measured at n_TOF, combined with the data obtained from the time-reversal $^{7}Li(p,n)^{7}Be$ reaction.

additional confidence on the reliability of the n_TOF data at all energies. The $^{7}Li(p,n)^{7}Be$ data that have been adopted for the fit (discussed later on) are reported in black.

5.2. ^{8}Be levels

For spin-parity conservation, just few ^{8}Be levels participate in the $^{7}Be(n,p)^{7}Li$ reaction in the energy range of consideration here and they are the only ones used in the cross section fit described in the next section. As shown in Fig. 5.3 the cross section for this reaction is dominated by the 2^- state at E_x=18.89 MeV. The main contribution to the $^{7}Be(n,p)^{7}Li$ cross section, $\sigma(n,p_0)$, is due to transitions to the ground state in ^{7}Li, which has a spin-parity $J^\pi = 3/2^-$. The first exited state in ^{7}Li is at 478 keV and it has a spin-parity $J^\pi = 1/2^-$. Therefore, if a $J^\pi = 2^-$ state is formed by s-wave neutrons on ^{7}Be, the state cannot decay into ^{7}Li(1st) by emitting protons with l=0 (because of insufficient angular momentum),

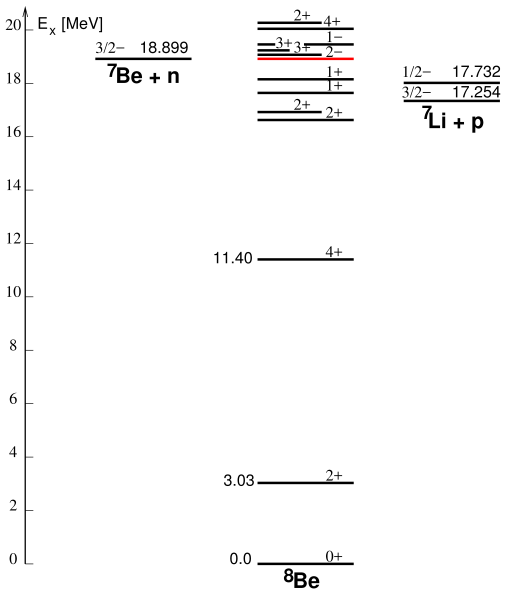

Figure 5.3: Energy levels for ^{7}Be, ^{8}Be, and ^{7}Li relevant for the (n,p) and (p,n) reactions.

nor with l=1 (because of the parity non-conservation). Therefore, the lowest orbital angular momentum of the emitted protons for the (n, p_1) exit channel is l=2. Since the 2^- state in ^{8}Be dominates the reaction mechanisms in a wide energy range, it is possible to estimate the $\sigma(n, p_1)$ contribution to the $^7Be(n, p)^7Li$ cross section. This component was not measured at n_TOF, since the protons from the (n,p_1) channel stop in the ΔE detector and cannot be identified. However, the contribution of this channel can be estimated from theoretical calculations [104], or assumed from previous measurements [50]. In both cases, the contribution is less than 2% in the energy range of interest for BBN.

5.3. R-matrix fit of the ^{7}Be(n,p)^{7}Li cross section

In order to determine the reaction rates, the maxwellian averaged cross section (MACS) must be evaluated. To do that, a maxwellian neutron spectrum is convoluted either directly with the data, or with the "fitted"

cross section, i.e. the cross section evaluated from the resonance parameters extracted from the data. To avoid fluctuations, the second method has been followed. To this end, a R-matrix analysis was performed by means of the code SAMMY. The purpose of the code is to analyze time-of-flight cross section data in the resolved and unresolved resonance regions, where the incident particle is either a neutron or a charged particle (p, α, d, ...). Bayes Theorem is used to find the best fit values of parameters and the associated parameter covariance matrix, that fit the data.

The adopted (n,p) cross section has been fitted with a R-matrix single-level Breit-Wigner expression:

$$\sigma_{n,p}(E_n) = \frac{\pi}{k_n^2} \sum_{r=1}^{N_r} g(J_r) \frac{\Gamma_{r,n}\Gamma_{r,p}}{(E_n - E_r)^2 + \frac{1}{4}\Gamma_r^2} \tag{5.4}$$

where

$$k_n = \frac{\sqrt{2\mu c^2 E_n}}{\hbar c}, \quad g(J) = \frac{2J+1}{2(2I_t+1)}, \quad \Gamma_r = \sum_{i=n,p,\alpha} \Gamma_{r,i}$$

μ is the reduced mass in the entrance channel, I_t the spin of the target nucleus ($I_t = 3/2$ in the present case), J_r is the resonance spin and E_r the resonance energy. Both, the neutron and charged-particle widths ($\Gamma_{r,n}$ and $\Gamma_{r,p}$ respectively), are taken to be energy dependent.

The Single Level Breit-Wigner (SLBW) formalism has been used in the full energy range, including all nine states ($N_r = 9$ levels) in ^{8}Be above 18.899 MeV (the neutron separation energy) and up to 22 MeV. For each resonance, the parameters available from the ENDF library have been adopted as starting values (see table 5.1).

The energy of each resonance, corresponding to the excitation energy of each state, as reported in the ENSDF library [105], has been kept constant in the fit, while the neutron and/or the proton widths have been allowed to vary, starting from the values reported in ENDF. In table 5.2 the final values are reported.

The SLBW (reduced) cross section is shown in Figure 5.4 and compared

#	E[MeV]	Ex[MeV]	l	J	$\Gamma_n[MeV]$	$\Gamma_p[MeV]$	$\Gamma_a[MeV]$	$\Gamma_{tot}[MeV]$
1	0.013	18.910	0	2.0	6.100e-02	6.100e-02	0.000e+00	1.220e-0
2	0.194	19.069	1	3.0	1.000e-03	2.710e-01	0.000e+00	2.720e-01
3	0.384	19.235	1	3.0	1.140e-01	1.140e-01	0.000e+00	2.280e-01
4	0.573	19.400	0	1.0	3.200e-01	3.200e-01	0.000e+00	6.400e-01
5	1.098	19.860	3	4.0	1.000e-03	2.100e-01	4.900e-01	7.010e-01
6	1.373	20.100	1	2.0	1.000e-01	1.270e-01	5.730e-01	8.000e-01
7	1.486	20.199	1	0.0	1.500e-01	1.500e-01	3.600e-01	6.600e-01
8	2.287	20.900	2	4.0	8.000e-01	8.000e-01	0.000e+00	1.600e+00
9	3.544	22.000	0	1.0	2.000e+00	2.000e+00	0.000e+00	4.000e+00

Table 5.1: Parameters available from the ENDF library that have been adopted as starting values.

#	E[MeV]	Ex[MeV]	l	J	$\Gamma_n[MeV]$	$\Gamma_p[MeV]$	$\Gamma_a[MeV]$	$\Gamma_{tot}[MeV]$
1	0.013	18.910	0	2.0	3.500e-02	1.190e-01	0.000e+00	1.540e-01
2	0.194	19.069	1	3.0	4.800e-02	4.150e-01	0.000e+00	4.630e-01
3	0.384	19.235	1	3.0	1.220e-01	7.500e-02	0.000e+00	1.970e-01
4	0.573	19.400	0	1.0	9.355e+00	3.390e-01	0.000e+00	9.694e+00
5	1.098	19.860	3	4.0	4.000e-03	4.400e-01	5.230e-01	9.670e-01
6	1.373	20.100	1	2.0	1.529e+00	1.258e+00	1.480e-01	2.935e+00
7	1.486	20.199	1	0.0	1.000e-01	1.000e-01	3.250e-01	5.250e-01
8	2.287	20.900	2	4.0	1.460e-01	1.243e+00	0.000e+00	1.389e+00
9	3.544	22.000	0	1.0	2.000e+00	2.000e+00	0.000e+00	4.000e+00

Table 5.2: Final values adopted for the fit.

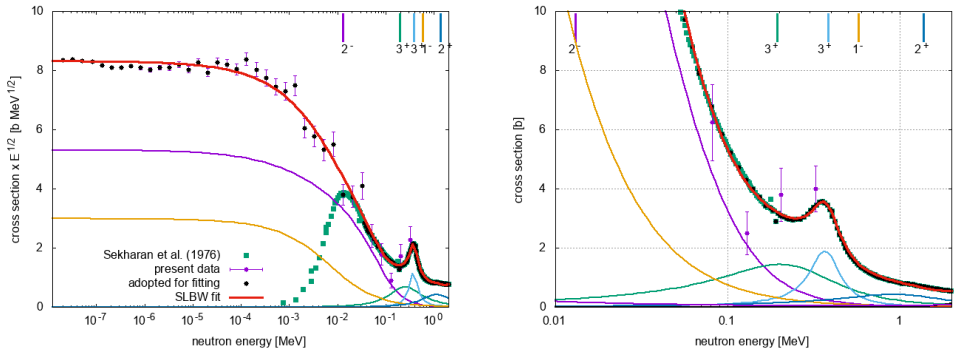

Figure 5.4: On the left adopted reduced (n,p) cross section in comparison with the SLBW fit obtained with the parameters of Table 5.2. On the right a zoom in the energy range above 10 keV.

with the adopted experimental data (for both the direct measurement at n_TOF and the inverse reaction data taken from the literature). Most of the resonance parameters should only be considered purely as fit parameters, optimized so to reproduce the adopted cross section and they do not necessarily represent accurate physical properties of the ^{8}Be excited states.

5.4. Comparison of the reaction rates for the ^{7}Be(n,p)^{7}Li reaction

In order to evaluate the reaction rate for the BBN calculations, once the resonance parameters fit of the (n,p) cross section have been extracted, the maxwellian averaged cross section (MACS) can be readily calculated numerically for a full set of thermal energies kT, using the formula:

$$\frac{<\sigma v>}{v_T} \equiv <\sigma> = \frac{2}{\sqrt{\pi}} \frac{1}{(kT)^2} \int_0^\infty E\sigma(E) e^{-E/kT} dE \qquad (5.5)$$

where k and T, respectively, are the Boltzman constant and temperature of the system, E is an energy of relative motion of the neutron with respect to the target, v is the relative velocity of neutrons and a target nuclide, and v_T is the mean thermal velocity given by:

$$\sqrt{\frac{2kT}{\mu}} \tag{5.6}$$

where μ is the reduced mass of the target nucleus and neutron. The MACS is then used to calculate the reaction rate, by means of the following formula:

$$N_A < \sigma v >= 10^{-24} < \sigma > 6.022 \times 10^{23} \times 3 \times 10^{10} \sqrt{\frac{2kT}{\mu c^2}} = 2.457 \times 10^8 \sqrt{\frac{A_1 + A_2}{A_1 A_2}} < \sigma > \sqrt{T_9} \tag{5.7}$$

where N_A is the Avogadro number. To express the reaction rates in [cm^3/(s·mole)] units, an additional factor of 10^{24} is introduced to express the $< \sigma >$ in barn; v_T is in units of [cm/s] and the temperature, T_9, in 10^9 degrees.

From Eq. 5.7 a numerical value of the reaction rate for a given temperature T_9 can be extracted. To understand the effect of the new cross section on the reaction rates, it is convenient to plot the ratio of the n_TOF reaction rates to those calculated by Cyburt (2004) [106], here assumed as reference. This can also be done for other, commonly adopted rates, such as those in [107, 108, 109]. Figure 5.5 shows such a ratio, as a function of the temperature, in the range $0.001 \leq T_9 \leq 10$. The temperature range of interest for BBN is indicated by the vertical light blue band. It can be seen that the present rate is significantly higher in a wide range up to $T_9 \sim 1$. The grey band represents the uncertainty on the reaction rates, obtained by propagating in Eq. 5.7 the maxwellian averaged uncertainty of the cross section $\Delta < \sigma >$:

$$\Delta < \sigma >= \frac{2}{\sqrt{\pi}} \frac{1}{(kT)^2} \int_0^\infty E \Delta\sigma(E) e^{-E/kT} dE \tag{5.8}$$

In order to express the reaction rate as a function of the temperature,

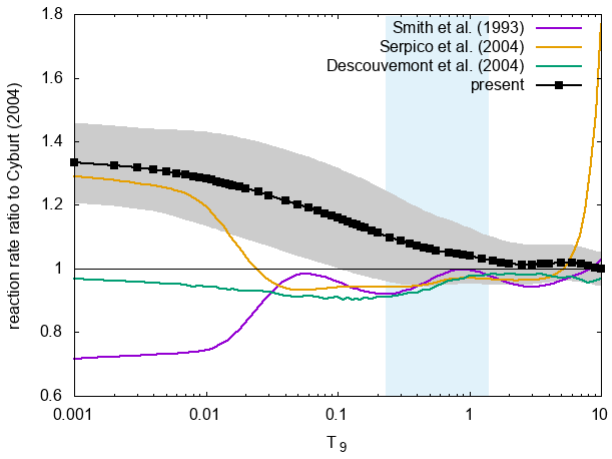

Figure 5.5: Comparison of the reaction rates for the $^7Be(n,p)^7Li$ reaction of the present work with the commonly adopted rate of Smith, Kawano and Malaney [107] and that derived from the evaluated cross section of ENDF/B-VII.1 library [101]. The temperature range of interest for BBN is indicated by the light blue grey band, while the error bars in the present data are indicated by the grey band.

a fit of the numerical results (black dots in Figure 5.5) have been done. The fitting function is a power expansion in T_9 (coefficients a_0 to a_5) plus an exponential term (a_6), as well as a resonance term (a_7):

$$N_A < \sigma v >= a_0(1+a_1)T_9^{1/2} + a_2T_9 + a_3T_9^{3/2} + a_4T_9^2 + a_5T_9^{5/2}) + a_6(\frac{1}{1+13.076T_9})^{3/2} + a_7T_9^{-3/2}e^{-b_0/T_9} \quad (5.9)$$

The values of the coefficients obtained from the fit are: a_0= 6.805e+09, a_1= -1.971e+00, a_2= 2.042e+00, a_3= -1.069e+00, a_4= 2.717e-01, a_5= -2.670e-02, a_6= 1.963e+08, a_7= 2.889e+07, and b_0= 2.811e-01.

5.5. Implications on the BBN

The standard BBN calculations have been performed using an updated version of the AlterBBN code of Alexander Arbey et al. [110]. It calculates the evolution of the Universe according to the standard model of the

	code index	reaction	adopted	options
1	12	$^1H(n,\gamma)D$	ando	ando, skm
2	16	$^3He(n,p)T$	stlb	stlb de04, skm
3	17	$^7Be(n,p)^7Li$	ntof	ntof, cy04, skm
4	19	$^7Be(n,\alpha)^4He$	ntof	wag, ntof
5	20	$D(p,\gamma)^3He$	il16	il16, skm
6	24	$^7Li(p,\alpha)^4He$	stlb	stlb, cf88, de04, skm
7	26	$T(\alpha,\gamma)^7Li$	stlb	stlb, skm
8	27	$^3He(\alpha,\gamma)^7Be$	il16	il16, ncr2, skm, cd08
9	28	$D(d,n)^3He$	stlb	stlb, skm
10	29	$D(d,p)T$	stlb	stlb, skm
11	30	$T(d,n)^4He$	stlb	stlb, de04, cf88, skm
12	31	$^3He(d,p)^4He$	stlb	stlb, de04, skm

Table 5.3: List of the 12th most important reactions in the BBN network. Wag: [111]; cf88: [112]; skm: [107]; de04: [108]; cy04: [106]; ando: [113]; il16: [114]; ncr2: fit to ncare2 library; stlb: fit to starlib table; ntof: rate from n_TOF experiments.

cosmological Big Bang, called Lambda-CDM (cold dark matter with a cosmological constant). Giving in input the 12 most important reactions of the BBN network with the relative reaction rates (details of the reaction rates used are given in Table 5.3), the code evaluates the evolution of the abundances as a function of time. Furthermore, the following conditions have been adopted in the code: the neutron average life-time $\tau_n = 880.2$ s, $N_\nu = 3$ neutrino species and the baryon-to-photon number density ratio $\eta_{10} = 6.09 \pm 0.06$ (η in units of 10^{-10})[8]. All the rates adopted for the twelve most important reactions are taken from [107].

The uncertainty or range of variation of the Lithium production is associated only to the corresponding variation of the $^7Be(n,p)^7Li$ reaction rate uncertainty. Calculations performed with an updated version of L. Kawano's code NUC123 [115] produced results of all the yields practically identical to those obtained with the AlterBBN code, once the reaction rates (and the Cosmology parameters) have been set the same. The ^{7}Li and ^{7}Be abundance, plotted vs η are shown in Figure 5.6. The yellow band represents the ^{7}Li abundance predicted by the observations, while the red one is the value of η derived directly from the measurements of the

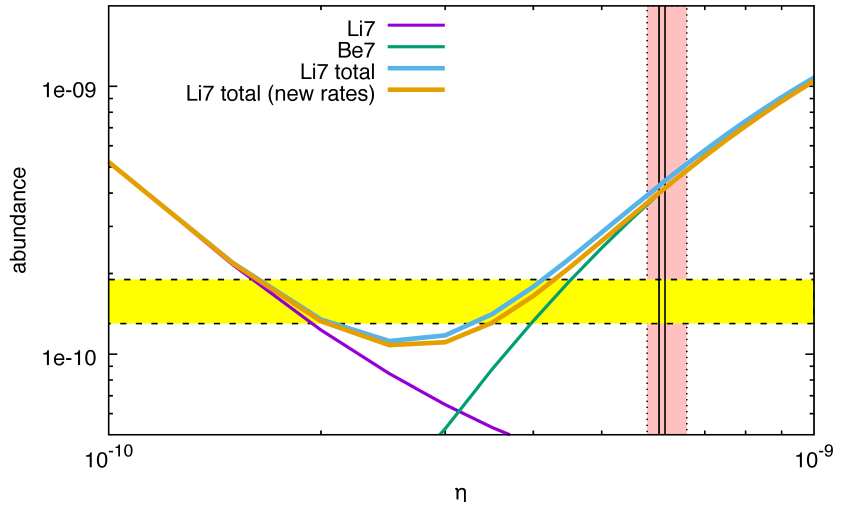

Figure 5.6: The ^{7}Li and ^{7}Be yields, plotted vs η. The total abundance of ^{7}Li obtained with the new rates calculated using the n_TOF cross section (orange curve), is compared with the predictions based on previous rates (blue curve).

Cosmic Microwave Background (CMB). Considering the abundance of ^{7}Li at the red band, it can be noticed that the new rates do not significantly modify the total production of ^{7}Li, leaving the CLiP still unresolved.

The results for the Li/H production are shown in Table 5.4 and in Figure 5.7 in comparison with other recent BBN calculations. The red line represents the value of the ^{7}Li abundance predicted by the observations. The estimation of the ^{7}Li abundance (relative to H) in this work with the new rate extracted from the $^{7}Be(n,p)^{7}Li$ cross section measurement have been done considering two values of η: η_{10}=6.09 $\pm$ 0.06 derived from the measurements of the Cosmic Background Radiation (CMB), and 5.8 $\leq$ η_{10} $\leq$ 6.3 obtained from BBN calculations, requiring an agreement with the measured values of ^{4}He and D abundances. All the values reported in Table 5.4 are the results of BBN calculations. Some authors evaluated the uncertainty of the results taking into account the uncertainties of all the reaction rates used in BBN calculations, while Mishra and Basu did not do so. The difference in the results obtained by Coc et al. in 2014 and in 2015 are simply due to different rates used. Looking at Figure

Mishra and Basu (2012) [116]	5.02
Coc et al. (2014)[117]	$4.94^{+0.40}_{-0.38}$
Coc et al. (2015) [118]	5.61 ± 0.26
Singh et al. (2017) [119]	4.45 ± 0.07
This work with standard rates	5.46
This work with present rate ($\eta_{10} = 6.09 \pm 0.06$)	5.26 ± 0.40
This work with present rate ($5.8 \leq \eta_{10} \leq 6.6$)	4.73-6.23
Observations [2]	1.6 ± 0.3

Table 5.4: BBN ^{7}Li abundance (relative to H) in units of 10^{10} calculated over the recent years, compared with the observation of the Spite-plateau in low-metallicity stars.

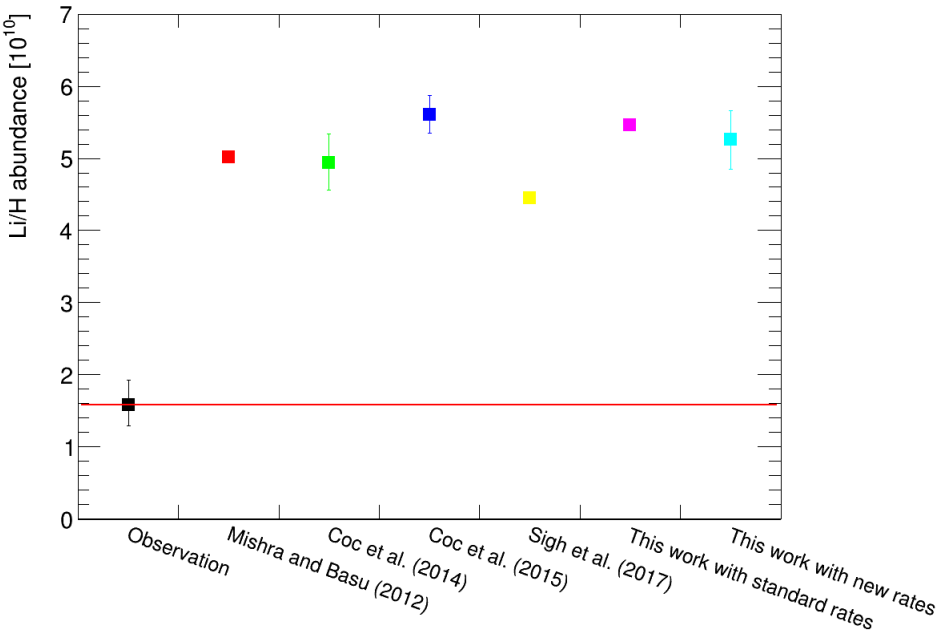

Figure 5.7: Comparison of the results for the Li/H production between this work and other recent BBN calculations.

5.7, it can be noticed that the result from Sigh et al. is quite lower with respect to all other evaluations. This is because a specific set of reaction rates was adopted, in particular for $^3He(\alpha,\gamma)^7Be$ a particularly "low" reaction rate was used, that leads to a lower production of ^{7}Be.

In conclusion, the new results from this work essentially lead to a 10% decrease in the Lithium production with respect to the previous calculation made using the "standard" rate (the rate from Ref.[106]) for the $^7Be(n,p)^7Li$ reaction. This variation does not change significantly the situation for the Cosmological Lithium Problem, leaving all alternative physical and astronomical scenarios still open for a possible solution.

Chapter 6

The ^{7}Li(p,n)^{7}Be cross section

Apart from the astrophysical motivation, the cross section of the $^7Be(n,p)^7Li$ reaction, determined in a wide energy range at n_TOF, has another important implication. As previously discussed, the $^7Be(n,p)^7Li$ and the $^7Li(p,n)^7Be$ reactions can be considered one the time-reversal reaction of the other. In Chapter 4 and 5, data on the $^7Li(p,n)^7Be$ reaction, well above the reaction threshold, have been used to infer the $^7Be(n,p)^7Li$ cross section at high energy (up to 1 MeV), in a range not covered by the n_TOF measurement. Analogously, the $^7Be(n,p)^7Li$ cross section at low energy can be inverted to obtain information on the $^7Li(n,p)^7Be$ reaction very close to the reaction threshold, where it is practically impossible to obtain accurate data in the direct proton-induced reaction. In this Chapter, this additional implication of the n_TOF data on the n+^{7}Be reaction is discussed.

6.1. The importance of ^{7}Li(p,n)^{7}Be cross section

The $^7Li(p,n)^7Be$ reaction, is one of the most important reactions for neutron production at low-energy accelerators, widely used for a variety of applications. In particular for proton energies slightly higher than 1912 keV, the neutrons emitted from thick ^{7}Li targets show a quasi-Maxwellian

energy distribution that reproduce the stellar neutron spectrum at kT $\sim$ 25 keV. This is a characteristic that makes this neutron source very important for astrophysics related studies [120].
The rapid rise of the $^7Li(p,n)^7Be$ cross section in the near threshold region makes this reaction very convenient for other applications as well. In particular, the high flux of low energy neutrons that can be produced with this reaction is very convenient for fundamental studies in radiobiology and dosimetry. Furthermore, it is a candidate as a neutron source for boron neutron capture therapy (BNCT) a cancer treatment modality, based on the use of ^{10}B carriers and thermal or epithermal neutron beams. Finally, this source is commonly used to calibrate neutron detectors and in a variety of other neutron beam applications.

The main advantage of the $^7Li(p,n)$ reaction as neutron source is the relatively low threshold of 1880.3 keV and the fast rise of the cross section as a function of energy. These characteristics imply that high-flux neutron beams can be easily obtained with low energy accelerators and a thick targets of ^{7}Li or ^{7}Li compounds (were the thickness is such to stop the protons inside the target itself).

One of the main requirements of a $^7Li(p,n)$ neutron source is the accurate estimate of the neutron yield and energy distribution. This is particularly important for astrophysical applications, where the energy distribution of the neutron beam strongly affects the measurement of relevant quantities (such as the MACS). Therefore, the high accuracy determination of the excitation function of this reaction is of crucial importance for an accurate estimate of the neutron yield and spectrum in thick targets (see for example Ref.[121, 122]).

6.2. Difficulties in the measurement of ^{7}Li(p,n)^{7}Be cross section

Direct measurements of the $^7Li(p,n)^7Be$ reaction cross section near the threshold (E_p =1880.3 keV) are difficult to perform since neutrons are

emitted with low energy ($\sim$ 30 keV at the threshold) and therefore are difficult to detect. Furthermore, due to the fact that the $^7Li(p,n)^7Be$ cross section rise quickly near the threshold, a proton beam with very narrow energy distribution, stable and well calibrated in energy is needed. Finally,

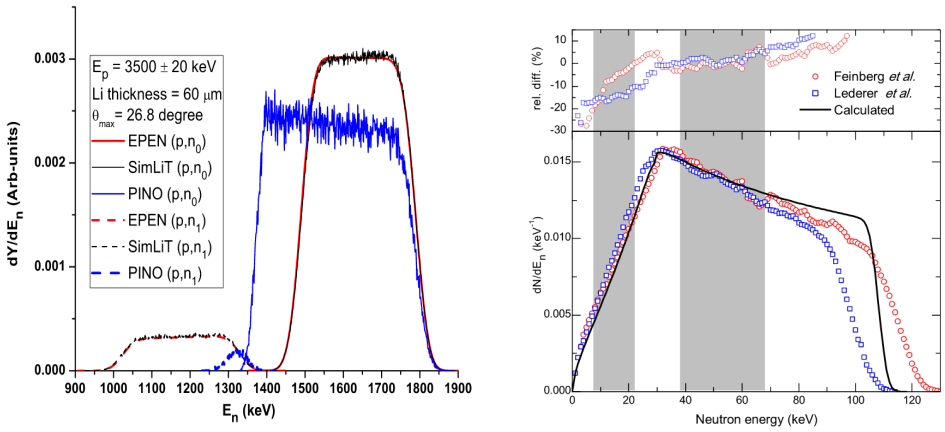

Figure 6.1: Left panel: comparison between the spectra obtained with a deterministic neutron source spectrum code EPEN and with two Monte Carlo codes, SimLiT and PINO for a 60μm-thick lithium target at E_p = 3500 $\pm$ 20 keV [123, 124]. Right panel: Neutron spectra from Feinberg et al. (open circles) and Lederer et al. (open squares) both measured at E_p = 1912 keV [123, 125] compared with a measurement performed at BELINA (black curve) [126].

the energy loss of protons inside the target, even if very thin, worsen the resolution of the proton beam. For all these reasons, discrepancies exist between various datasets near threshold (as will be shown later on). Clearly, this situation reflects on the predictions of the neutron yield and energy distribution that can be produced with a thick ^{7}Li target at a given proton energy. For example, left panel of Figure 6.1 shows a comparison between the spectra obtained with a deterministic neutron source spectrum code EPEN [123] and with two Monte Carlo codes, SimLiT [123] and PINO [124] for a 60μm-thick lithium target at E_p = 3500 $\pm$ 20 keV. A perfect match can be observed between the neutron spectra predicted with EPEN and SimLiT for both (p,n_0) and (p,n_1) contributions, while PINO shows large discrepancy from EPEN and SimLiT for both (p,n_0) and (p,n_1) contributions. Another example of the uncertainties in the measured and calculated neutron spectrum from

the $^7Li(p,n)$ source is shown in the right panel of Figure 6.1, where the neutron spectra from Feinberg et al. [123] (open circles) and Lederer et al. [125] (open squares) both measured at E_p=1912 keV are compared with the spectrum calculated by G. Martin-Hernandez et al. for the BELINA facility at the same proton energy [126] (black curve). Also in this case dicrepancies between neutron spectra are evident, showing once again the uncertainty associated with both measurements and calculations of the neutron yield from the $^7Li(p,n)$ reaction.

6.3. The ^{7}Li(p,n)^{7}Be cross section from the present ^{7}Be(n,p)^{7}Li data

As already mentioned, the time-reversal $^7Be(n,p)^7Li$ data are not affected by the experimental problems described above which make the direct measurement of the $^7Li(p,n)$ reaction near threshold very uncertain. Therefore, the n_TOF data can be used for a very accurate determination of the $^7Li(p,n)^7Be$ cross section very close to the threshold. To this end, the time-reversal invariance, mentioned in the previous chapter, can be used to derive the $^7Li(p,n)^7Be$ cross section from the measured $^7Be(n,p)^7Li$ cross section through the following equation:

$$\sigma_{p,n} = \frac{k_n^2}{k_p^2}\sigma_{n,p} \tag{6.1}$$

The results are shown in Figure 6.2. In the left panel, the $^7Li(p,n)^7Be$ cross section near threshold is shown (black symbols). The right panel instead, shows the cross section in the full energy range up to E_p = 2 MeV. For comparison, the data from measurements of the near-threshold (p,n) reaction (Refs. [52, 127]) are also shown. Relative to the direct measurements, the cross section extracted from the n_TOF $^7Be(n,p)^7Li$ data shows a much faster rise just above the threshold, as it is not affected by the resolution problems of direct measurements. The ENDF/B-VII.1 [101] cross section and the Single Level Breit-Wigner (SLBW) fit

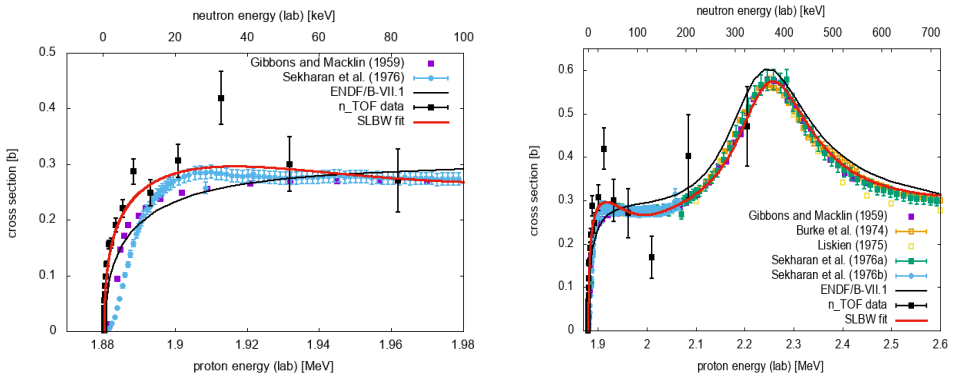

Figure 6.2: Left panel: the cross section of the $^7Li(p,n)^7Be$ (black symbols), obtained by time-reversing the n_TOF data of the reaction. For comparison, the data from measurements of the near-threshold (p,n) reaction (Refs. [52, 127]) are also shown. Right panel: the $^7Li(p,n)^7Be$ cross section in the full energy range up to $E_p = 2$ MeV.

calculated with the resonance parameters of Table 5.2, are plotted as well. The fit nicely reproduces the cross section all the way from the reaction threshold to 2 MeV. Relative to the ENDF evaluated cross section, typically used in calculations of the ^{7}Li-based neutron source, the new fit is higher just above the threshold, while it is systematically lower at higher energy. It can therefore be expected that thick target neutron yields calculated on the basis of the new fit will be lower than the one predicted by ENDF, with also a slight change in the energy distribution of the emitted neutrons. In particular, given the fast rise of the cross section near the threshold, more low-energy neutrons will most probably be emitted than previously believed. More detailed calculations are needed to estimate the effect of the new data on the yield and energy distribution of neutrons from the $^7Li(p,n)$ source. Nevertheless, it can be concluded here that the combination of the time-reversal $^7Be(n,p)$ data collected at n_TOF with the results of direct measurements leads to a new very accurate excitation function for the $^7Li(p,n)^7Be$ reaction, that can be used for more reliable predictions of the neutron beams that can be produced with the near-threshold $^7Li(p,n)$ reaction.

Conclusions

The present Ph.D. thesis regards a measurement of the $^7Be(n,p)^7Li$ reaction, performed in the recently constructed second experimental area (EAR2) at the neutron time-of-flight facility n_TOF at CERN. The main motivation of this work is related to the Cosmological Lithium Problem in Big Bang Nucleosynthesis (BBN), one of the most puzzling and long-standing issues in Nuclear Astrophysics. In fact, despite 50 years of efforts, standard Big Bang Nucleosynthesis calculations still largely overestimate (roughly by a factor of three), the observations of the primordial ^{7}Li abundance. While during the first minutes after the Big Bang ^{7}Li is produced and destroyed by nuclear reactions, almost all primordial ^{7}Li is produced at later times by the electron capture decay of ^{7}Be. A reduction of ^{7}Be surviving BBN would therefore automatically reduce the abundance of primordial ^{7}Li.

Among neutron-induced reactions, the $^7Be(n,p)^7Li$ is believed to be the mayor responsible of ^{7}Be destruction during BBN, accounting for 97% of the total destruction rate of this isotope. Despite its importance, data on this reaction were scarce and discrepant among each others, covering just partially the neutron energy region of interest for the Big Bang Nucleosynthesis. The lack of reliable data is essentially due to the intrinsic difficulty of the measurement, since the short half life of ^{7}Be (53 days corresponding to a high specific activity of 13 GBq/μg), poses severe problems in terms of background and radioprotection issues. These difficulties could be overcome at n_TOF thanks to the extremely high instantaneous neutron flux (10^8 n/cm^2/pulse) of the second experimental

area (EAR2) that results in a high signal to background ratio for radioactive samples. For this reason, a measurement of the $^7Be(n,p)^7Li$ reaction cross section was proposed and performed at n_TOF, covering for the first time a wide energy range (from thermal up to 400 keV), including the one of interest for the Big Bang Nucleosynthesis.

The $^7Be(n,p)^7Li$ reaction is characterized by a high cross section, of thousand of barns, at thermal energy and several barns in the range of BBN interest (from 20 to 200 keV). This feature, combined with the high neutron flux, allowed to perform the measurement with a sample of mass as low as 90 ng mass, corresponding to 1 GBq total activity. On the other hand, the reaction has a low Q-value (1.64 MeV) with the consequence that the protons are emitted with a low energy of 1.44 MeV. For this reason, a low noise and a high sensitivity set-up had to be used in order to allow the identification of the emitted protons as a signature of the reaction. To this aim, a ΔE-E telescope was used, made of silicon strip detectors of 20 (ΔE) and 300 micron thickness (E), and 5×5 cm^2 area. This technique allowed a very efficient rejection of the background related to spurious particles, in particular the 478 keV γ-rays emitted in the EC decay of ^{7}Be.

In order to avoid background from other reaction channels on the sample backing or contaminants, a target material as pure as possible was needed for the experiment. Thanks to a collaboration of two different laboratories, Paul Scherrer Institut (PSI) and Isolde at CERN, two high-purity ^{7}Be samples of 20 MBq and 1.1 GBq activity were produced. A sufficient amount of ^{7}Be was extracted from the cooling water of the Swiss Spallation Neutron Source (SINQ) facility at PSI and chemically purified in that laboratory. Subsequently, it was sent to CERN, were ^{7}Be was isotropically separated and implanted at ISOLDE. The samples were later characterized, in terms of total mass and uniformity, at PSI. The ^{7}Be sample of 1.1 Gbq activity (the one used for the evaluation of the $^7Be(n,p)^7Li$ cross section) resulted 99% pure, with 1% of ^{7}Li contamination. It was also found that the deposit was highly inhomogeneous with a gaussian profile of approximately 0.5 cm FHWM. The collaboration between PSI,

ISOLDE and n_TOF made the measurement of the $^{7}Be(n,p)^{7}Li$ cross section, the first one performed with a neutron beam impinging on a sample produced at a Radioactive Beam Facility.
The $^{7}Be(n,p)^{7}Li$ cross section was evaluated relative to the $^{6}Li(n,t)$ cross section (that is standard from thermal up to 1 MeV neutron energy), from the ratio of the number of counts of the two reactions (normalized to the same neutron fluence), the ratio of the efficiencies and of the beam-sample convolution factors of both ^{7}Be and ^{6}LiF sample. At low energies, the $^{7}Be(n,p)^{7}Li$ cross section measured at n_TOF is ∼40% higher than current evaluations (based on one of the two previous measurements), while above 1 keV it starts to deviate less from the evaluation, finally showing a good agreement in the region of interest for the Cosmological Lithium Problem. The n_TOF data reach up to ∼325 keV neutron energy, since at higher energy the background due to the $^{14}N(n,p)$ reactions in the sample backing dominates. For this reason, in order to obtain a reliable fit of the cross section in the wide temperature range required by BBN network calculations, the n_TOF data were complemented with the very accurate ones from the time-reversal reaction $^{7}Li(p,n)^{7}Be$. In order to determine the astrophysical reaction rates of the $^{7}Be(n,p)^{7}Li$ reaction, the maxwellian averaged cross section (MACS) has been evaluated, by convoluting the stellar neutron spectrum with the reaction cross section. In order to avoid statistical fluctuations, the experimental data were fitted with the R-Matrix analysis code SAMMY using a single-level Breit-Wigner formalism in the full energy range, including all nine states in ^{8}Be above the neutron separation energy. The reaction rate was extracted from the MACS in the temperature range $0.001 \leq T_9 \leq 10$. While it is found significantly higher with respect to the commonly adopted rates up to $T_9 \sim 1$, at higher temperatures a smaller deviation from previous calculations is found. Overall, an estimate of the ^{7}Be destruction rate based on the n_TOF data here reported, leads to a decrease of the theoretically predicted cosmological Lithium abundance of ∼10%. This result is clearly insufficient to solve the Cosmological Lithium Problem, and rules out one of the last possible nuclear solutions as a potential explanation of the

Cosmological Lithium Problem.

Acknowledgments

Questi sono stati tre anni in cui ho imparato molto sia dal punto di vista professionale che da quello umano e questo lo devo principalmente ai miei due relatori: Nicola e Pino.

Grazie Nicola per la tua pazienza e dedizione, sei stato la mia guida e l'esempio da seguire durante il mio dottorato. Sei una persona molto disponibile e anche una delle piú intelligenti che io conosca e questo ti rende davvero speciale. Col tuo aiuto ho imparato tante cose e spero che la fine di questo percorso non mi impedisca di apprenderne molte altre ancora assieme a te.

Pino, con te lavorare diventa un piacere perché riesci sempre a trovare un approccio semplice ed efficace ad ogni mio problema. Mi hai insegnato a non perdermi mai d'animo e ad affrontare anche le situazioni piú difficili senza mai trascurare il sorriso. Sei stato il mio punto di riferimento per la misura di ^{89}Y e ^{88}Sr, grazie.

I miei ringraziamenti vanno anche ad Alberto Mengoni la cui esperienza e professionalitá sono state fondamentali per la stesura di questa tesi, specialmente per l'ultimo capitolo.

Un riconoscimento particolare va a Massimo Barbagallo, lo spokesperson di questo esperimento nonché amico e collega, che si é distinto nell'organizzazione e coordinazione della misura e che mi ha sempre aiutato nell'analisi ogni qualvolta ne avessi bisogno.

Mario Mastromarco, come sempre a te piace aiutare da dietro le quinte perché sei una delle persone piú umili e buone che io conosca. Per questo motivo vorrei ricordare in queste righe quanto tu sia stato essenziale per

la riuscita dell'esperimento.

Grazie ad n_TOF che nel corso di questi tre anni é diventata un po' anche la mia famiglia specialmente durante il periodo trascorso al CERN. Vivere lontani da casa non é mai facile, ma con voi é stato tutto piú divertente e stimolante. Siete entrati tutti nel mio cuore.

Dulcis in fundo grazie alla mia famiglia, che ovviamente comprende anche il mio amore Aronne, alla quale ho voluto dedicare questo lavoro di tesi. Mi siete stati sempre accanto, dandomi il vostro sostegno nei momenti difficili e gioendo con me per ogni soddisfazione, dalla piú piccola alla piú grande con l'entusiasmo sempre alle stelle. Spero siate fieri di me come io lo sono di voi.

Bibliography

[1] B. D. Fields, P. Molaro, and S. Sarkar, Chin. Phys. **C38**(2014), arXiv:1412.1408.

[2] R. H. Cyburt, B. D. Fields, K. A. Olive, and T.-H. Yeh, Rev. Mod. Phys. **88**, 015004 (2016), arXiv:1505.01076.

[3] Astronomy Astrophysics. **594** (13): A13. arXiv:1502.01589, doi:10.1051/0004-6361/201525830.

[4] B. Ryden, "Introduction to Cosmology", p.196 Addison-Wesley (2003).

[5] B. Follin et al., Phys. Rev. Lett. **115**, 091301, (2015).

[6] C. A. Bertulani and T. Kajino, Prog. Part. Nucl. Phys. **89**, 56 (2016).

[7] The ALEPH Collaboration, The DELPHI Collaboration, The L3 Collaboration, The OPAL Collaboration, The SLD Collaboration, The LEP Electroweak Working Group, The SLD Electroweak and Heavy Flavor Groups, Phys. Reports **427**, 257 (2006).

[8] C. Patrignani, et al. (Particle Data Group), Chinese Phys. **C40**, 100001 (2016).

[9] Goddard Space Flight Center, "Wilkinson Microwave Anisotropy Probe: Overview". August 4, 2009.

[10] W. Hu, S. Dodelson, Annu. Rev. Astron. Astrophys. 40:171 (2002), arXiv:astro-ph/0110414.

[11] E. Komatsu, et al., Ap. J. 192, 18 (2011).

[12] P. A. R. Ade, et al., Astron. Astrophys. 594, A13 (2016).

[13] B. D. Fields, Annu. Rev. Nucl. Part. Sci., 61 (2011), p. 47.

[14] M. Pospelov, arXiv:1011.1054v1, 4 Nov 2010.

[15] A. Coc, E. Vangioni-Flam, P. Descouvemont, A. Adahchour, C. Angulo, Ap. J. 600:544 (2004), astro-ph/0309480.

[16] Grant J. Mathews, Motohiko Kusakabe, Toshitaka Kajino, International Journal of Modern Physics E. arXiv:1706.03138v1 [astro-ph.CO] 9 Jun 2017.

[17] S. Burles, D. Tytler, Ap. J. 507:732 (1998), arXiv:astro-ph/9712109.

[18] J. M. OMeara, D. Tytler, D. Kirkman, N. Suzuki, J. X. Prochaska, et al., Ap. J. 552:718 (2001), arXiv:astro-ph/0011179.

[19] D. Kirkman, D. Tytler, N. Suzuki, J. M. OMeara, D. Lubin, Ap. J. Supp. 149:1 (2003), arXiv:astro-ph/0302006.

[20] J. M. OMeara, S. Burles, J. X. Prochaska, G. E. Prochter, R. A. Bernstein, K. M. Burgess, Ap. J. Lett. 649:L61 (2006), arXiv:astro-ph/0608302.

[21] M. Pettini, B. J. Zych, M. T. Murphy, A. Lewis, C. C. Steidel, Mon. Not. Roy. Astr. Soc. 391:1499 (2008), 0805.0594.

[22] K. A. Olive, E. D. Skillman, New Astron. 6:119 (2001).

[23] K. A. Olive, E. D. Skillman, Ap. J. 617:29 (2004), arXiv:astro-ph/0405588.

[24] A. Peimbert, M. Peimbert, V. Luridiana, Ap. J. 565:668 (2002), arXiv:astro-ph/0107189.

[25] Y. I. Izotov, T. X. Thuan, Ap. J. 500:188 (1998).

[26] Y. I. Izotov, T. X. Thuan, Ap. J. 602:200 (2004), arXiv:astro-ph/0310421.

[27] T. M. Bania, R. T. Rood, D. S. Balser, Space Sci. Rev. 130:53 (2007).

[28] E. Vangioni-Flam, K. A. Olive, B. D. Fields, M. Cass, Ap. J. 585:611 (2003), arXiv:astro-ph/0207583.

[29] M. Spite, F. Spite, Nature 297, 483-485 (1982).

[30] Y. I. Izotov and T. X. Thuan, Ap. J. Lett. 710, L67 (2010).

[31] M. Peimbert, https://arxiv.org/pdf/0811.2980.

[32] L. Sbordone, et al., AA 522, A26 (2010).

[33] L. S. Lyubimkov, https://arxiv.org/pdf/1701.05720.

[34] M. Pinsonneault, Annu. Rev. Astron. Astrophys. 35:557.

[35] S. Talon, C. Charbonnel, Astron. Astrophys. 418:1051 (2004), arXiv:astroph/0401474.

[36] O. Richard, G. Michaud, J. Richer, Ap. J. 619:538 (2005), arXiv:astroph/0409672.

[37] M. H. Pinsonneault, C. P. Deliyannis, P. Demarque, Ap. J. Supp. 78:179 (1992).

[38] W. Aoki, P. S. Barklem, T. C. Beers, N. Christlieb, S. Inoue, et al., Ap. J. 698:1803(2009), 0904.1448.

[39] A. Hosford et al., Astron. Astrophys. 493:601 (2009), 0811.2506.

[40] J. Melendez et al., Astron. Astrophys. 515:L3 (2010), 1005.2944.

[41] R. H. Cyburt, B. D. Fields, K. A. Olive, Phys. Rev. D69:123519 (2004), arXiv:astro-ph/0312629.

[42] C. Broggini et al., DOI https://arxiv.org/pdf/1202.5232.pdf.

[43] C. Angulo et al., Astrophysical J. 630, L105 (2005).

[44] P. D. OMalley et al., Phys. Rev. C84, 042801(R) (2011).

[45] F. Ajzenberg-Selove, Nucl. Phys. A 506, 1 (1990).

[46] P. Bassi et al., Il Nuovo Cimento XXVIII, 1049 (1963).

[47] R. V. Wagoner, Astrophys. J. 148, 3 (1967).

[48] M. Sabat-Gilarte et al., Eur. Phys. J. A (2017) 53: 210.

[49] M. Barbagallo et al., Phys. Rev. Lett. 117, 152701 (2016).

[50] Koehler P.E. et al., Phys. Rev., **C37** (1988), p. 917.

[51] Yu. M. Gledenov, T. S. Zvarova, M. P. Mitrikov, R. S. Mitrikova, Yu. P. Popov, V.I. Salatskiy, Fung-Van-Zuan, in: Int. Conf. on Neutron Physics, Kiev, 1418 Sep 1987, Vol.2, (1987) 232, USSR.

[52] K. K. Sekharan, H. Laumer, B. Kern, and F. Gabbard, Nucl. Instrum. Meth. 133, 253 (1976).

[53] A. Goudelis et al., arXiv:1510.08858v2, 24 May 2016.

[54] A. Coc, N. J. Nunes, K. A. Olive, J. Uzan, E. Vangioni, Phys. Rev. D 76:023511 (2007), arXiv:astro-ph/0610733.

[55] V. V. Flambaum, E. V. Shuryak, Phys. Rev. D 65:103503 (2002), arXiv:hep-ph/0201303.

[56] V. F. Dmitriev, V. V. Flambaum, J. K. Webb, Phys. Rev. D 69:063506 (2004), arXiv:astro-ph/0310892.

[57] J. L. Feng, Annu. Rev. Astron. Astrophys. 48:495 (2010), 1003.0904.

[58] D. Hooper, E. A. Baltz, Annual Review of Nuclear and Particle Science 58:293 (2008), 0802.0702.

[59] R. J. Gaitskell, Annual Review of Nuclear and Particle Science 54:315 (2004).

[60] J. Ellis, J. E. Kim, D. V. Nanopoulos, Physics Letters B 145:181 (1984).

[61] K. Jedamzik, Phys. Rev. D 70:083510 (2004), arXiv:astro-ph/0405583.

[62] E. Chiaveri (The n_TOF Collaboration), Technical Report CERN-INTC-2012-029, INTC-O-015, February 2012.

[63] S. Marrone et al., Nuclear Instruments and Methods in Physics Research A 517 (2004) 389-398.

[64] CERN Bullettin Issue No. 32-34/2014 - Monday 4 August 2014.

[65] The n_TOF Collaboration, Eur. Phys. J. A (2013) 49: 27.

[66] G. Lorusso et al., Nucl. Instr. and Meth. A 532 (2004) 622-630.

[67] D. J. Simon, Proc. of EPAC 96, Sitges 1996, p.295.

[68] M. Calviani et al., ICANS XIX, n_TOF-CONF-2010-2011.

[69] Fluka, CERN-INFN. www.fluka.org/fluka.php.

[70] N. Colonna et al., Progress in Particle and Nuclear Physics 101 (2018) 177-203.

[71] L. Damone., Tesi di laurea magistrale, (2013-2014).

[72] A. D. Carlson et al., Nucl. Data Sheets 110, 3215 (2009).

[73] A.D. Carlson, Metrologia 48, S328 (2011).

[74] L. Cosentino et al., Rev. Sci. Instrum. 86, 073509 (2015).

[75] I. Giomataris et al., Nucl. Instrum. Methods A 376, 29 (1996).

[76] S. Andriamonje et al., J. Korean Phys. Soc. 59, 1597 (2011).

[77] I. Giomataris, R. De Oliveira, Patent CEA-CERN, Application Number 09 290 825.0 (2009).

[78] C. Paradela et al., Phys. Rev. C 82, 034601 (2010).

[79] D. Tarrio et al., Phys. Rev. C 83, 044620 (2011).

[80] C. Weiss et al., Nuclear Instruments and Methods in Physics Research A 799 (2015) 90-98.

[81] J. Lerendegui-Marco et al., Eur. Phys. J. A (2016) 52: 100.

[82] Y. H. Chen, EPJ Web of Conferences 146, 03020 (2017).

[83] M. Diakaki, n_TOF Collaboration meeting, Madrid 2017, https://indico.cern.ch/event/767271/.

[84] L. Cosentino et al., https://arxiv.org/pdf/1506.02305.

[85] J. Pancin et al., Nuclear Instruments and Methods in Physics Research A 524 (2004) 102114.

[86] http://www.caen.it/csite/CaenProd.jsp?idmod=774parent=13.

[87] https://www.kfki.hu/mtaita_lai/laiprodu.htm.

[88] D. Schumann et al., Radiochim. Acta 101 (2013) 509.

[89] E. A. Maugeri et al., J. Instrum. 12 (2017).

[90] U. Koster et al., Nucl. Instrum. Methods Phys. Res. B 204 (2003) 343.

[91] E. Maugeri et al., Nucl. Instrum. Meth. A 889, 138 (2018).

[92] S. Agostinelli et al., Nucl. Instrum. Methods Phys. Res. A 506 (2003) 250.

[93] D. G. Krige, J. Chem. Metal. Min. Soc. South Afr. 52 (1951) 119.

[94] S. I. Sakata et al., Comput. Struct. 86 (2008) 1477.

[95] P. Žugec et al., Nucl. Instrum. Methods A 812, 134 (2016).

[96] P. Žugec, Users guide through Pulse Shape Analysis routines, 16 December 2014.

[97] M. Barbagallo, et al., Rev. Sci. Instrum., 84 (2013), p. 033503.

[98] S. Lo Meo, et al., Eur. Phys. J., A51 (2015), p. 160.

[99] S. Lo Meo, L. Cosentino, A. Mazzone, P. Bartolomei, P. Finocchiaro, Nucl. Instrum. Methods A, 866 (2017), p. 48.

[100] ENDF/B-VII.1 library (http://www.nndc.bnl.gov/sigma/).

[101] M. B. Chadwick et al., Nuclear Data Sheets 112, 2887 (2011), special Issue on ENDF/B-VII.1 Library.

[102] R. Hanna, The London, Edinburgh, and Dublin Philosophical Magazine and Journal of Science 46, 381 (1955), https://doi.org/10.1080/14786440408520571.

[103] J. Červená et al, Czechoslovak Journal of Physics B 39, 1263 (1989).

[104] https://twiki.cern.ch/twiki/bin/view/NTOFPublic/Be7npPaperDraft.

[105] D. Tilley, J. Kelley, J. Godwin, D. Millener, J. Purcell, C. Sheu, and H. Weller, Nuclear Physics A 745, 155 (2004).

[106] R. H. Cyburt et al., Phys. Rev. D 70 (2004) 023505.

[107] M. S. Smith, L. H. Kawano, and R. A. Malaney, The Astrophysical Journal 85, 219 (1993).

[108] P. Descouvemont, A. Adahchour, C. Angulo, A. Coc, and E. Vangioni-Flam, Atomic Data and Nuclear Data Tables 88 (2004) 203.

[109] P. D. Serpico, S. Esposito, F. Iocco, G. Mangano, G. Miele, and O. Pisanti, Journal of Cosmology and Astroparticle Physics 12 (2004) 10.

[110] A. Arbey, Computer Physics Communications 183 (2012) 1822.

[111] R. V. Wagoner, ApJS, 18, 247 (1969).

[112] Caughlan and Fowler, ADNDT 40, 283 (1988).

[113] Ando et al. Phys. Rev. C 74, 025809 (2006).

[114] Iliadis et al., ApJ 831, 107 (2016).

[115] L. Kawano, FERMILAB-Pub-92/04-A (1992).

[116] A. Mishra and D. N. Basu, Rom. Jour. Physics 9-10, 1317 (2012).

[117] A. Coc, J. P. Uzan, and E. Vangioni, Journal of Cosmology and Astroparticle Physics 10, 050 (2014).

[118] A. Coc, P. Petitjean, J.-P. Uzan, E. Vangioni, P. Descouvemont, C. Iliadis, and R. Longland, Phys. Rev. D 92, 123526 (2015).

[119] V. Singh, J. Lahiri, D. Bhowmick, and D. N. Basu, (2017), arXiv:1708.05567.

[120] N. Colonna, F. Gunsing, and F. Kppeler, Prog. Part. Nucl. Phys. in press (2018).

[121] C. Lee and X. L. Zhou, Nucl. Instr. Meth. B 152, 1 (1999).

[122] M. S. Herrera, G. A. Moreno, and A. J. Kreiner, Nucl. 495 Instr. Meth. B 349, 64 (2015).

[123] M. Friedman et al., Nucl. Instr. Meth. A 698, 117(2013).

[124] R. Reifarth et al., Nucl. Instr. Meth. A 608, 139(2009).

[125] C. Lederer et al., Phys.Rev.C 85,055809(2012).

[126] G. Martin-Hernandez et al., Phys. Rev. C 94, 034620 (2016).

[127] J. H. Gibbons and R. L. Macklin, Phys. Rev. 114, 571 (1959).